Washington University in St. Louis
Washington University Open Scholarship

All Theses and Dissertations (ETDs)

Winter 1-1-2012

Dynamic Deformation and Mechanical Properties of Brain Tissue

Yuan Feng
Washington University in St. Louis

Follow this and additional works at: https://openscholarship.wustl.edu/etd

Recommended Citation
Feng, Yuan, "Dynamic Deformation and Mechanical Properties of Brain Tissue" (2012). *All Theses and Dissertations (ETDs)*. 1003.
https://openscholarship.wustl.edu/etd/1003

This Dissertation is brought to you for free and open access by Washington University Open Scholarship. It has been accepted for inclusion in All Theses and Dissertations (ETDs) by an authorized administrator of Washington University Open Scholarship. For more information, please contact digital@wumail.wustl.edu.

WASHINGTON UNIVERSITY IN ST. LOUIS

School of Engineering & Applied Science

Department of Mechanical Engineering and Materials Science

Dissertation Examination Committee:
Philip Bayly, Chair
Guy Genin
Phillip Gould
Kenneth Jerina
Eric Leuthardt
Ruth Okamoto
Robert Pless
Larry Taber

Dynamic Deformation and Mechanical Properties of Brain Tissue

by

Yuan Feng

A dissertation presented to the
Graduate School of Arts and Sciences
of Washington University
in partial fulfillment of the
requirements for the degree of
Doctor of Philosophy

December 2012

Saint Louis, Missouri

© copyright 2012 by Yuan Feng.

All rights reserved.

Table of Contents

List of Figures

List of Tables

Nomenclature

Ω_0 – reference configuration

Ω – deformed configuration

$\boldsymbol{X}$ – position vector in the reference (material) configuration

$\boldsymbol{x}$ – position vector in the deformed (spatial) configuration

$\boldsymbol{F}$ – deformation gradient

J – volume ratio

dV – referential infinitesimal volume

dv – deformed infinitesimal volume

ρ_0 – density in the reference configuration

ρ – density in the deformed configuration

$\boldsymbol{R}$ – rigid body rotation tensor

$\boldsymbol{U}$ – pure stretch tensor acting on the reference configuration

$\boldsymbol{v}$ – pure stretch tensor acting on the deformed configuration

$\boldsymbol{C}$ – right Cauchy-Green tensor

$\boldsymbol{b}$ – left Cauchy-Green tensor

$\boldsymbol{E}$ – Green-Lagrange strain tensor

$\boldsymbol{e}$ – Euler-Almansi strain tensor

$\boldsymbol{\sigma}$ – Cauchy stress

ψ – strain energy function

$\boldsymbol{S}$ – second Piola-Kirchhoff stress tensor

I_1, I_2 , I_3 – principal (isotropic) invariants of $\boldsymbol{C}$

I_4, I_5 - pseudo invariants

$\boldsymbol{A}$ – unit vector representing the fiber direction in the reference configuration

$\boldsymbol{a}$ – vector representing the fiber direction in the deformed configuration

$\tilde{\boldsymbol{a}}$ – normalized unit vector representing the fiber direction in the deformed configuration

λ – fiber stretch after deformation

$\psi_{isotropic}$ – isotropic contribution component of the strain energy function

$\psi_{anisotropic}$ – anisotropic contribution component of the strain energy function

$\overline{\boldsymbol{C}}$ – modified right Cauchy-Green tensor

$\overline{\boldsymbol{b}}$ – modified left Cauchy-Green tensor

$\overline{I_1}, \overline{I_2}, \overline{I_3}$ – modified principal (isotropic) invariants of $\overline{\boldsymbol{C}}$

$\overline{I_4}, \overline{I_5}$ – modified pseudo invariants

$\psi_{volumetric}$ – the volumetric (volume-distorting) of the strain energy function

$\psi_{isochoric}$ – the isochoric (volume-preserving) component of the strain energy function

$\boldsymbol{C}$ – general elasticity tensor

$\boldsymbol{\varepsilon}$ – infinitesimal strain tensor

$[\mathbb{C}]$ – elastic stiffness matrix

$[\mathbb{S}]$ – elastic compliance matrix

$[\boldsymbol{\sigma}]$ – components of $\boldsymbol{\sigma}$ arranged in a column vector

$[\boldsymbol{\varepsilon}]$ – components of $\boldsymbol{\varepsilon}$ arranged in a column vector

I_5^* – pseudo invariant representing the fiber shearing element

$\overline{I_5^*}$ – isochoric pseudo-invariant representing the fiber shearing element

μ – parameter of the isotropic component of the strain energy function

κ – bulk modulus

ζ – parameter of the fiber stretching component of the strain energy function

ϕ – parameter of the fiber shearing component of the strain energy function

E – Young's modulus

ν – Poisson's ratio

η – viscosity coefficient

μ^*, G^* – complex shear modulus

μ', G' – storage shear modulus

μ'', G'' – loss shear modulus

μ_1 – shear modulus which is effective in the plane containing the tissue fiber

μ_2 – shear modulus which is effective in the plane perpendicular to the direction of the tissue fiber

λ – the first Lamé parameter

ρ – material density

u – displacement

τ – shear stress

F_s – shear force

γ – shear strain

k – indentation stiffness

Acknowledgments

I would like to give my sincere thanks to my advisor Dr. Bayly, whose patience, excellence, and dedication to academia always inspire and motivate me. Throughout my PhD study, he has been a great mentor and teacher, who overcomes the language and culture difference, passing the value of honesty, integrity, and a spirit of team work to me.

I would like to thank Dr. Genin and Dr. Okamoto who also guided me throughout my study at Washington University. The enormous help they gave me are not only from the academic side, but also from the life too.

When I served as a teaching assistant at the mechanical engineering department, Dr. Gould, Dr. Peters, and Dr. Jerina have been a great mentor of teaching, and a great mentor of life of me. I am also very grateful to be the teaching assistant of Dr. Look, Dr. Pitt, Dr. Malast, and Dr. Sellers. All the students that I have been met during my teaching assistant years, I learned so much from you too, and I always feel lucky and grateful to know all of you.

Most of my dissertation work focuses on the mechanics side, which I would never accomplish without taking the biomechanics course by Dr. Taber, the finite element analysis course by Dr. Szabo, and the continuum mechanics course by Dr. Avula.

The human and animal experiments are made possible with the help from the Department of Comparative Medicine and the Biomedical Magnetic Resonance Lab at Washington University. Financial support was provided by NIH grant RO1 NS55951. Finally, I would like to thank Bayly lab members and all my friends at Washington University - without your support, I could never finish this dissertation.

Yuan Feng

Washington University in St. Louis

December 2012

Dedicated to my family.

ABSTRACT OF THE DISSERTATION

Dynamic Deformation and Mechanical Properties of Brain Tissue

by

Yuan Feng

Doctor of Philosophy in Mechanical Engineering

Washington University in St. Louis, 2012

Professor Philip Bayly, Chairperson

Traumatic brain injury is an important medical problem affecting millions of people. Mathematical models of brain biomechanics are being developed to simulate the mechanics of brain injury and to design protective devices. However, because of a lack of quantitative data on brain-skull boundary conditions and deformations, the predictions of mathematical models remain uncertain. The objectives of this dissertation are to develop methods and obtain experimental data that will be used to parameterize and validate models of traumatic brain injury. To that end, this dissertation first addresses the brain-skull boundary conditions by measuring human brain motion using tagged magnetic resonance imaging. Magnetic resonance elastography was performed in the ferret brain to measure its mechanical properties in vivo. Brain tissue is not only heterogeneous, but may also be anisotropic. To characterize tissue anisotropy, an experimental procedure combining both shear testing and indentation was developed and applied to white matter and gray matter. These measurements of brain-skull interactions and mechanical properties of the brain will be valuable in the development and validation of finite element simulations of brain biomechanics.

Chapter 1

Introduction

In this introduction, a brief description of traumatic brain injury (TBI) and its importance is given. Ongoing computer simulation methods for understanding TBI need complete and accurate understanding of both brain tissue properties and boundary conditions. The chapter also summarizes and compares recent studies of brain tissue biomechanical properties. Current methods for investigating brain tissue properties and boundary conditions such as mechanical test methods and magnetic resonance imaging methods are discussed. The chapter discusses the significance of brain biomechanics in the fields of tissue injury study, neurosurgery, and brain development. This chapter concludes with specific aims of this dissertation and an overview of its organization.

The human head mainly consists of the skull which is a stiff protective shell, and the soft brain tissue inside the skull (Figure 1.1a). The brain consists of cerebral hemispheres, the cerebellum, and the brain stem. Each of the two hemispheres (left and right) is subdivided into frontal, parietal, temporal, and occipital lobes. The two hemispheres are connected by corpus callosum white matter tissue, and the cavities of between the tissues are filled with cerebrospinal fluid (CSF). Brain tissue includes gray matter tissue, which is made of neuronal cell bodies that do not have myelinated axon fiber tracts, and white matter tissue, which is mostly made of glial cells and myelinated axon fiber tracts. The whole brain is covered by the pia mater, arachnoid mater, and the dura mater (Figure 1.1b), and CSF fills the cavities between each layers.

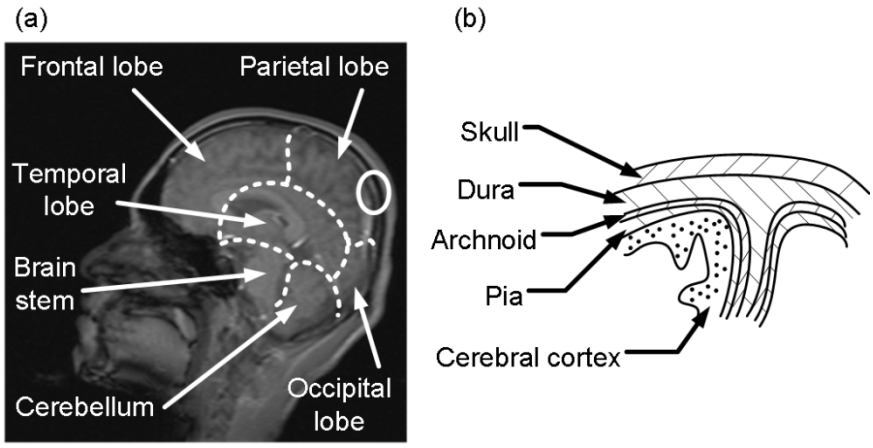

Figure 1.1 (a) Human brain sagittal plane MRI illustrating brain anatomy. (b) Illustration of skull-brain interface region. The area drawn corresponds to the white circle region in (a).

Although the cerebral cortex is confined inside the skull by the dura and pia membranes and tethered by the vasculature, it can still move relative to the skull during acceleration and deceleration. The white and gray matter composing the brain appear to have different mechanical properties (Table 1.1).

1.1 What Is Traumatic Brain Injury and What Can We Do about It?

1.1.1 Traumatic Brain Injury

Traumatic brain injury (TBI) is a complex injury caused by an external force that produces alteration in brain function or other evidence of brain pathology [1]. TBI is a leading cause of injury death and disability in the United States; about 53,000 persons die from TBI-related injuries each year [2]. Over the past half-century, researchers have investigated the mechanisms, injury threshold, and pathology of TBI, but much is still unknown.

TBI mechanisms have been categorized as primary and secondary [3], where primary refers to an injury occurring at the time of impact and secondary is a related injury that develops after the impact. The modes of injury include closed-head trauma, penetrating

injury and blast injury [3]. In this dissertation, both theoretical and experimental methods are used to investigate brain tissue response and the brain-skull interaction during mild impact, which will lead to a better understanding of primary injury mechanisms. The models and properties of brain tissue will help our understanding of both penetrating and blast injury cases.

Cerebral concussion is a common type of TBI: about 90% of the TBI are categorized as concussions or mild TBI [4]. In concussion, coup injury is defined as the injury at the site of the impact location, and contrecoup injury is defined as the injury in the opposite direction of the site of the impact location [5]. The mechanisms of coup and contrecoup injury [6] during concussion are still largely unclear. The biomechanics of concussion are influenced by many factors, including skull and brain geometry, and brain-skull interactions [7]. Although the geometry of the brain and skull may be acquired by imaging methods such as magnetic resonance imaging (MRI), how the brain interacts within the skull during acceleration or deceleration is still an active topic of research.

Although TBI may include injuries to white matter and the cerebral hemisphere (Figure 1.2), white matter tissue, in particular, appears to be deformed and damaged during trauma, leading to diffuse axonal injury (DAI) [8]. After TBI, pathological examination reveals that axons in white matter tended to get swollen and disconnected [8]. Although the mechanism of DAI is still unclear, it is postulated that when the brain tissue is under acceleration or deceleration, a certain threshold of tissue deformation is exceeded [9], thus generating un-restorable physical shape changes and tissue damage. Recent studies using diffusion tensor imaging (DTI) have also found that white matter tissue is very susceptible to damage after mild (m)TBI [10].

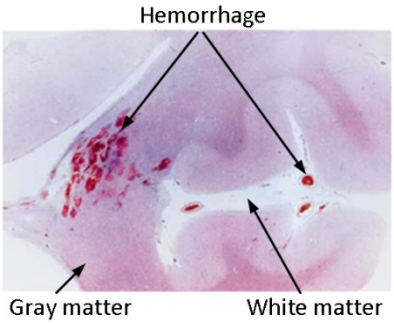

Figure 1.2 Histopathology slides of DAI sectioned from the corpus callosum from TBI after weeks of initial injury [9] (reprint with permission). Hemorrhage appeared at both gray matter and white matter.

1.1.2 Finite Element Computer Simulation

Predicting the macroscopic regions that will experience injurious stresses and strains during external loading is a primary goal of understanding TBI. Computer simulation methods (predominantly finite element (FE) simulations) have been proposed for prediction when brain injury will occur [11-14] and by what mechanisms [15-18]. FE simulations can predict strains in neural fibers (axons) [19] which are hypothesized to underlie diffuse axonal injury (DAI). Predicted strains from simulations can be correlated with injury markers [20] using strain-based thresholds for cellular and tissue injury determined under in vitro test conditions [21-22]. In other applications, FE simulations of brain tissue have been applied to investigate the head-neck responses during car crashes [23], and forensic practice [24]. A sample FE model of human head is shown in Figure 1.3.

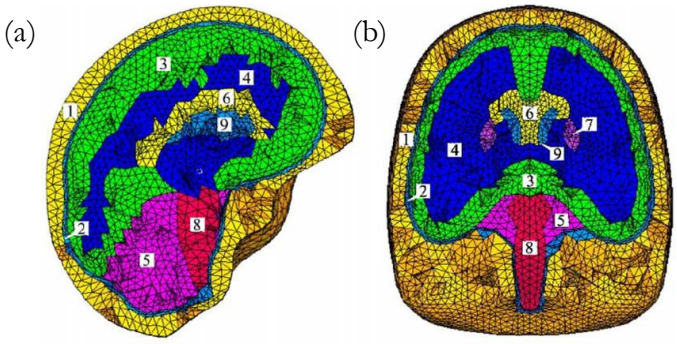

Figure 1.3 Finite element model of human head showing (a) mid-sagittal and (b) mid-coronal sections [25] (reprinted with permission).

However, to implement FE simulations of brain tissue models, a complete and accurate picture of the mechanical properties of brain tissue is needed. This should include detailed material constitutive relationships for different components of the brain, such as white matter, gray matter, vasculature and cerebrospinal fluid (CSF). The attachments of each component lead to brain-skull interactions that are also important for an accurate FE model.

1.1.3 Mechanical Tests of Brain Tissue Properties

The effort to characterize brain material properties has been sustained for over fifty years [26-27]. Both in vivo and ex vivo tests over a large range of sample species have given insights into brain tissue behavior. The mechanical test methods most commonly used for brain tissue are dynamic shear tests, tension tests, and compression/indentation tests. An overview of the most recent studies using dynamic shear tests (DST) is shown in Table 1.1.

Most of the DST studies assume the tested tissue to be isotropic. Results are mixed regarding whether white matter exhibits anisotropic properties. Although most of the tests distinguished between white and gray matter regions, the shear modulus estimates for white and gray matter differ among studies. Also, the shear modulus measured for the same species in the same region varied among studies, which may be due to the frequency range and the test conditions. The discrepancy of the tissue tests is also true for tension tests (Table 1.2) and compression/indentation tests (Table 1.3). All the DST and tension tests were carried out in vitro, because the sample has to be taken out of the living animal and shaped into a certain geometry before testing. However, indentation tests are possible in vivo because an indenter head can compress the brain tissue through an opening in the skull [28-30]. The flexibility of the indenter head also makes micron level indentation possible. The micron-indentation method has been used to investigate specific regions of white and gray matter [31-32].

Table 1.1 Overview of experimental studies on brain tissue in dynamic shear tests. Dynamic shear moduli measured: G', storage modulus; G'', loss modulus. Anisotropy tested: ISO, isotropic; ANI, anisotropic properties reported. Donor: HM, human; PC, porcine; BV, bovine; RT, rat. Region: WM, white matter without specification; GM, gray matter without specification; CX, cortex; TM, thalamus; BS, brain stem; CR, corona radiata; CC, corpus callosum; Sample test state: VV, in vivo; VT, in vitro. Sample geometry: D, circular shape with diameter in mm; H, height in mm; L, rectangular shape with length in mm; W, rectangular shape with width in mm.

	Sample geometry (mm)	Frequency (Hz)	State	Species, Region	G' (Pa)	G'' (Pa)	anisotropy
[33]	D12.7×H3	2-350	VT	HM, CR	696-765	262-351	ISO
				HM, GM	4130-1060	1380-1510	ANI
[34]	D10-12×H1-2	0.16-16	VT	BV, WM	212-580	78-424	–
[35]	D30×H1.5	1, 5, 20	VT	BV, WM	800-2000	300-500	–
[36]	D5.5×H1	20-200	VT	PC, BS	1200-2200	250-2500	ANI
[37]	D10-12×H1-2	20-200	VT	PC	500-1800	250-2200	–
[38]	D20×H2	0.01-20	VT	BV, CC, CR	1000-1500	600-900	–
[39]	L10×W5×H1	–	VT	PC, CC, CR	182.2	–	ANI
				PC, GM	263.6		ISO
[40]	D7-10×H1-3	0.04-16	VT	PC, CR	250-800	100-400	–
[41]	D20×H4-5	0.1-10	VT	PC, CR	390-650	75-190	–
[42]	D10-13×H1.5-3.5	1-10	VT	PC, TM	150-200	45-90	–
[43]	D8-12×H2	1-10	VT	PC, CR	300-800	100-400	ANI
[44]	D10,20×H0.15-0.85	0.1-6310	VT	PC, CR	2100-16800	400-18700	ISO

1.1.4 In Vivo Measurement by Magnetic Resonance Imaging (MRI)

Although mechanical testing methods give a straightforward way of measuring brain tissue properties, few measurements have been carried out in vivo [28-30]. Magnetic resonance (MR) imaging provides a useful way to measure both the tissue properties and tissue boundary conditions in vivo.

The measurement of tissue displacement in vivo by MR tagging provides a tool for investigating the boundary conditions of FE model of TBI. Originally applied to study the heart motion in vivo [48-49], MR tagging can be used to track the displacement of brain motion inside skull and to characterize the deformation of brain tissue [50-51]. The displacement and deformation information are useful for any brain related FE modeling.

For in vivo measurement of tissue properties, MR elastography (MRE) [52-53] is now widely used. MRE has been used not only to study both human [54-58] and animal [41, 59-63] brain, but also to study other organs and tissues such as liver [55, 64-65], breast [66-68], heart [69], prostate [70-71], muscle [72].

Table 1.2 Overview of experimental studies on brain tissue in tension tests. Shear modulus was calculated or extrapolated based on tension test. Anisotropy tested: ISO, isotropic; ANI, anisotropic properties reported. Donor: HM, human; PC, porcine;. Region: WM, white matter without specification; GM, gray matter without specification; CR, corona radiata; CC, corpus callosum; Sample test state: VT, in vitro. Sample geometry: D, circular shape with diameter in mm; H, height in mm; L, rectangular shape with length in mm; W, rectangular shape with width in mm.

	Sample geometry (mm)	Strain rate (s^{-1})	State	Specimen	Shear Modulus (Pa)	anisotropy
[45]	L40-60×W10×H2-5	0.01	VT	PC, CC	502.12	ANI
				PC, CR	378.55	ANI
				PC, GM	319.28	ISO
[46]	D30×H10	$0.64\text{-}0.64\times10^{-2}$	VT	PC	842	–
[47]	–	$5.5\text{-}9.3\times10^{-3}$	VT	HM	–	–

1.1.5 In Vivo Measurement by Magnetic Resonance Imaging (MRI)

Although mechanical testing methods give a straightforward way of measuring brain tissue properties, few measurements have been carried out in vivo [28-30]. Magnetic

resonance (MR) imaging provides a useful way to measure both the tissue properties and tissue boundary conditions in vivo.

Table 1.3 Overview of experimental studies on brain tissue in indentation tests. Shear modulus was calculated or extrapolated based on indentation measurement. All the indentation tests listed assumed isotropic material properties. Donor: HM, human; PC, porcine; BV, bovine; RT, rat. Region: WM, white matter without specification; GM, gray matter without specification; CX, cortex; CR, corona radiata; CC, corpus callosum; Sample test state: VV, in vivo; VT, in vitro. Sample geometry: D, circular shape with diameter in mm; H, height in mm; L, rectangular shape with length in mm; W, rectangular shape with width in mm. Indenter geometry: R, spherical indenter head with radius in mm; CP, compression test.

	Sample geometry (mm)	Indentation speed (mm×s^{-1})	Indenter geometry	Depth (mm)	State	Specimen	Shear Modulus (Pa)
[28-29]	−	1	R10	3.9	VV	PC	1052
[30]	−	1, 3	R2	4	VV	PC	450-717
[48]	D20.5×H4	0.0001, 0.001, 0.01	CP	0.05×4	VT	BV, CC	129.6
[49]	D8-12×H2	0.045	CP	0.1×2	VT	BV, CR	202-1339
[50]	H0.225	0.003	R0.02	0.02-0.04	VT	RT, WM	152-384
						RT, GM	384-508
[32]	D30×H1-2	0.1, 0.34, 1	R2	0.1-0.3	VT	PC, WM	925-1209
						PC, GM	669-738
[31]	H2	0.75	R0.5	0.04	VT	RT, CC	238
						RT, CX	55-485
[51]	H2	0.75	R0.25	0.04	VT	PC, CC	116
						PC, CX	292

The measurement of tissue displacement in vivo by MR tagging provides a tool for investigating the boundary conditions of FE model of TBI. Originally applied to study the heart motion in vivo [52-53], MR tagging can be used to track the displacement of brain motion inside skull and to characterize the deformation of brain tissue [54-55]. The displacement and deformation information are useful for any brain related FE modeling.

For in vivo measurement of tissue properties, MR elastography (MRE) [56-57] is now widely used. MRE has been used not only to study both human [58-62] and animal [41, 63-67] brain, but also to study other organs and tissues such as liver [59, 68-69], breast [70-72], heart [73], prostate [74-75], muscle [76].

1.1.6 Significance of Brain Tissue Biomechanics

The mechanisms of TBI are still unclear, and factors such as injury thresholds and conditions for inducing DAI are still topics of current research [17, 77]. A complete picture of the mechanical properties of brain tissue is needed to relate the mechanical responses of brain tissue to actual tissue damage. Also, accurate information about tissue properties will help implement finite element analysis (FEA) of brain tissue models [16, 24]. Both in vivo and ex vivo brain biomechanics data will be useful for illuminating the mechanics and modeling of TBI.

In neurosurgery, neurosurgical retraction is needed to give the surgeons a good view during surgery. The retraction force applied to the brain tissue may damage the brain tissue, and thus needs to be monitored [78]. However, to understand the level of retraction force applied to the brain tissue, a clear picture of tissue responses to external loading is needed. Biomechanical information about brain tissue will help both the experimental studies and also numerical simulations [29]. Thus, it is of great interest to investigate biomechanical models and properties of the brain tissue.

Mechanisms of brain development such as cortical folding involve mechanical processes [79]. Knowledge of the mechanics of the folding process will help in understanding abnormal convolutional development and associated cerebral malfunctions. Current hypotheses include differential growth [80] and tension-based theories [81]. The mechanics of brain tissue will provide a basic foundation for both experiment and computational evaluation of competing hypotheses.

1.2 Dissertation Organization

1.2.1 Specific Aims

With the overall objective of acquiring data to parameterize and validate computer models of traumatic brain injury, the following specific aims are included.

- Aim 1: Investigate the relative displacement field of the brain with respect to the skull in human subjects during mild head acceleration, using MR tagging.

- Aim 2: Use MRE to characterize the mechanical properties of ferret brain in vivo.

- Aim 3: Investigate the anisotropic properties of brain tissue. First establish general procedures for the study of soft anisotropic viscoelastic materials by testing fibrin gel, then apply these procedures to study the anisotropy of white matter.

1.2.2 Dissertation Organization

This dissertation follows the following presentation order:

- Chapter 2 gives the common theoretical background for the dissertation. After a brief introduction of basic principles, specialization to transversely isotropic material is presented. Constitutive equations forms for both small and large strains are discussed that are capable of describing white matter anisotropy. Basic principles of linear viscoelasticity and its application to wave propagation in soft tissue are also presented.

- Chapter 3 describes the relative displacement of the brain during mild frontal impact. This chapter is aimed at providing accurate and reliable boundary

conditions for FE models of TBI. The imaging methods and experimental devices are described. Tagged image acquisition, extraction of displacements, and analysis of deformation are presented. Results consisting of relative displacement and deformation of brain tissue are shown.

- Chapter 4 is an in vivo study of mechanical properties of the ferret brain using MRE. Imaging sequences and experiment setups are presented. Displacement, strain, and curl fields in three dimensions are extracted, and used to estimate viscoelastic properties of the brain tissue.

- Chapter 5 describes a preliminary study of a soft transversely isotropic material. After introducing the preparation of fibrin gel, which is a controllable fibrin-reinforced material, a test protocol for studying transversely isotropic material is described. The combination of dynamic shear testing and indentation testing can provide, in theory, all the information needed to characterize an incompressible, transversely isotropic material.

- In Chapter 6 the test protocol from Chapter 4 is applied to investigate brain tissue anisotropy. Results from testing of both white matter and gray matter are presented. Experimental results are discussed in the context of the proposed transversely isotropic model in Chapter 2.

- Chapter 7 summarizes the dissertation, outlines the significance of the results, and gives an overview of proposed future studies.

Chapter 2

General concepts behind hyperelastic and viscoelastic models of brain tissue

This chapter lays the theoretical groundwork for the rest of the dissertation. Basic continuum mechanics theory is introduced first. General hyperelastic constitutive relations for a transversely isotropic material under finite strain are presented, followed by specialization to the small strain regime. To describe the tissue anisotropy in both simple shear and extension, a form of candidate constitutive model is proposed. The model parameters and their implications for material response are also discussed. Brain tissue is essentially viscoelastic, so basic principles of viscoelasticity are also introduced in this chapter. Shear wave propagation in a viscoelastic medium is discussed, which has specific applications to MRE studies.

2.1 Introduction

Constitutive relations are of fundamental importance for the mechanical modeling of brain tissue. A proper constitutive model can help researchers understand the tissue response, and thus provide insights into tissue injury mechanisms. Approaches for modeling biological tissues can be categorized into structural and phenomenological types. The structural approach is based explicitly on the tissue structures and composition, whereas the phenomenological approach models the overall tissue behavior. In this study, a combined approach is adopted to study brain tissue.

Continuum mechanical models have been widely applied to soft biological tissues. They have been used to study tissues such as arterial wall [82], myocardium [83-85], and brain tissue [29, 78, 86-87]. The continuum-based theory can describe both small and large deformation, and can be used for constructing both structural [82, 87] and phenomenological constitutive models [29, 86].

Brain tissue is highly heterogeneous because it contains both white and gray matter, thus ideally, constitutive modeling of brain tissue should be done separately for white and gray matter. However, in small animals such as the rat and the mouse, where only a small portion of the brain tissue is white matter, a homogeneous model is usually used for the whole brain [65, 67]. White matter, consisting of aligned axonal fibers, is hypothesized to be mechanically anisotropic; in contrast, gray matter is hypothesized to be mechanically isotropic [39]. Some current anisotropic models for the white matter are based on the principle of hyperelasticity, in which a particular strain energy function is used to specify the constitutive law [87]. Since the white matter has predominantly aligned axonal fibers, transversely isotropic, linearly elastic or viscoelastic models have been adopted to describe the mechanical behavior of the white matter [78, 87].

Spencer [88] pioneered the work on the transversely isotropic material modeling. He introduced formulations for both thesmall and the large strain regime, using classical linear elasticity theory and a hyperelastic model, respectively. These formulations have been widely adopted or paralleled by others. Most of the anisotropic strain energy functions in the literature include pseudo-invariants proposed by Spencer, and have been successfully applied to the modeling of myocardium [83, 85], brain stem [86, 89], and the white matter [87].

As an initial step, this chapter focuses on the elastic modeling of the transversely isotropic properties of the white matter. However, brain tissue is essentially viscoelastic. Characterization of the viscoelastic properties of brain tissue started at the very early stage of studying brain tissue [33, 90-91]. Some of the current viscoelastic models include, but are not limited to: the Prony series [30, 39, 46, 92], the Fractional Zener model [59, 93], and the springpot model [94]. A general characterization of anisotropic,

hyperelastic, and viscoelastic model of the brain tissue would need comprehensive experimental tests and simulations. As a first step, an isotropic visoelastic model is used for inverting the dynamic shear modulus from MRE experiments.

This chapter introduces basic hyperelastic and viscoelastic theories in the context of brain tissue modeling. Relations between the general strain energy function and classical stiffness and compliance matrices are derived, before proposing a specific example strain energy function for white matter. A Maxwell model is presented as a first step to illustrate the viscoelastic behavior of white matter. Wave propagation in a viscoelastic medium is discussed, and an inversion method for calculating dynamic shear modulus is introduced which will be applied in later chapters.

2.2 Kinematics of Deformation

In continuum mechanics, deformation is defined as a transformation from the reference configuration Ω_0 to the deformed configuration Ω. The deformation gradient $\boldsymbol{F}$ is a tensor describing this transformation:

$$\boldsymbol{F} = \frac{\partial \boldsymbol{x}}{\partial \boldsymbol{X}}, \tag{2.1}$$

where $\boldsymbol{X}$ is the position vector in the reference (material) configuration and $\boldsymbol{x}$ is the position vector in the deformed (spatial) configuration. $\boldsymbol{F}$ acts as a push-forward two-point tensor connecting the reference and deformed positions of a material point. The determinant of $\boldsymbol{F}$ is the volume ratio J between deformed and referential infinitesimal volume:

$$J = \det(\boldsymbol{F}) = \frac{dv}{dV} = \frac{\rho_0}{\rho}, \tag{2.2}$$

where dv is the deformed infinitesimal volume, ρ is the density in the deformed configuration, dV is the volume in the reference configuration, and ρ_0 is the density in the reference configuration. As an illustration, a 2-D deformation gradient $\begin{bmatrix} 1 & 0.25 \\ 0.5 & 1 \end{bmatrix}$ is applied to a unit circle to generate the deformed ellipsoid. Figure 2.1 shows how this deformation gradient works.

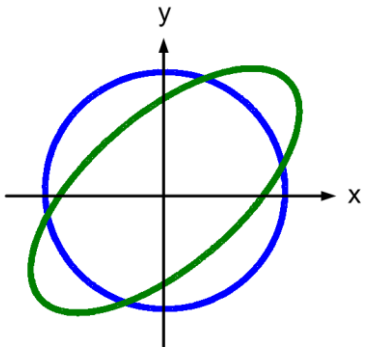

Figure 2.1 Ellipsoid after deformation. The ellipsoid is the deformed shape of the unit circle, on which the position of each displaced point is calculated by applying the deformation gradient to the corresponding point at the unit circle.

The deformation gradient $\boldsymbol{F}$ can be decomposed into the a rotational component and a stretching component:

$$\boldsymbol{F} = \boldsymbol{RU} = \boldsymbol{vR}, \tag{2.3}$$

where $\boldsymbol{R}$ is the rigid body rotation tensor, $\boldsymbol{U}$ and $\boldsymbol{v}$ are pure stretch tensors acting on reference and deformed configuration, respectively. Following by the definition of deformation gradient tensor, the right and left Cauchy-Green tensor are defined as:

$$\boldsymbol{C} = \boldsymbol{F}^T\boldsymbol{F} = \boldsymbol{U}^2, \tag{2.4}$$

$$\boldsymbol{b} = \boldsymbol{F}\boldsymbol{F}^T = \boldsymbol{v}^2. \tag{2.5}$$

where $\boldsymbol{C}$ is the right Cauchy-Green tensor and $\boldsymbol{b}$ is the left Cauchy-Green tensor. The Material and spatial strain tensors based on the right and left Cauchy-Green tensors are:

$$\boldsymbol{E} = \frac{1}{2}(\boldsymbol{F}^T\boldsymbol{F} - \boldsymbol{I}) = \frac{1}{2}(\boldsymbol{C} - \boldsymbol{I}), \tag{2.6}$$

$$\boldsymbol{e} = \frac{1}{2}(\boldsymbol{I} - \boldsymbol{F}^{-T}\boldsymbol{F}^{-1}) = \frac{1}{2}(\boldsymbol{I} - \boldsymbol{b}^{-1}), \tag{2.7}$$

where $\boldsymbol{E}$ is called the Green-Lagrange strain tensor and $\boldsymbol{e}$ is called the Euler-Almansi strain tensor.

2.3 Hyperelastic and Linearly Elastic, Transversely Isotropic, Constitutive Models

2.3.1 Strain Invariants and Strain Energy Function

Under some conditions, brain tissue (white matter, e.g.) may be modeled as a type of hyperelastic (Green elastic) material. Under this assumption, the Cauchy stress $\boldsymbol{\sigma}(\boldsymbol{F})$ depends on the deformation gradient $\boldsymbol{F}$ only. Also, there exists a scalar-valued tensor function $\psi(\boldsymbol{F})$, (strain energy function) from which $\boldsymbol{\sigma}(\boldsymbol{F})$ can be derived [95]:

$$\boldsymbol{\sigma}(\boldsymbol{F}) = J^{-1}\frac{\partial\psi(\boldsymbol{F})}{\partial\boldsymbol{F}}\boldsymbol{F}^T. \tag{2.8}$$

From the definition of the Cauchy-Green tensor, we may further write the second Piola-Kirchhoff stress tensor $\boldsymbol{S}$ and the Cauchy stress $\boldsymbol{\sigma}$ in terms of $\boldsymbol{C}$:

$$\boldsymbol{S}(\boldsymbol{C}) = 2\frac{\partial\psi(\boldsymbol{C})}{\partial\boldsymbol{C}}, \tag{2.9}$$

$$\boldsymbol{\sigma}(\boldsymbol{C}) = 2J^{-1}\boldsymbol{F}\frac{\partial\psi(\boldsymbol{C})}{\partial\boldsymbol{C}}\boldsymbol{F}^T. \tag{2.10}$$

Based on the representation theorem for invariants [96], the strain energy function ψ can be expressed in terms of the invariants of $\boldsymbol{C}$. The principal (isotropic) invariants of $\boldsymbol{C}$ are:

$$I_1 = tr(\boldsymbol{C}), \tag{2.11}$$

$$I_2 = \frac{1}{2}\left[\left(tr(\boldsymbol{C})\right)^2 - tr(\boldsymbol{C}^2)\right], \tag{2.12}$$

$$I_3 = \det(\boldsymbol{C}). \tag{2.13}$$

For a transversely isotropic material, the oriented fibers will contribute to the strain energy function. If we define the fiber direction in the reference configuration by a unit vector $\boldsymbol{A}$, then ψ can be written as:

$$\psi = \psi(\boldsymbol{C}, \boldsymbol{A} \otimes \boldsymbol{A}). \tag{2.14}$$

Two additional pseudo-invariants [88] which contain the fiber-reinforcement effect are:

$$I_4 = \boldsymbol{A} \cdot \boldsymbol{C}\boldsymbol{A}, \tag{2.15}$$

$$I_5 = \boldsymbol{A} \cdot \boldsymbol{C}^2\boldsymbol{A}. \tag{2.16}$$

Notice that the fiber direction in the deformed configuration is $\boldsymbol{a} = \boldsymbol{F} \cdot \boldsymbol{A}$, whose magnitude is $((\boldsymbol{F} \cdot \boldsymbol{A})^T \cdot \boldsymbol{F} \cdot \boldsymbol{A})^{\frac{1}{2}} = \sqrt{I_4}$. The relation between the vector $\boldsymbol{a}$ and its normalized form $\tilde{\boldsymbol{a}}$ is:

$$\boldsymbol{a} = \boldsymbol{F} \cdot \boldsymbol{A} = \sqrt{I_4}\tilde{\boldsymbol{a}} = \lambda\tilde{\boldsymbol{a}}, \tag{2.17}$$

where $\lambda = \sqrt{I_4}$ represents the fiber stretch. The strain energy function for a transversely isotropic material in terms of invariants can be written as [88]:

$$\psi = \psi(I_1, I_2, I_3, I_4, I_5). \tag{2.18}$$

2.3.2 Constitutive Law under Finite Strain

When the tissue is under finite strain where the small strain approximation is not applicable, continuum-based hyperelasticity is appropriate. For a transversely isotropic hyperelastic material, the stress-strain relation can be expressed in terms of invariants using Eqs. (2.11)-(2.16). The constitutive law of Eq. (2.9) and Eq. (2.10) can be approached by using the chain rule:

$$\frac{\partial \psi}{\partial \boldsymbol{C}} = \sum_{i=1}^{5} \frac{\partial \psi}{\partial I_i} \frac{\partial I_i}{\partial \boldsymbol{C}}. \tag{2.19}$$

The derivatives of the invariants with respect to the right Cauchy-Green tensor are:

$$\frac{\partial I_1}{\partial \boldsymbol{C}} = \boldsymbol{I}, \tag{2.20}$$

$$\frac{\partial I_2}{\partial \boldsymbol{C}} = I_1 \boldsymbol{I} - \boldsymbol{C}, \tag{2.21}$$

$$\frac{\partial I_3}{\partial \boldsymbol{C}} = I_3 \boldsymbol{C}^{-1}, \tag{2.22}$$

$$\frac{\partial I_4}{\partial \boldsymbol{C}} = \boldsymbol{A} \otimes \boldsymbol{A}, \tag{2.23}$$

$$\frac{\partial I_5}{\partial \boldsymbol{C}} = \boldsymbol{A} \otimes \boldsymbol{C}\boldsymbol{A} + \boldsymbol{A}\boldsymbol{C} \otimes \boldsymbol{A}. \tag{2.24}$$

With Eq. (2.10) and Eq. (2.19-2.24), the Cauchy stress in terms of invariants is:

$$\boldsymbol{\sigma} = 2J^{-1}\left[\frac{\partial \psi}{\partial I_1}\boldsymbol{b} + \frac{\partial \psi}{\partial I_2}(I_1\boldsymbol{b} - \boldsymbol{b}^2) + I_3\frac{\partial \psi}{\partial I_3}\boldsymbol{I} + \frac{\partial \psi}{\partial I_4}\boldsymbol{a} \otimes \boldsymbol{a} + \frac{\partial \psi}{\partial I_5}(\boldsymbol{a} \otimes \boldsymbol{b}\boldsymbol{a} + \boldsymbol{a}\boldsymbol{b} \otimes \boldsymbol{a})\right]. \tag{2.25}$$

Note that deformed fiber direction $\boldsymbol{a}$ is used instead of its normalized form $\tilde{\boldsymbol{a}}$. A push-forward transformation of the contravariant stress tensor component is used to derive the Eq. (2.25):

$$\boldsymbol{F}(\boldsymbol{A}\otimes\boldsymbol{C}\boldsymbol{A}+\boldsymbol{A}\boldsymbol{C}\otimes\boldsymbol{A})\boldsymbol{F}^{T}=\boldsymbol{a}\otimes\boldsymbol{b}\boldsymbol{a}+\boldsymbol{a}\boldsymbol{b}\otimes\boldsymbol{a}. \tag{2.26}$$

If the part of the strain energy function which contains the isotropic invariants I_1, I_2 and I_3 are decoupled from the part containing I_4 and I_5, the strain energy can be separated into isotropic contribution component $\psi_{isotropic}$ and anisotropic contribution component $\psi_{anisotropic}$:

$$\psi(I_1,I_2,I_3,I_4,I_5)=\psi_{isotropic}(I_1,I_2,I_3)+\psi_{anisotropic}(I_4,I_5). \tag{2.27}$$

Constraints apply when both strain energy function and Cauchy stress vanish in the undeformed (reference) state (where $I_1=I_2=3, I_3=I_4=I_5=1$). Thus, the strain energy function must satisfy:

$$\psi(3,3,1,1,1)=0, \tag{2.28}$$

$$\left(\frac{\partial\psi}{\partial I_1}+2\,\frac{\partial\psi}{\partial I_2}+\frac{\partial\psi}{\partial I_3}\right)_{(3,3,1,1,1)}=0, \tag{2.29}$$

$$\left(\frac{\partial\psi}{\partial I_4}+2\,\frac{\partial\psi}{\partial I_5}\right)_{(3,3,1,1,1)}=0. \tag{2.30}$$

For nearly incompressible material, it is convenient to decompose the deformation gradient into dilatational and distortional parts [95]: $\boldsymbol{F}=J^{1/3}\overline{\boldsymbol{F}}$. The modified right and left Cauchy-Green tensors are:

$$\overline{\boldsymbol{C}}=\overline{\boldsymbol{F}}^{T}\overline{\boldsymbol{F}}=J^{-\frac{2}{3}}\boldsymbol{C}, \text{ and} \tag{2.31}$$

$$\overline{\boldsymbol{b}}=\overline{\boldsymbol{F}}\overline{\boldsymbol{F}}^{\boldsymbol{T}}=\boldsymbol{J}^{-\frac{\boldsymbol{2}}{\boldsymbol{3}}}\boldsymbol{b}. \tag{2.32}$$

The corresponding modified principal and pseudo-invariants are:

$$\overline{I_1}=tr(\overline{\boldsymbol{C}})=J^{-\frac{2}{3}}I_1, \tag{2.33}$$

$$\bar{I}_2 = \frac{1}{2}\left[\left(tr(\bar{\boldsymbol{C}})\right)^2 - tr(\bar{\boldsymbol{C}}^2)\right] = J^{-\frac{4}{3}} I_2, \tag{2.34}$$

$$\bar{I}_3 = \det(\bar{\boldsymbol{C}}) = I_3^{\frac{2}{3}} = J^{\frac{4}{3}}, \tag{2.35}$$

$$\bar{I}_4 = \boldsymbol{A} \cdot \bar{\boldsymbol{C}}\boldsymbol{A} = J^{-\frac{2}{3}} I_4, \tag{2.36}$$

$$\bar{I}_5 = \boldsymbol{A} \cdot \bar{\boldsymbol{C}}^2 \boldsymbol{A} = J^{-\frac{4}{3}} I_5. \tag{2.37}$$

The strain energy function can also be expressed in the form of modified invariants, and written in a decoupled form [95]:

$$\psi = \psi(\bar{I}_1, \bar{I}_2, J, \bar{I}_4, \bar{I}_5) = \psi_{volumetric}(J) + \psi_{isochoric}(\bar{I}_1, \bar{I}_2, \bar{I}_4, \bar{I}_5), \tag{2.38}$$

where $\psi_{volumetric}$ is the volumetric (volume-distorting) component and $\psi_{isochoric}$ is the isochoric (volume-preserving) component.

Following the same procedure of deriving Eqs. (2.19)-(2.25), also noticing:

$$\frac{\partial \psi}{\partial \boldsymbol{C}} = \sum_{i=1}^{5} \frac{\partial \psi}{\partial \bar{I}_i} \frac{\partial \bar{I}_i}{\partial I_i} \frac{\partial I_i}{\partial \boldsymbol{C}}, \tag{2.39}$$

the Cauchy stress in terms of decoupled invariants is:

$$\begin{aligned} \boldsymbol{\sigma} = \frac{\partial \psi}{\partial \bar{I}_1}\left(-\frac{2}{3} J^{-1} \bar{I}_1 \boldsymbol{I} + 2J^{-\frac{5}{3}} \boldsymbol{b}\right) \\ + \frac{\partial \psi}{\partial \bar{I}_2}\left(-\frac{4}{3} J^{-1} \bar{I}_2 \boldsymbol{I} + 2J^{-\frac{5}{3}} \bar{I}_1 \boldsymbol{b} - 2J^{-\frac{7}{3}} \boldsymbol{b}^2\right) + \frac{\partial \psi}{\partial J} \boldsymbol{I} \\ + \frac{\partial \psi}{\partial \bar{I}_4}\left(-\frac{2}{3} J^{-1} \bar{I}_4 \boldsymbol{I} + 2J^{-\frac{5}{3}} \boldsymbol{a} \otimes \boldsymbol{a}\right) \\ + \frac{\partial \psi}{\partial \bar{I}_5}\left[-\frac{4}{3} J^{-1} \bar{I}_5 \boldsymbol{I} + 2J^{-\frac{7}{3}} (\boldsymbol{a} \otimes \boldsymbol{b}\boldsymbol{a} + \boldsymbol{a}\boldsymbol{b} \otimes \boldsymbol{a})\right]. \end{aligned} \tag{2.40}$$

2.3.3 Transversely Isotropic Constitutive Law under Small Strain

In the small deformation regime, where the reference and deformed coordinates are not distinguished, the equations derived in the large strain region can be simplified. Using the relation between the strain energy function and the classic elasticity formulation, parameters influencing the mechanical response of materials are discussed.

In continuum mechanics, the general elasticity tensor $\mathbb{C}$ is defined as [95]:

$$\mathbb{C} = 2\frac{\partial \boldsymbol{S}(\boldsymbol{C})}{\partial \boldsymbol{C}} = \frac{\partial \boldsymbol{S}(\boldsymbol{E})}{\partial \boldsymbol{E}}, \tag{2.41}$$

where $\mathbb{C}$ is a fourth-order tensor. In the small strain regime, the following approximation relations exit:

$$\boldsymbol{\varepsilon} \approx \boldsymbol{E} \approx \boldsymbol{e}. \tag{2.42}$$

Because reference and deformed coordinates are not distinguished in small deformation, the left and right Green tensors are identical:

$$\boldsymbol{C} = \boldsymbol{b} = \boldsymbol{I} + \boldsymbol{2\varepsilon}. \tag{2.43}$$

The corresponding isotropic and pseudo-invariants in terms of small strain $\boldsymbol{\varepsilon}$ are:

$$I_1 = 3 + 2tr(\boldsymbol{\varepsilon}), \tag{2.44}$$

$$I_2 = \frac{1}{2}\Big[6 + 8tr(\boldsymbol{\varepsilon}) + 4\big(tr(\boldsymbol{\varepsilon})\big)^2 - 4tr(\boldsymbol{\varepsilon}^2)\Big], \tag{2.45}$$

$$I_3 = \det(\boldsymbol{I} + \boldsymbol{2\varepsilon}), \tag{2.46}$$

$$I_4 = \boldsymbol{A}\cdot\boldsymbol{A} + 2\boldsymbol{A}\cdot\boldsymbol{\varepsilon}\boldsymbol{A} + \boldsymbol{A}\cdot\boldsymbol{\varepsilon}^2\boldsymbol{A}, \tag{2.47}$$

$$I_5 = \boldsymbol{A}\cdot\boldsymbol{A} + 4\boldsymbol{A}\cdot\boldsymbol{\varepsilon}\boldsymbol{A} + 5\boldsymbol{A}\cdot\boldsymbol{\varepsilon}^2\boldsymbol{A} + 2\boldsymbol{A}\cdot\boldsymbol{\varepsilon}^3\boldsymbol{A}. \tag{2.48}$$

Substitute Eqs. (2.44)-(2.48) into Eq. (2.25), and notice that $\boldsymbol{A} \approx \boldsymbol{a}$, the Cauchy stress can be expressed in terms of $\boldsymbol{\varepsilon}$ (eliminating higher order terms $\boldsymbol{\varepsilon}^2$):

$$\begin{aligned}\boldsymbol{\sigma} = 2J^{-1}\Big[&\Big(\frac{\partial\psi}{\partial I_1} + 2I_1\frac{\partial\psi}{\partial I_2} - \frac{\partial\psi}{\partial I_2} + I_3\frac{\partial\psi}{\partial I_3}\Big)\boldsymbol{I} \\ &+ \Big(2\frac{\partial\psi}{\partial I_1} + 2I_1\frac{\partial\psi}{\partial I_2} - 4\frac{\partial\psi}{\partial I_2}\Big)\boldsymbol{\varepsilon} + (\frac{\partial\psi}{\partial I_4} + 2\frac{\partial\psi}{\partial I_5})\boldsymbol{A}\otimes\boldsymbol{A} \\ &+ 2\frac{\partial\psi}{\partial I_5}(\boldsymbol{A}\otimes\boldsymbol{\varepsilon}\boldsymbol{A} + \boldsymbol{A}\boldsymbol{\varepsilon}\otimes\boldsymbol{A})\Big].\end{aligned} \tag{2.49}$$

In classical linear elasticity theory, where strain is small, a representation of the elasticity tensor $\mathbb{C}$ as a 6×6 matrix $[\mathbb{C}]$ is used to relate small strain tensor $\boldsymbol{\varepsilon}$ and stress $\boldsymbol{\sigma}$:

$$[\boldsymbol{\sigma}] = [\mathbb{C}][\boldsymbol{\varepsilon}], \tag{2.50}$$

$$[\boldsymbol{\varepsilon}] = [\mathbb{S}][\boldsymbol{\sigma}], \tag{2.51}$$

where $[\mathbb{C}]$ is defined as the elastic stiffness matrix, and $[\mathbb{S}]$ is the elastic compliance matrix.$[\boldsymbol{\sigma}]$ and $[\boldsymbol{\varepsilon}]$ are the components of $\boldsymbol{\sigma}$ and $\boldsymbol{\varepsilon}$ arranged in a column vector as in Eq. (2.52). Although the fourth-order tensor $\mathbb{C}$ has 81 parameters, the free parameters reduce to 36 because of the symmetry of $\boldsymbol{\sigma}$ and $\boldsymbol{\varepsilon}$. The existence of strain energy function further reduces the free parameters to 21. Thus $[\mathbb{C}]$, in a 6×6 matrix representing $\mathbb{C}$ as a stiffness matrix, relates stress and strain components:

$$\begin{bmatrix}\sigma_{11}\\ \sigma_{22}\\ \sigma_{33}\\ \sigma_{23}\\ \sigma_{13}\\ \sigma_{12}\end{bmatrix} = \begin{bmatrix}c_{11} & c_{12} & c_{13} & c_{14} & c_{15} & c_{16}\\ & c_{22} & c_{23} & c_{24} & c_{25} & c_{26}\\ & & c_{33} & c_{34} & c_{35} & c_{36}\\ & & & c_{44} & c_{45} & c_{46}\\ & sym & & & c_{55} & c_{56}\\ & & & & & c_{66}\end{bmatrix}\begin{bmatrix}\varepsilon_{11}\\ \varepsilon_{22}\\ \varepsilon_{33}\\ 2\varepsilon_{23}\\ 2\varepsilon_{13}\\ 2\varepsilon_{12}\end{bmatrix}. \tag{2.52}$$

For a transversely isotropic material, if the fiber direction is defined to be along the $\boldsymbol{x}_1$ direction in the Cartesian coordinates, then the plane of isotropy is perpendicular to $\boldsymbol{x}_1$ (Figure 2.2).

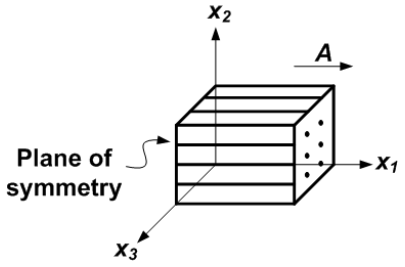

Figure 2.2 Basic model of a transversely isotropic material. Vector A indicates the fiber direction in the reference configuration. The plane of symmetry is perpendicular to x_1.

The stiffness matrix can be simplified as:

$$[\mathbb{C}] = \begin{bmatrix} c_{11} & c_{12} & c_{12} & & & \\ c_{12} & c_{22} & c_{23} & & \mathbf{0} & \\ c_{12} & c_{23} & c_{22} & & & \\ & & & \frac{c_{22}-c_{23}}{2} & & \\ & \mathbf{0} & & & c_{55} & \\ & & & & & c_{55} \end{bmatrix} \tag{2.53}$$

The relations between the stiffness matrix component and strain energy function are found to be [97-98]:

$$\frac{\partial^2\psi}{\partial I_1^2} + 4\frac{\partial^2\psi}{\partial I_1 \partial I_2} + 4\frac{\partial^2\psi}{\partial I_2^2} + 2\frac{\partial^2\psi}{\partial I_1 \partial I_3} + 4\frac{\partial^2\psi}{\partial I_2 \partial I_3} + \frac{\partial^2\psi}{\partial I_3^2} = \frac{c_{22}}{4}, \tag{2.54}$$

$$\frac{\partial\psi}{\partial I_2} + \frac{\partial\psi}{\partial I_3} = \frac{c_{23}-c_{22}}{4}, \tag{2.55}$$

$$\frac{\partial\psi}{\partial I_1} + \frac{\partial\psi}{\partial I_2} + \frac{\partial\psi}{\partial I_5} = \frac{c_{55}}{2}, \tag{2.56}$$

$$\frac{\partial^2\psi}{\partial I_1 \partial I_4} + 2\frac{\partial^2\psi}{\partial I_2 \partial I_4} + 2\frac{\partial^2\psi}{\partial I_1 \partial I_5} + \frac{\partial^2\psi}{\partial I_3 \partial I_4} + 4\frac{\partial^2\psi}{\partial I_2 \partial I_5} + 2\frac{\partial^2\psi}{\partial I_3 \partial I_5} = \frac{c_{12}-c_{23}}{4}, \tag{2.57}$$

$$\frac{\partial^2\psi}{\partial I_4^2} + 4\frac{\partial^2\psi}{\partial I_4 \partial I_5} + 4\frac{\partial^2\psi}{\partial I_5^2} + 2\frac{\partial\psi}{\partial I_5} = \frac{c_{11}-c_{22}+2c_{23}-2c_{12}}{4}. \tag{2.58}$$

The elastic stiffness matrix components in terms of ψ are:

$$
\begin{aligned}
c_{11} = 4\frac{\partial^2\psi}{\partial I_1^2} + 16\frac{\partial^2\psi}{\partial I_1\partial I_2} + 8\frac{\partial^2\psi}{\partial I_1\partial I_3} + 8\frac{\partial^2\psi}{\partial I_1\partial I_4} \\
+ 16\frac{\partial^2\psi}{\partial I_1\partial I_5} + 16\frac{\partial^2\psi}{\partial I_2^2} + 16\frac{\partial^2\psi}{\partial I_2\partial I_3} \\
+ 16\frac{\partial^2\psi}{\partial I_2\partial I_4} + 32\frac{\partial^2\psi}{\partial I_2\partial I_5} + 4\frac{\partial^2\psi}{\partial I_3^2} \\
+ 8\frac{\partial^2\psi}{\partial I_3\partial I_4} + 16\frac{\partial^2\psi}{\partial I_3\partial I_5} + 4\frac{\partial^2\psi}{\partial I_4^2} \\
+ 16\frac{\partial^2\psi}{\partial I_4\partial I_5} + 8\frac{\partial\psi}{\partial I_5} + 16\frac{\partial^2\psi}{\partial I_5^2},
\end{aligned} \tag{2.59}
$$

$$
\begin{aligned}
c_{12} = 4\frac{\partial^2\psi}{\partial I_1^2} + 16\frac{\partial^2\psi}{\partial I_1\partial I_2} + 8\frac{\partial^2\psi}{\partial I_1\partial I_3} + 4\frac{\partial^2\psi}{\partial I_1\partial I_4} \\
+ 8\frac{\partial^2\psi}{\partial I_1\partial I_5} + 4\frac{\partial\psi}{\partial I_2} + 16\frac{\partial^2\psi}{\partial I_2^2} + 16\frac{\partial^2\psi}{\partial I_2\partial I_3} \\
+ 8\frac{\partial^2\psi}{\partial I_2\partial I_4} + 16\frac{\partial^2\psi}{\partial I_2\partial I_5} + 4\frac{\partial\psi}{\partial I_3} + 4\frac{\partial^2\psi}{\partial I_3^2} \\
+ 4\frac{\partial^2\psi}{\partial I_3\partial I_4} + 8\frac{\partial^2\psi}{\partial I_3\partial I_5},
\end{aligned} \tag{2.60}
$$

$$
\begin{aligned}
c_{22} = 4\frac{\partial^2\psi}{\partial I_1^2} + 16\frac{\partial^2\psi}{\partial I_1\partial I_2} + 8\frac{\partial^2\psi}{\partial I_1\partial I_3} + 16\frac{\partial^2\psi}{\partial I_2^2} \\
+ 16\frac{\partial^2\psi}{\partial I_2\partial I_3} + 4\frac{\partial^2\psi}{\partial I_3^2},
\end{aligned} \tag{2.61}
$$

$$
\begin{aligned}
c_{23} = 4\frac{\partial^2\psi}{\partial I_1^2} + 16\frac{\partial^2\psi}{\partial I_1\partial I_2} + 8\frac{\partial^2\psi}{\partial I_1\partial I_3} + 4\frac{\partial\psi}{\partial I_2} + 16\frac{\partial^2\psi}{\partial I_2^2} \\
+ 16\frac{\partial^2\psi}{\partial I_2\partial I_3} + 4\frac{\partial\psi}{\partial I_3} + 4\frac{\partial^2\psi}{\partial I_3^2},
\end{aligned} \tag{2.62}
$$

$$
c_{55} = 2\frac{\partial\psi}{\partial I_1} + 2\frac{\partial\psi}{\partial I_2} + 2\frac{\partial\psi}{\partial I_5}. \tag{2.63}
$$

Based on the constraints on the strain energy function in the undeformed state (Eqs. (28)-(30)) c_{ij} can be expressed in terms of partial derivatives of ψ with respect to invariants except I_2:

$$[\mathbb{C}] = \begin{bmatrix} c_{11} & c_{12}' & c_{12}' & & & \\ c_{12}' & c_{22} & c_{23}' & & \mathbf{0} & \\ c_{12}' & c_{23}' & c_{22} & & & \\ & & & \frac{\partial\psi}{\partial I_1} - \frac{\partial\psi}{\partial I_3} & & \\ & \mathbf{0} & & & \frac{\partial\psi}{\partial I_1} - \frac{\partial\psi}{\partial I_3} + 2\frac{\partial\psi}{\partial I_5} & \\ & & & & & \frac{\partial\psi}{\partial I_1} - \frac{\partial\psi}{\partial I_3} + 2\frac{\partial\psi}{\partial I_5} \end{bmatrix}, \tag{2.64}$$

where two of the stiffness matrix components (c_{12} and c_{23}) are modified based on constraint equations:

$$\begin{aligned} c_{12}' = 4\frac{\partial^2\psi}{\partial I_1^2} + 16\frac{\partial^2\psi}{\partial I_1\partial I_2} + 8\frac{\partial^2\psi}{\partial I_1\partial I_3} + 4\frac{\partial^2\psi}{\partial I_1\partial I_4} + 8\frac{\partial^2\psi}{\partial I_1\partial I_5} + 16\frac{\partial^2\psi}{\partial I_2^2} \\ + 16\frac{\partial^2\psi}{\partial I_2\partial I_3} + 8\frac{\partial^2\psi}{\partial I_2\partial I_4} + 16\frac{\partial^2\psi}{\partial I_2\partial I_5} + 2\frac{\partial\psi}{\partial I_3} + 4\frac{\partial^2\psi}{\partial I_3^2} \\ + 4\frac{\partial^2\psi}{\partial I_3\partial I_4} + 8\frac{\partial^2\psi}{\partial I_3\partial I_5} - 2\frac{\partial\psi}{\partial I_1}, \end{aligned} \tag{2.65}$$

$$\begin{aligned} c_{23}' = 4\frac{\partial^2\psi}{\partial I_1^2} + 16\frac{\partial^2\psi}{\partial I_1\partial I_2} + 8\frac{\partial^2\psi}{\partial I_1\partial I_3} + 4\frac{\partial\psi}{\partial I_2} + 16\frac{\partial^2\psi}{\partial I_2^2} + 16\frac{\partial^2\psi}{\partial I_2\partial I_3} \\ + 2\frac{\partial\psi}{\partial I_3} + 4\frac{\partial^2\psi}{\partial I_3^2} - 2\frac{\partial\psi}{\partial I_1}. \end{aligned} \tag{2.66}$$

We observe that:

$$c_{11} - c_{22} = 4\frac{\partial^2\psi}{\partial I_4^2} + 16\frac{\partial^2\psi}{\partial I_4\partial I_5} + 16\frac{\partial^2\psi}{\partial I_5^2} + 8\frac{\partial\psi}{\partial I_5}, \tag{2.67}$$

which shows that both I_4 and I_5 terms contribute to the difference in the Young's moduli in the principal directions. For the shear components:

$$c_{55} - c_{44} = 2\frac{\partial\psi}{\partial I_5}, \tag{2.68}$$

which shows that the strain energy function must depend on I_5 if the material exhibits different shear moduli in different orthogonal planes parallel and normal to the fiber axis. The corresponding compliance matrix under reference configuration is in the appendix.

2.3.4 A Form of a Candidate Constitutive Model

In this section, a form of a candidate transversely isotropic constitutive model is presented for modeling white matter tissue. The presented constitutive model will be used for explaining experimental results in Chapter 6.

If $\boldsymbol{x_1}$ is the fiber direction, based on the relationship between I_4 and I_5 [98]:

$$I_4 = C_{11}, \tag{2.69}$$

$$I_5 = I_4^2 + C_{12}^2 + C_{13}^2, \tag{2.70}$$

where C_{11}, C_{12} and C_{13} are components of the right Cauchy-Green tensor $\boldsymbol{C}$. The fiber shearing element, namely I_5^*, can be separated:

$$I_5^* = I_5 - I_4^2. \tag{2.71}$$

Prior studies, as well as the experiments presented in chapter 6, suggest that white matter is nearly incompressible and anisotropic in both uniaxial stretch and simple shear deformations; in both cases, the stress-strain relationships depend on whether displacements are imposed parallel or perpendicular to the fiber axis. To analyze this behavior, it is convenient to use strain energy function in a decoupled form (Eq. (2.38)). The isochoric component can be further separated into the isotropic and anisotropic contributions [86, 98], following Eq. (2.27):

$$\psi_{isochoric} = \psi_{isotropic}(\bar{I}_1, \bar{I}_2) + \psi_{anisotropic}(\bar{I}_4, \bar{I}_5). \tag{2.72}$$

A neo-Hookean strain energy function (for example) may be chosen for the isotropic part. Considering the anisotropic part, noticing the relation between $\bar{I}_4$ and $\bar{I}_5$ (Eq. (2.70)), an alternative isochoric pseudo-invariant $\bar{I}_5^*$ that contains no contribution from fiber stretch is used:

$$\bar{I}_5^* = \bar{I}_5 - \bar{I}_4^2 = J^{-\frac{4}{3}} I_5^*. \tag{2.73}$$

$\bar{I}_5^*$ is a quadratic function of the shear strain in the plane parallel to the fiber axis. To describe the anisotropic component of the strain energy function, a combination of a quadratic term of $\bar{I}_4$ that describes the additional strain energy due to fiber stretch, and a term proportional to $\bar{I}_5^*$ that describes the effect of fiber-matrix interactions is introduced. The isochoric component of strain energy for this model is

$$\psi_{isochoric} = \left\{\frac{\mu}{2}(\bar{I}_1 - 3)\right\}_{isotropic} + \left\{\frac{\zeta}{2}(\bar{I}_4 - 1)^2 + \frac{\phi}{2}\bar{I}_5^*\right\}_{anisotropic}. \tag{2.74}$$

Finally, the volumetric component of strain energy in terms of a bulk modulus κ and the change in volume [86, 99] is:

$$\psi_{volumetric} = \frac{\kappa}{2}(J - 1)^2. \tag{2.75}$$

To describe nearly incompressible materials like brain tissue, the bulk modulus κ will have a large value relative to the parameters μ, ζ, and ϕ. The complete candidate strain energy function is thus:

$$\psi = \frac{\kappa}{2}(J - 1)^2 + \frac{\mu}{2}(\bar{I}_1 - 3) + \frac{\zeta}{2}(\bar{I}_4 - 1)^2 + \frac{\phi}{2}\bar{I}_5^*. \tag{2.76}$$

The corresponding Cauchy stress is:

$$\begin{aligned}\boldsymbol{\sigma} = {} & J^{-\frac{5}{3}}\mu\boldsymbol{b} + \kappa(J-1)\boldsymbol{I} - \frac{\mu}{3}I_1 J^{-\frac{5}{3}}\boldsymbol{I} \\ & + \frac{2}{3}J^{-\frac{5}{3}}I_4\left(J^{-\frac{2}{3}}(\phi-\zeta)I_4 + \zeta\right)\boldsymbol{I} \\ & - \frac{2}{3}J^{-\frac{7}{3}}\phi I_5\boldsymbol{I} + 2J^{-\frac{5}{3}}\left[J^{-\frac{2}{3}}(\zeta-\phi)I_4 - \zeta\right]\boldsymbol{a} \\ & \otimes \boldsymbol{a} + J^{-\frac{7}{3}}\phi(\boldsymbol{a}\otimes\boldsymbol{ba} + \boldsymbol{ab}\otimes\boldsymbol{a}).\end{aligned} \tag{2.77}$$

As required, the candidate strain energy function (Eq. (2.76)) and Cauchy stress both vanish in the reference configuration (Eqs. (2.28)-(2.30)). The Cauchy stress can also be written in terms of deviatoric invariants (Eqs. (2.33)-(2.37) and Eq. (2.73)):

$$\begin{aligned}\boldsymbol{\sigma} = {} & J^{-1}\mu\bar{\boldsymbol{b}} + \kappa(J-1)\boldsymbol{I} \\ & - \left(\frac{\mu}{3}J^{-1}\bar{I}_1 + \frac{2}{3}J^{-1}\phi\bar{I}_5^* - \frac{2}{3}J^{-1}\zeta\bar{I}_4(\bar{I}_4 \right. \\ & \left. - 1)\right)\boldsymbol{I} + 2J^{-1}[(\zeta-\phi)\bar{I}_4 - \zeta]\bar{\boldsymbol{a}}\otimes\bar{\boldsymbol{a}} \\ & + J^{-1}\phi\left(\bar{\boldsymbol{a}}\otimes\bar{\boldsymbol{b}}\bar{\boldsymbol{a}} + \bar{\boldsymbol{a}}\bar{\boldsymbol{b}}\otimes\bar{\boldsymbol{a}}\right),\end{aligned} \tag{2.78}$$

where $\bar{\boldsymbol{a}} = J^{-\frac{1}{3}}\boldsymbol{a}$, which makes $|\bar{\boldsymbol{a}}| = \bar{I}_4^{1/2}$.

2.3.5 Parameter Discussion

Consider small deformations of an incompressible material; for the perfectly incompressible case, no elasticity matrix can be defined since the stress state is indeterminate for a given deformation. However, the compliance matrix $[\mathbb{S}] = [\mathbb{C}]^{-1}$ can be obtained for an incompressible material, since strains are unique for a given stress state. Accordingly, use Eqs. (2.53)-(2.63),the elasticity matrix in terms of the parameters

of the general (compressible) strain energy function: $\kappa, \mu, \zeta,$ and ϕ can be obtained. The compliance matrix is then inverted from the elasticity matrix, where the limit is obtained as the bulk modulus $\kappa \to \infty$ and the dilatation $J \to 1$. Under these conditions the compliance matrix $[\mathbb{S}]$ at the reference configuration is:

$$[\mathbb{S}] = \begin{bmatrix} \frac{2}{8\zeta+6\mu} & -\frac{1}{8\zeta+6\mu} & -\frac{1}{8\zeta+6\mu} & & & \\ -\frac{1}{8\zeta+6\mu} & \frac{1}{2(8\zeta+6\mu)}+\frac{1}{4\mu} & \frac{1}{2(8\zeta+6\mu)}-\frac{1}{4\mu} & & \mathbf{0} & \\ -\frac{1}{8\zeta+6\mu} & \frac{1}{2(8\zeta+6\mu)}-\frac{1}{4\mu} & \frac{1}{2(8\zeta+6\mu)}+\frac{1}{4\mu} & & & \\ & & & \frac{1}{\mu} & & \\ & \mathbf{0} & & & \frac{1}{\phi+\mu} & \\ & & & & & \frac{1}{\phi+\mu} \end{bmatrix} = \begin{bmatrix} \frac{1}{E_1} & -\frac{\nu_{21}}{E_2} & -\frac{\nu_{21}}{E_2} & & & \\ -\frac{\nu_{12}}{E_1} & \frac{1}{E_2} & -\frac{\nu_2}{E_2} & & \mathbf{0} & \\ -\frac{\nu_{12}}{E_1} & -\frac{\nu_2}{E_2} & \frac{1}{E_2} & & & \\ & & & \frac{1}{\mu_2} & 0 & 0 \\ & \mathbf{0} & & 0 & \frac{1}{\mu_1} & 0 \\ & & & 0 & 0 & \frac{1}{\mu_1} \end{bmatrix}. \tag{2.79}$$

In Eq. (2.79-1), the compliance matrix is expressed in terms of the three parameters of the isochoric part of the strain energy function: $\mu, \zeta,$ and ϕ. Eq. (2.79-2) shows the classical form of the compliance matrix, expressed in terms of "physical" parameters: two Young's moduli (E_1 and E_2), two shear moduli (μ_1 and μ_2) and three Poisson's ratios (ν_{12}, ν_{21}, and ν_2). The two Young's moduli describe the stresses that arise in uniaxial stretch parallel (E_1) and perpendicular (E_2) to the fiber axis. The shear moduli govern the shear stresses during shear in a plane parallel to (μ_1) or normal to (μ_2) the fiber axis. The Poisson's ratios ν_{ij} describe the strain in the j-direction that arises as a

result of stretch in the i-direction ($\nu_2 = \nu_{23} = \nu_{32}$). Note that in general only five of the seven physical parameters are independent since the moduli and Poisson's ratios are related by two additional equations; in the incompressible case, the number of independent parameters is further reduced to three [88].

It is observed that for a transversely isotropic material, the shear modulus μ_1, which governs the shear force in planes containing $\boldsymbol{x}_1$ and the shear modulus μ_2, which is effective in the plane perpendicular to $\boldsymbol{x}_1$, differ due to the parameter ϕ, which multiplies the $\overline{I_5^*}$ term in the strain energy function. In the reference configuration:

$$\mu_1 = \frac{\partial \psi}{\partial I_1} - \frac{\partial \psi}{\partial I_3} + 2\frac{\partial \psi}{\partial I_5} = \mu + \phi, \tag{2.80}$$

$$\mu_2 = \frac{\partial \psi}{\partial I_1} - \frac{\partial \psi}{\partial I_3} = \mu. \tag{2.81}$$

By comparing components of the compliance matrix and solving for the elastic modulus in the fiber direction (E_1) and perpendicular to fiber direction (E_2), a a relation between E_1 and E_2 can be found:

$$\frac{E_1}{E_2} = 1 + \frac{\zeta}{\mu}. \tag{2.82}$$

This shows that the Young's modulus is larger for stretch in the fiber direction due to the parameter ζ. In the classic transversely isotropic linear elastic formulation of Spencer [88], the fiber reinforcement effect is captured by the analogous parameter β [88, 100]. It can be shown that for an incompressible material in the reference configuration:

$$\beta = 4(\zeta - \phi). \tag{2.83}$$

Eqs. (2.80)-(2.82) indicate that to fully characterize anisotropy in white matter tissue, information is needed from tests that involve stretch and shear in planes both parallel and perpendicular to the fiber axis. In chapter 6, information from both shear testing and indentation tests are used for an estimate of the model parameters. Although still in small strain regime, the model gives implications for model selection in the general hyperelastic case.

In the reference configuration state, if we take the ratio of β/μ_2 for consideration [100], using Eq. (2.80) and Eq. (2.83), then:

$$\frac{\beta}{\mu_2} = \frac{4(\zeta - \phi)}{\mu} = 4\left(\frac{\zeta}{\mu} - \frac{\mu_1}{\mu_2} + 1\right). \tag{2.84}$$

In Eq. (2.84), if the ratio μ_1/μ_2 is fixed, then the ratio β/μ_2 is in linear relation with ζ/μ, which is a ratio for the tissue anisotropy related to I_4 term. If β/μ_2 increases, ζ/μ also increases, which indicates a stronger tissue anisotropy.

Tension exists if the fibers are stretched ($I_4 > 1$), which means the stress components in Eq. (2.77) containing $\frac{\partial \psi}{\partial I_4}$ would be positive, which results in:

$$\frac{\partial \psi}{\partial I_4} = \zeta(I_4 - 1) > 0 \tag{2.85}$$

Note that when fiber is under compression ($I_4 < 1$), $\frac{\partial \psi}{\partial I_4} < 0$. The following derivation is used:

$$\frac{\partial \psi}{\partial I_4} = \frac{\zeta}{2} 2(\bar{I}_4 - 1)\frac{\partial \bar{I}_4}{\partial I_4} + \phi \frac{\partial \bar{I}_5^*}{\partial \mathrm{I}_4}, \tag{2.86}$$

with $\frac{\partial \bar{I}_5^*}{\partial I_4} = J^{-\frac{4}{3}}\left(\frac{\partial I_5}{\partial I_4} - 2I_4\right) = 0$.

2.4 Viscoelasticity

In the previous section, a linearly elastic model is introduced for modeling the anisotropy of white matter. However, brain tissue appears to be viscoelastic. As a first approach to address the viscoelastic properties, an isotropic model is adopted. In the chapter 4, the isotropic viscoelastic model is used to invert the dynamic shear moduli from MRE data.

2.4.1 Kelvin Chain and Maxwell Model

The basic components in linear viscoelasticity theory are spring and dashpot, where stress is in linear relation with strain and strain rate, respectively. The constitutive relation for a spring component is:

$$\sigma = \mu\varepsilon, \tag{2.87}$$

and for a dashpot component is:

$$\sigma = \eta\frac{d\varepsilon}{dt} \tag{2.88}$$

where σ is the stress, ε is the strain, μ and η represent the elastic modulus and viscosity coefficient, respectively (Figure 2.3).

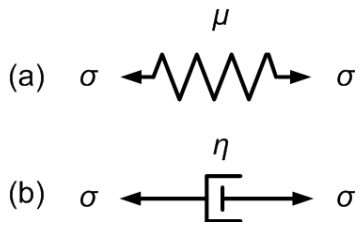

Figure 2.3. (a) Spring and (b) dashpot element model in linear viscoelasticity.

Viscoelasticity models can have various combinations of spring and dashpot elements. The fundamental combinations are the Maxwell fluid model and the Kelvin solid model (Figure 2.4). The corresponding constitutive equation for a Maxwell fluid is:

$$\sigma + \frac{\eta}{\mu}\frac{d\sigma}{dt} = \eta\frac{d\varepsilon}{dt}, \tag{2.89}$$

and for a Kelvin solid is:

$$\sigma = \mu\varepsilon + \eta\frac{d\varepsilon}{dt}. \tag{2.90}$$

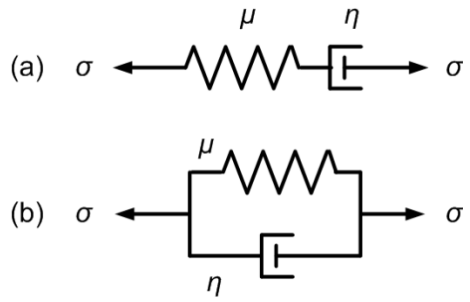

Figure 2.4. (a) Maxwell fluid and (b) Kelvin solid material models.

In general, a viscoelastic constitutive model can be expressed in a linear differential equation [101]:

$$\sum_{0}^{m} p_k \frac{d^k\sigma}{dt^k} = \sum_{0}^{n} q_k \frac{d^k\varepsilon}{dt^k}, \tag{2.91}$$

where p_k and q_k are model coefficients depending on the model construction. More complicated models can be constructed by combining the Maxwell fluid and the Kelvin solid model together. The two common prototypes are the Kelvin chain (Figure 2.5a) and the Maxwell model (Figure 2.5b).

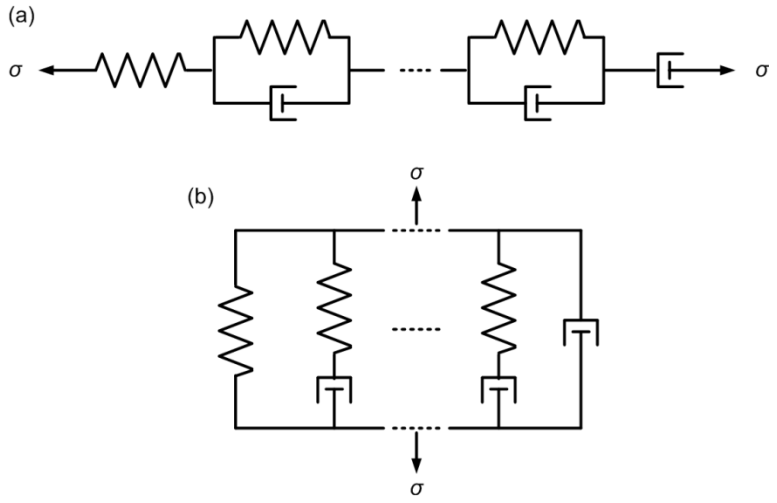

Figure 2.5. (a) Kelvin chain and (b) Maxwell model.

A corresponding general form of the viscoelastic constitutive relationship in the frequency domain can be obtained by assuming that both stress and strain are harmonic functions of time, i.e.:

$$\sigma = \sigma_0 e^{i\omega t}, \tag{2.92}$$

$$\varepsilon = \varepsilon_0 e^{i\omega t}, \tag{2.93}$$

where it is implicit that only the real component is retained.

Under these conditions the (complex) coefficients of the stress and strain functions are related by the complex shear modulus, μ^*, as:

$$\sigma_0 = \mu^* \varepsilon_0, \tag{2.94}$$

where $\mu^* = \mu' + i\mu''$.

2.4.2 Shear Wave Propagation and Viscoelastic Parameter Estimation

Under some conditions, brain tissue may be modeled as viscoelastic material. White matter tissue is anisotropic and heterogeneous; an extensive data set is needed to fully characterize the anisotropic viscoelastic model of the brain tissue. In the current MRE study (chapter 4), although 3D displacement data were acquired during shear wave propagation, an isotropic viscoelastic model was used to interpret the measurements. In fact, brain tissue is expected to exhibit nonlinear and anisotropic behavior. For small deflections, the linear approximation is well-justified on theoretical grounds.

For a homogenous, isotropic, linearly elastic material undergoing small strain, the equation governing wave propagation in 3D is [102-103]:

$$\rho \frac{\partial^2 \boldsymbol{u}}{\partial t^2} = \mu \nabla^2 \boldsymbol{u} + (\lambda + \mu) \nabla (\nabla \cdot \boldsymbol{u}), \tag{2.95}$$

where μ is the shear modulus (the second Lamé parameter), ρ is the material density, and λ is the first Lamé parameter. Since brain tissue is nearly incompressible, the parameter λ is much larger than μ, and the displacement fields are dominated by the contributions of shear waves. The shear wave component of displacement, $\boldsymbol{u}_T$, which is divergence free ($\nabla \cdot \boldsymbol{u}_T = 0$), is governed by a reduced form of Eq. (2.95):

$$\rho \frac{\partial^2 \boldsymbol{u}_T}{\partial t^2} = \mu \nabla^2 \boldsymbol{u}_T. \tag{2.96}$$

If the motion is harmonic with excitation frequency ω, the complex exponential form of the displacement is $u(x,t) = u_1(x) e^{i\omega t}$. Eq. (2.96) is simplified to:

$$-\rho \omega^2 u_1 = \mu \nabla^2 u_1. \tag{2.97}$$

Viscoelastic properties of the brain tissue can be calculated by applying the correspondence principle [101] to Eq. (2.97), in which the displacement component u_1 and shear modulus μ are replaced with complex analogous: $u_1 = u_1' + iu_1''$ and $\mu = \mu' + i\mu''$:

$$-\rho\omega_1^2(u_1' + iu_1'') = (\mu' + i\mu'')(\nabla^2 u_1' + i\nabla^2 u_1''). \tag{2.98}$$

Complex moduli can be estimated from the real and imaginary parts of this linear equation:

$$-\rho\omega^2 \begin{bmatrix} u_1' \\ u_1'' \end{bmatrix} = \begin{bmatrix} \nabla^2 u_1' & -\nabla^2 u_1'' \\ \nabla^2 u_1'' & \nabla^2 u_1' \end{bmatrix} \begin{bmatrix} \mu' \\ \mu'' \end{bmatrix} \tag{2.99}$$

The equation above illustrates how to estimate brain tissue dynamic shear moduli from harmonic displacement fields.

2.5 Conclusion

Continuum mechanics have been introduced in this chapter as background for the rest of the dissertation. Basic deformation kinematics and constitutive relations are discussed. A general, transversely isotropic model is presented, from which the stiffness and compliance matrices are derived for small strains. Parameters related to the material anisotropy are discussed in the small strain regime. Basic viscoelastic components along with the most common constitutive structures are described. The wave equation in a isotropic viscoelastic medium is introduced in to illustrate the process of inversion for dynamic shear moduli.

Chapter 3 uses the deformation gradient and strain representations to describe the deformation of brain tissue during mild frontal impact. Chapter 4 uses the wave propagation equation to estimate parameters for brain tissue modeled as an isotropic

viscoelastic medium. The transversely isotropic hyperelastic and linear elastic theory presented above is applied to explain the experimental results in Chapters 5 and 6.

Chapter 3

Relative Brain Displacement and Deformation during Constrained Mild Frontal Head Impact

This chapter describes the measurement of fields of relative displacement between the brain and the skull in vivo by tagged magnetic resonance imaging and digital image analysis. Motion of the brain relative to the skull occurs during normal activity, but if the head undergoes high accelerations, the resulting large and rapid deformation of neuronal and axonal tissue can lead to long-term disability or death. Mathematical modeling and computer simulation of acceleration-induced traumatic brain injury (TBI) promise to illuminate the mechanisms of axonal and neuronal pathology, but numerical studies require knowledge of boundary conditions at the brain-skull interface, material properties, and experimental data for validation. Experimental methods using tagged MR imaging method is presented. A rigid body registration method is applied to extracting the rigid body motion of the skull. Displacement information is acquired by analyzing tagging images. This chapter provides a dense set of displacement measurements in the human brain during mild frontal skull impact constrained to the sagittal plane. Although head motion is dominated by translation, these data show that the brain rotates relative to the skull. For these mild events, characterized by linear decelerations near 1.5G (G=9.81 m/s^2) and angular accelerations of 120-140 rad/s^2, relative brain-skull displacements of 2-3 mm are typical; regions of smaller displacements reflect the tethering effects of brain-skull connections. Strain fields exhibit significant areas with maximal principal strains of 5% or greater. These displacement and strain fields illuminate the skull-brain boundary conditions, and can be used to validate simulations of brain biomechanics.

The material presented in this chapter is published in the Journal of Royal Society Interface (Feng, Abney, Okamoto, Pless, Genin, and Bayly 2010). Feng performed the experiment, analyzed the data, and wrote the manuscript. Abney, Okamoto, and Pless analyzed part of the data, Feng, Genin and Bayly designed the study. Bayly conceived the project. All the authors reviewed and edited the manuscripts.

3.1 Introduction

Traumatic brain injury (TBI) is a complex injury associated with a broad spectrum of symptoms and disabilities. High linear and angular accelerations of the head often lead to diffuse axonal injury, which is generally believed to be responsible for many of the cognitive deficits exhibited by TBI survivors [8]. Although the complete pathway from mechanical insult to cognitive deficit is not fully understood, rapid deformation of brain tissue is a biomechanical feature of most brain traumas. Clear understanding of brain displacement, stretch and stress resulting from head acceleration can help illuminate the pathology of TBI and aid in the development of preventive and therapeutic strategies.

The pattern of brain motion relative to the skull has been a focus of research for decades. Various biomechanical computer models, mostly developed using finite element (FE) methods [13] are aimed at predicting displacement and deformation of brain tissue during head acceleration. The accuracy of these models is uncertain, however, because of the lack of quantitative displacement data for comparison with predictions. The first direct observation of brain motion was performed by replacing the top of a Macacus Rhesus monkey skull with a Lucite calvarium and filming the motion of the brain during under impact [104-105]. This general method was reproduced by [106] and [107]. These experiments confirmed that the brain displaces relative to the skull, and provided qualitative insight into the deformation at the brain surface. However, the transparent replacement materials provide different boundary conditions from the intact skull, and the skull and brain of the animal itself differ significantly from the corresponding human anatomy.

The flash x-ray technique has been used by several investigators to obtain quantitative measurements of internal brain displacement in dogs [108], in primates [109], and in human cadavers [110]. During the impact or acceleration, images of lead particles embedded in the brain of the subject were obtained with high temporal resolution by fast x-ray methods. The density differences between the particles and the brain itself probably affect the displacement field. The imaging technique was improved by the use of a high-speed biplanar x-ray system to image the motion of a small number of neutral density particles in the cadaver brain during high accelerations [111]. In these studies the magnitude of relative displacement of brain was approximately 5mm at the locations of the particles. In a more recent analysis of this data set, the relative motion was separated into rigid body displacement and deformation [112]. These two studies provide quantitative traces of human brain displacement during head impact; the major shortcomings are that the data are spatially very sparse, and that the cadaveric brain is quite different from the intact, living brain.

Magnetic resonance imaging (MRI) provides an alternative approach to investigating brain displacement. A tagged MR imaging protocol was performed to estimate Lagrangian strains in the human brain in vivo during occipital impact [54] and during angular acceleration [113]. In these studies, although strain was estimated from the absolute displacement field, the motion of the skull was not isolated, so that relative displacement between the brain and skull was not obtained. Displacements of the pons region of the brain under neck flexion have also been quantified using MRI techniques [114]; however these data correspond to quasistatic loading.

A number of mathematical models of TBI biomechanics have been developed [18, 23-24, 115-117]. These models use the best available measurements of brain tissue properties and estimates of the interface conditions between brain and skull. However, validation of such models has suffered from the relative paucity of high-resolution experimental measurements of acceleration-induced brain displacement and deformation.

The present study extends our previous work [54, 113], by focusing on the brain displacement with respect to the skull. A landmark point-based image registration method was applied to characterize the rigid-body motion of the skull. Material points in the brain were tracked by "harmonic phase" (HARP) analysis of tagged MR images. The relative displacement of brain tissue with respect to the skull was acquired by expressing the brain displacements in a skull-fixed coordinate system. These results will be valuable for validation of computer models of brain biomechanics and for clarifying the role of the brain's suspension in traumatic brain injury.

3.2 Experimental Design

3.2.1 Imaging Methods

Magnetic resonance imaging provides a non-invasive method for visualizing motion of biological tissue. MR tagging was developed more than 20 years ago [53] as a useful technique for tracking the motion of moving tissue. A sequence of radio frequency (RF) pulses and modulating gradients are applied to modulate the longitudinal magnetization of proton spins (Figure 3.1). Incorporating these steps into a conventional imaging sequence, the sinusoidally-modulated longitudinal magnetization will turn into sinusoidally-modulated transverse magnetization, which leads to light and dark stripes ("tag lines") in the final image. Since the proton spins, which are the source of the signal, move with the tissue, the stripes can be used for tracking the motion of biological tissue [118-119]. We used MR tagging method to keep track of the brain tissue movement inside of skull during constraint mild frontal impact.

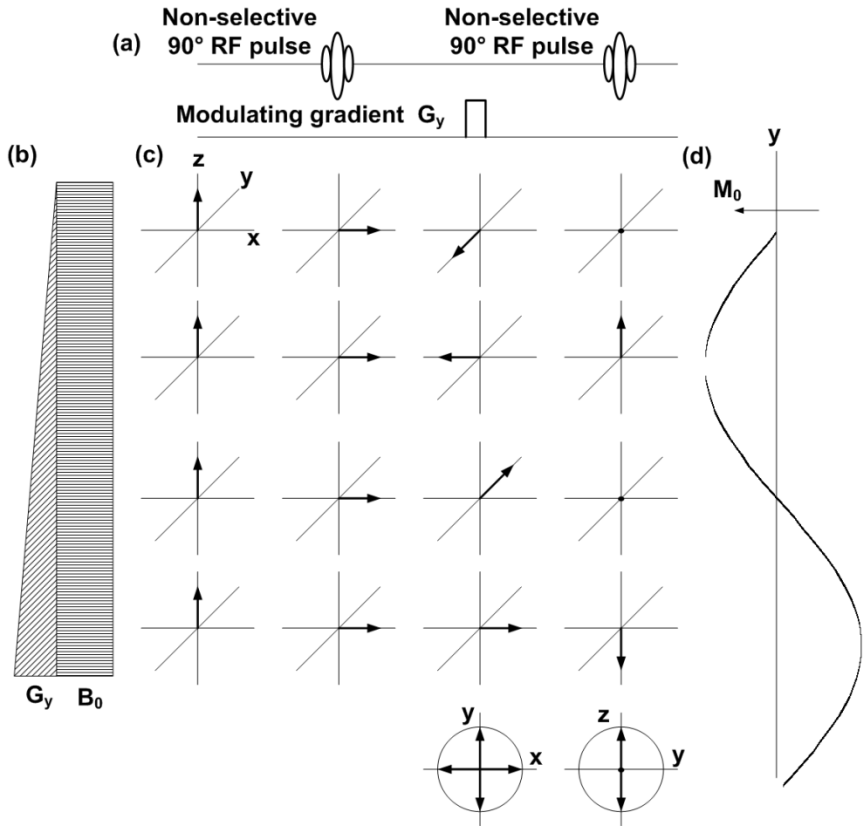

Figure 3.1 MR tagging pulse sequence and spin status. (a) Tagging sequence on top of the figure showing the radio frequency (RF) pulses. (b) Static magnetic field B_0 and modulation gradient along y axis. (c) Proton spins in four difference spatial positions along y-axis (vertical direction) was illustrated by tracking their status through four temporal points (horizontal direction) corresponding to tagging sequence. (d) sinusoidally-modulated longitudinal magnetization along y axis.

3.2.2 Implementation of Controlled Head Acceleration

MR tagging data was acquired from three male human volunteers (age 23–44 years) by a clinical MR scanner (Siemens Sonata 1.5 T; Siemens, Munich, Germany). The synchronization of the head falling and the triggering of the tagging sequence was achieved with a custom-built apparatus (Figure 3.2) was used. The human head was secured in a rigid fiberglass frame, which was placed inside of a standard Siemens head coil. The head was suspended by a broad elastic strap that covered the forehead, and by a soft chin strap, both of which were attached to the fiberglass frame. The frame can rotate about a pivot that allowed constrained motion in the anterior-posterior direction. Upon release of a latch, the frame would drop approximately 2 cm and hit a rubber

stop. The head would be decelerated by the elastic suspension, experiencing acceleration typical of mild frontal impact. Imaging was triggered by an optical sensor that detected the release of the latch, so that image acquisition was synchronized with motion.

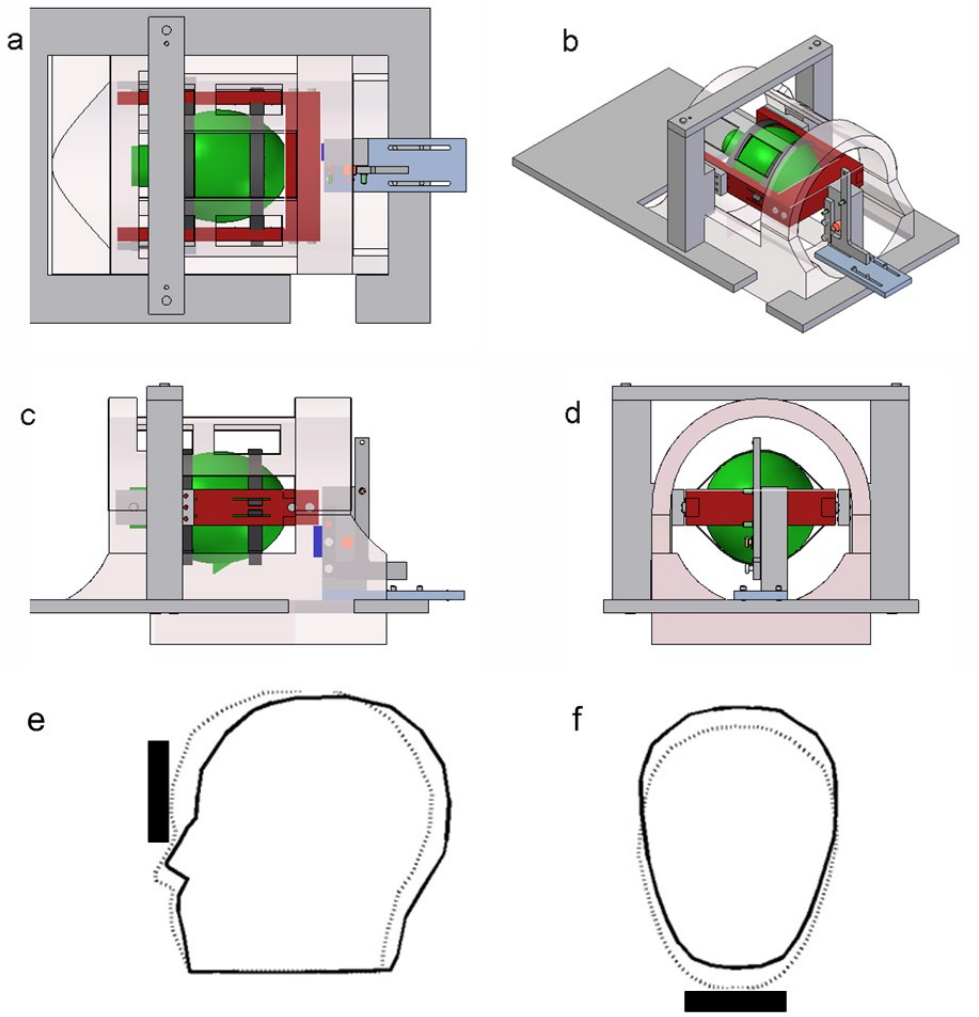

Figure 3.2 (a–d) Digital solid model of the experimental apparatus: top, isometric, side and front views. The head (green) is suspended by elastic straps (black) in a fiberglass frame (red) that can rotate in the sagittal plane to produce a nodding motion of the head. The subject lifts his lead into position, then releases a latch that drops the frame approximately 2 cm onto a stop (dark blue). (e,f) The subject's forehead is restrained by the elastic suspension to produce a mild deceleration similar to frontal impact.

3.3 Image Acquisition and Processing

3.3.1 Image Acquisition

Tagged images were obtained in a sagittal plane of the left hemisphere of each subject (Figure 3.3) offset about 1 cm from the mid-plane of the brain. Tagging sequence was incorporated into a standard fast gradient echo cine pulse sequence (FLASH2D) with repetition time TR = 5.6 ms and echo time TE = 2.9 ms. The frequency domain (k-space) matrix was 144×384 (144 phase-encoding line and 384 readout points). Images were obtained by zero-padding the matrix to 192×384 in the Fourier domain, Fourier transforming and truncating to a 192×192 pixel matrix. The final field of view was 250×250 mm^2 and the slice thickness was 5 mm, corresponding to a voxel size of 1.3×1.3×5 mm^3.

To maximize temporal resolution, the MR image is acquired for one line of k-space at a time; the head drop was repeated once for each line of k-space. For each subject, a total of 120 images was obtained, spanning the duration of the head drop; each image frame was captured every 5.6 ms. The time between the release of the latch (initiation of imaging) and impact with the stop was approximately 40-50 ms, so that the impact typically occurred between the eight and the tenth image. For this reason, we selected the first 30 image frame for analysis. After the first 30 frames (168 ms), the head was almost stationary.

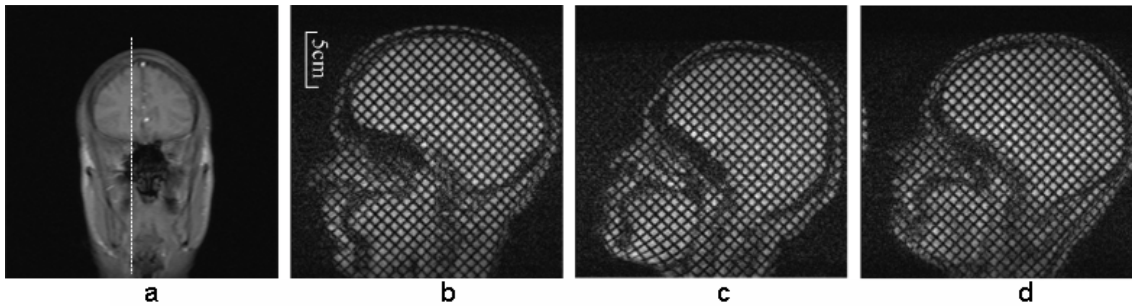

Figure 3.3 (a) Scout MR image showing the sagittal plane used for subsequent dynamic tagged imaging. (b-d) The (undeformed) reference grid pattern obtained by tagged MRI of this sagittal image plane in (b) subject S1, (c) subject S2, and (d) subject S3. (b) Scale bar is 5 cm.

3.3.2 Image Registration

To describe brain motion relative to the skull, the (approximately) rigid-body motion of the skull must be estimated. This was done by registration of landmark points on the skull and on the relatively rigid anatomical features of the head. The Cartesian coordinates of 10 landmark points were manually identified by clicking at intersections of tag lines on the reference image (Figure 3.4a) and at corresponding tag line intersections on subsequent (deformed) images (Figure 3.4b). Displacement vectors between the landmark points in the reference image and the corresponding points in each deformed image are obtained. The origin of a skull-fixed coordinate system was defined in the reference image, near the foramen magnum. We sought the rotation about the axis normal to the image plane passing through this point, combined with translation. This would bring the landmark points in the images of the rotated head into alignment with the landmark points in the reference image. For each image, a minimization algorithm (Nelder–Mead unconstrained nonlinear minimization) implemented in Matlab (fminsearch; The Mathworks, Natick, MA, USA) was used to find the three parameters (rotation, x-translation, y-translation) that minimized the sum of the squared displacements of the 10 landmark points. The parameters obtained for each image were used as initial guesses for registration of the subsequent image. The registration method and results are illustrated in Figure 3.4b,c; the displaced landmark points are plotted on a composite image obtained by summing the images of the displaced head. Rotation and translation are applied to each set of landmark points, and to each greyscale image (using the Matlab function imtransform). The composite image obtained from the sum of the registered skull images and the registered landmark points are shown in Figure 3.4c.

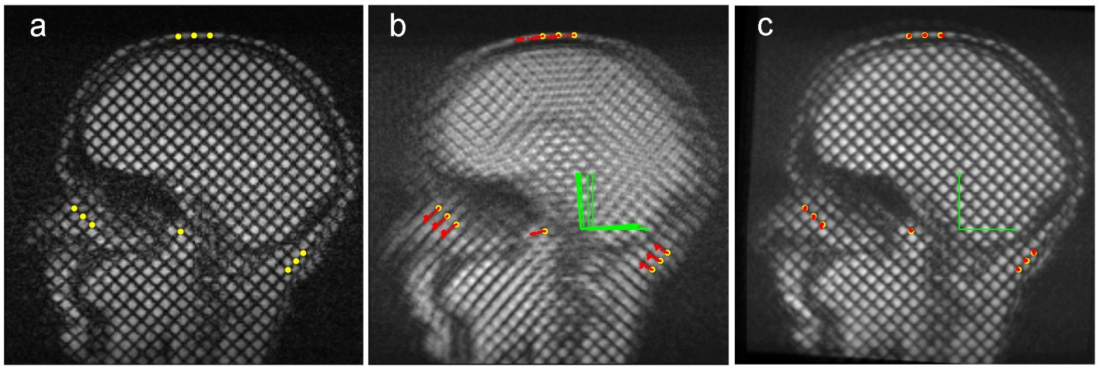

Figure 3.4 Quantification of the rigid-body kinematics of the head by registration of landmark points. (a) Ten landmark points(yellow) located at tag line intersections on extracranial tissue. (b) Trajectories of landmark points during head motion are shown (in red) on a composite image formed from the sum of 12 successive images (2–13). (c) The same set of landmark points (red) are shown after registration on a composite image formed from the sum of 12 successive registered images. Registration was performed by finding the translation and rotation of a reference frame fixed to the skull, which minimized the sum of the squared displacements of all 10 points.

3.3.3 Analysis of Displacement and Strain Fields

The intersections of tagged lines were tracked by identifying contours of HARP [120]. The intersection points of the brain in its deformed configuration were obtained from each MR image (Figure 3.5), and transformed so that they were expressed with respect to the skull-fixed coordinate system. The intersection points in the reference configuration were also obtained from the first MR image (before the drop). The relative displacement field was obtained from the differences in locations of intersection points in the deformed and reference configurations.

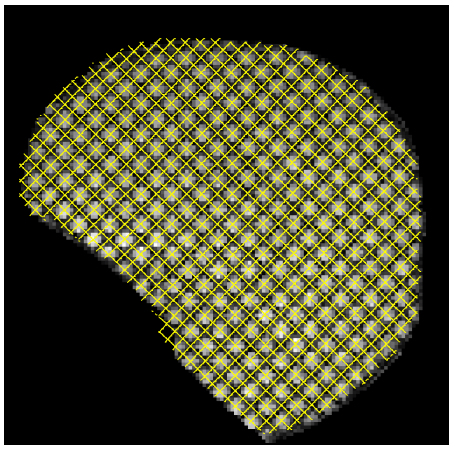

Figure 3.5 A representative image showing tracked tagged lines (yellow line) overlay the MR tagged images.

The strain distribution was obtained from the HARP intersection points via the algorithm presented in [54]. Briefly, the Delaunay method was used to generate a triangular mesh from intersection points in the reference configuration and in the deformed configuration.

Suppose that for each triangle, the sides of the triangle in the reference configuration are the vectors $\boldsymbol{D}_n$(n = 1, 2, 3) and in the deformed configuration, the sides are vectors $\boldsymbol{d}_n$. The two-dimensional deformation gradient tensor $\boldsymbol{F}$ relates corresponding sides in the reference and deformed configurations

$$\boldsymbol{D}_n = \boldsymbol{F} \cdot \boldsymbol{d}_n \tag{2.100}$$

The eigenvalues (λ_1, λ_2) of the deformation gradient tensor are the principal stretch ratios; if an infinitesimal circle is mapped by $\boldsymbol{F}$ from the reference to the deformed configuration, the stretch ratios are the ratios of the major and minor axes of the ellipse to the radius of the undeformed circle. The Lagrangian strain tensor $\boldsymbol{E}$ can be also obtained using Eq. (2.2)-(2.6) Lagrangian strain is unaffected by rigid-body rotations.

3.4 Results

3.4.1 Relative displacements

Estimates of skull motion (linear displacement of a central point, plus rotation about that point) obtained by image registration in all three subjects are shown in Figure 3.6. The peak translational acceleration magnitudes of the skull origin for the three subjects were 14.3–16.3 $m \cdot s^{-2}$. Peak angular accelerations for the subjects' skulls varied from 124 to 143 $rad \cdot s^{-2}$ and occurred fairly uniformly at about 40 ms after latch release (Table 3.1). Displacement vector fields and displacement magnitude fields for subject S1 (Figure 3.7) show a spatially varying, dynamic pattern of relative brain displacement. For subject S1, at 39 ms (just before peak deceleration), most displacement vectors are pointing forward (anterior) but large regions have very small displacement values. From 39 to 50 ms, as the skull decelerates, the anterior components of displacement increase as the brain pitches forward relative to the skull, especially in the mid-superior cortex. Notably, near the cortical surface, the relative displacements are small; despite being surrounded by cerebrospinal fluid, the tangential motion of the surface of the brain is apparently constrained by the skull. By 56 ms, the relative displacement has begun to diminish throughout the brain. A vortex-like feature is seen in the basal central region of the field at 61.6 ms. Subsequent displacement fields (not shown) show relative displacements returning to normal values close to zero.

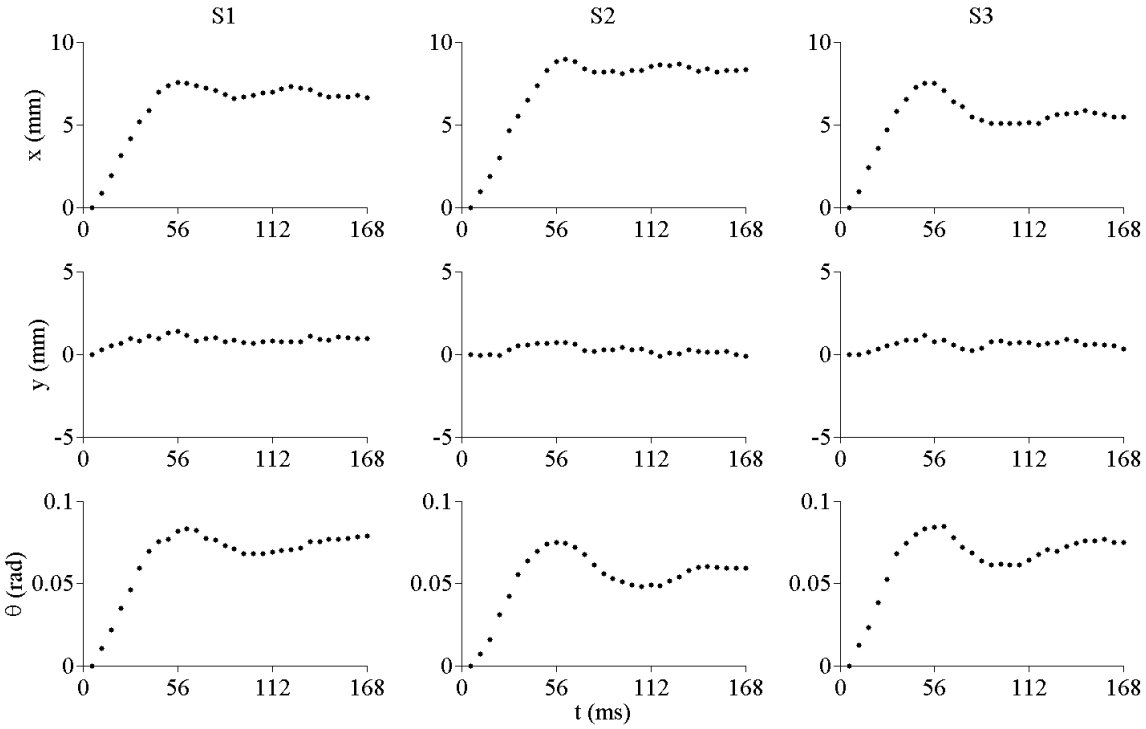

Figure 3.6 Estimated rigid-body motion of the skull in the first 30 images after the head drop is triggered. (a) Displacement of the skull origin (Figure 3.4) in the image x-direction (anterior–posterior, or vertical direction for the prone subject) for subject S1, subject S2 and subject S3. (b) Displacement of the skull origin in the image y-direction (inferior–superior, or horizontal direction for the prone subject) for subject S1, subject S2 and subject S3. (c) Angular displacement of the skull for subject S1, subject S2 and subject S3.

Table 3.1 Maximum magnitude of skull linear and angular acceleration for each subject, and the corresponding time of occurrence. Linear acceleration is estimated at the centroid of the image

	$\|a\|_{max}$ (m/s^2)	Time (ms)	$\|\alpha\|_{max}$ (rad/s^2)	Time (ms)
S1	14.3	44.8	131	39.2
S2	15.8	56.0	124	39.2
S3	16.3	56.0	143	39.2

Figure 3.8 and Figure 3.9 show comparisons of displacement vectors and their magnitudes in all three subjects. The maximum displacement for subject S1 is about 3.5 mm; in subject S2 about 2 mm and in subject S3 about 3 mm. The brains of the two younger subjects (S1, 23 years and S3, 30 years) exhibited more similar timing and slightly larger magnitudes than the brain of the third subject (S2, 44 years). The vortex-like feature noted above in subject S1 is also seen in subjects S2 and S3, indicating that perhaps this feature is a consistent effect of the basal attachment of the brain to skull. Relative displacement was also tracked over time at specific locations (a–d in the upper-right panel, t = 44.8, S3, in Figure 3.9). We examined displacements at material positions in the frontal lobe (a), parietal regions (b), cerebellum (c) and near the pituitary stalk (d). The time series are shown in Figure 3.10. The tissue displacements in all subjects peaked slightly before 56 ms. Larger displacements were observed in the superior cortical locations than in the basal regions (consistent with the 'pitching-forward' rigid-body component of brain motion).

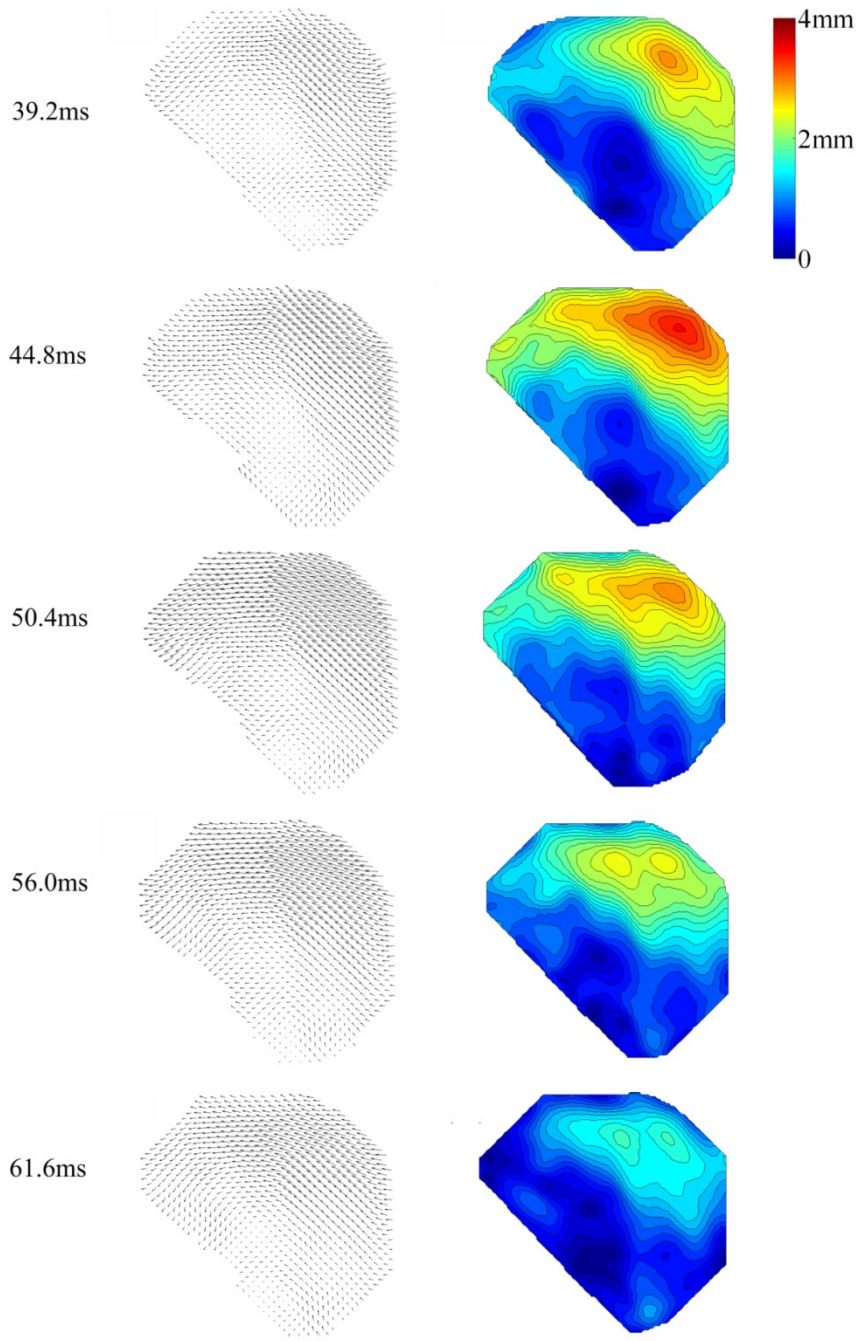

Figure 3.7 (a) Relative displacement vector field and (b) relative displacement magnitude field for subject S1 at t = 39.2 ms (image 7) after release; t = 44.8 ms (image 8); t = 50.4 ms (image 9); t = 56.0 ms (image 10); t = 61.6 ms (image 11).

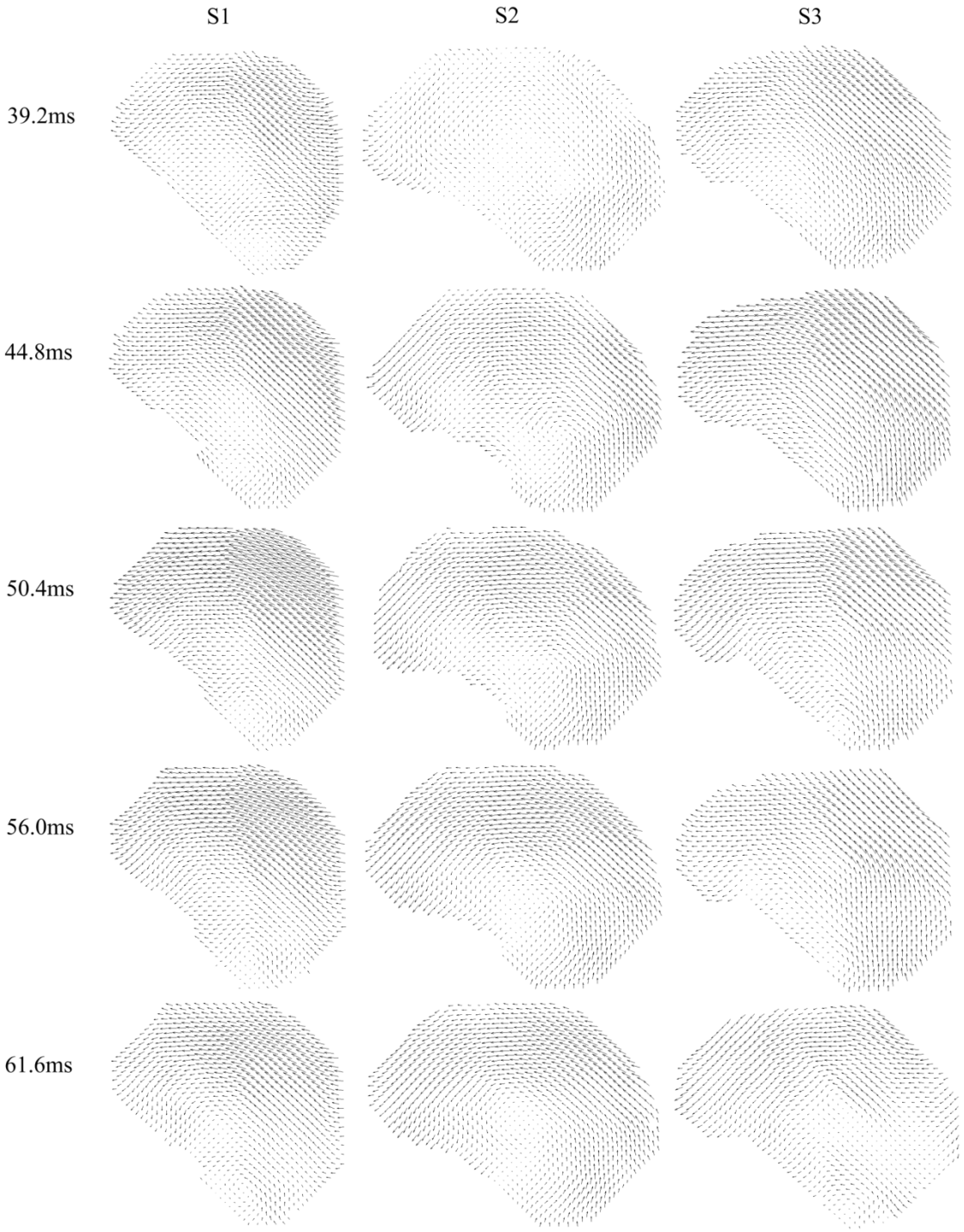

Figure 3.8 Relative displacement vectors, with respect to the skull, of material points in the brain in three subjects (S1, S2 and S3) at specified times after release.

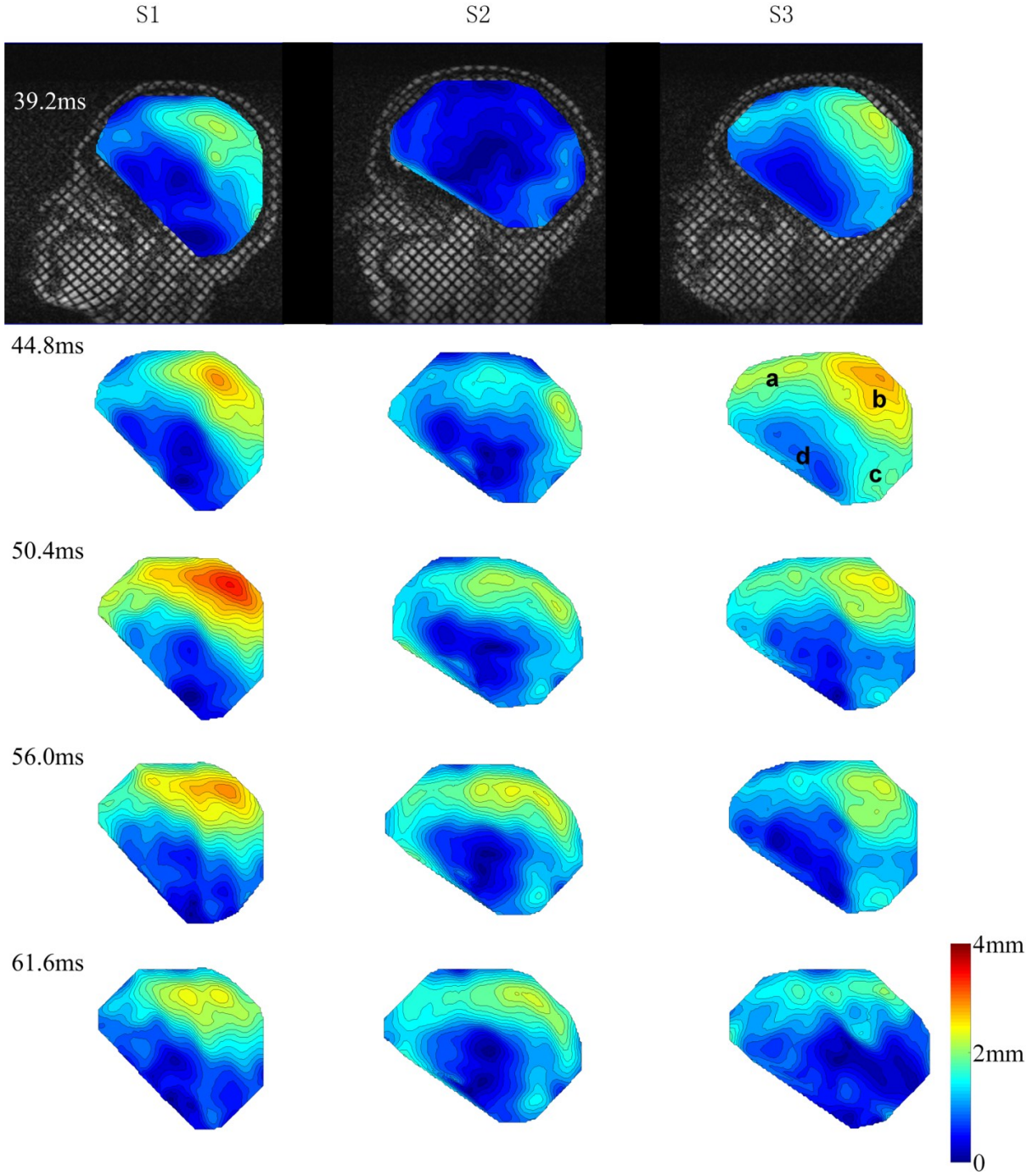

Figure 3.9 Relative displacement magnitudes, with respect to the skull, of material points in the brain in three subjects (S1, S2 and S3), at specific times after release, corresponding to the vector fields in Figure 3.8. The annotations in the upper-right image (S3, t = 44.8) indicate the locations of points at which displacement time series are extracted and shown in Figure 3.10.

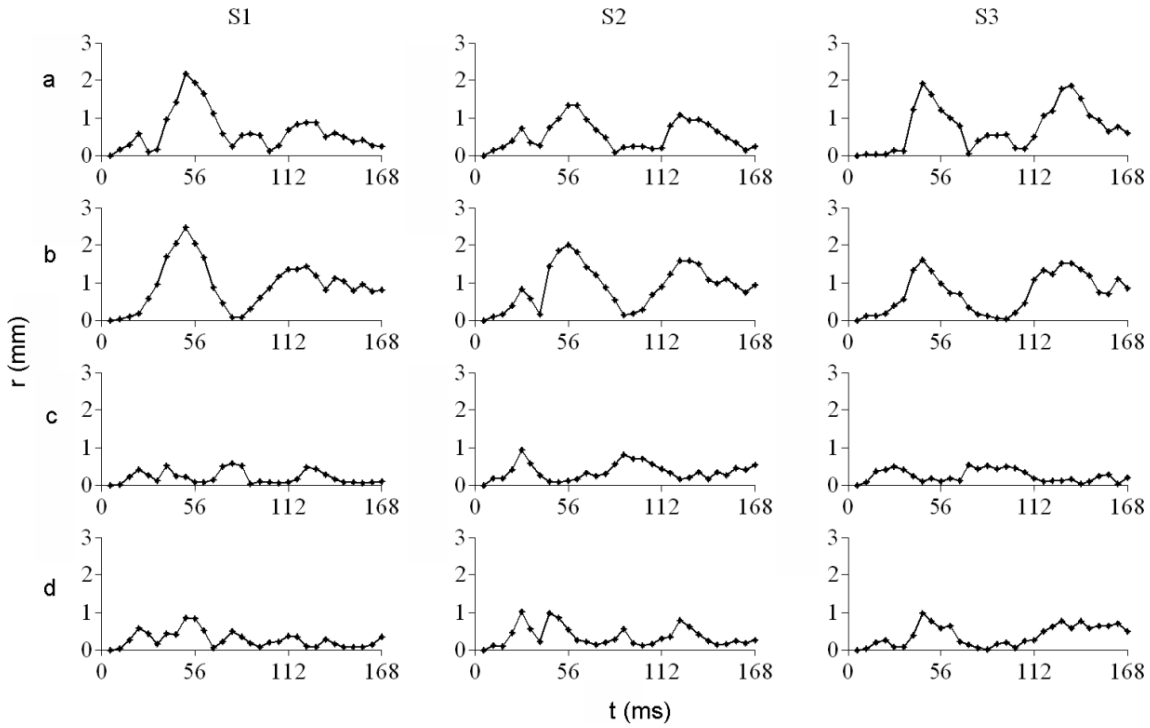

Figure 3.10 Time series of relative brain displacement magnitude in all three subjects at the four material locations (a, b, c and d) indicated in the upper-right panel (S3, t = 44.8 ms) of Figure 3.9, for all three subjects.

3.4.2 Brain deformation

To illustrate deformation, a 'strain ellipse plot' is shown for all three subjects in Figure 3.11. The deformation gradient F is used to transform circles located at different positions of the undeformed brain into corresponding ellipses in the deformed configuration. The ellipses are colored by the corresponding maximum principal stretch ratio λ_1. These deformation fields show diffuse but heterogeneous stretching throughout the brain. The highest levels of stretch and shear are seen at the cortical surface of the brain (including frontal, superior, and occipital sites) and near basal points of attachment of the brain to the skull. Significant regions of the brain exhibit maximal principal stretches of 1.05–1.07 (5–7% elongation) under the conditions of this study. In the Cartesian reference frame with the x-axis aligned in the anterior–posterior direction, and the y-axis aligned inferior–superior, these cortical regions are characterized by strong x–y shear deformations and vertical stretching.

Time histories of the first (maximum) principal Lagrangian strain, ε_1, at the locations identified in Figure 3.9, are shown in Figure 3.12. Though the strain histories are noisier than displacement (largely because strain represents the spatial derivative of displacement), peaks near 5% strain are seen consistently at locations near the superior cortical surface, around the time of peak deceleration. Strains in the inferior central region (site c) are consistently lower than strains near the superior cortical surface (sites a and b).

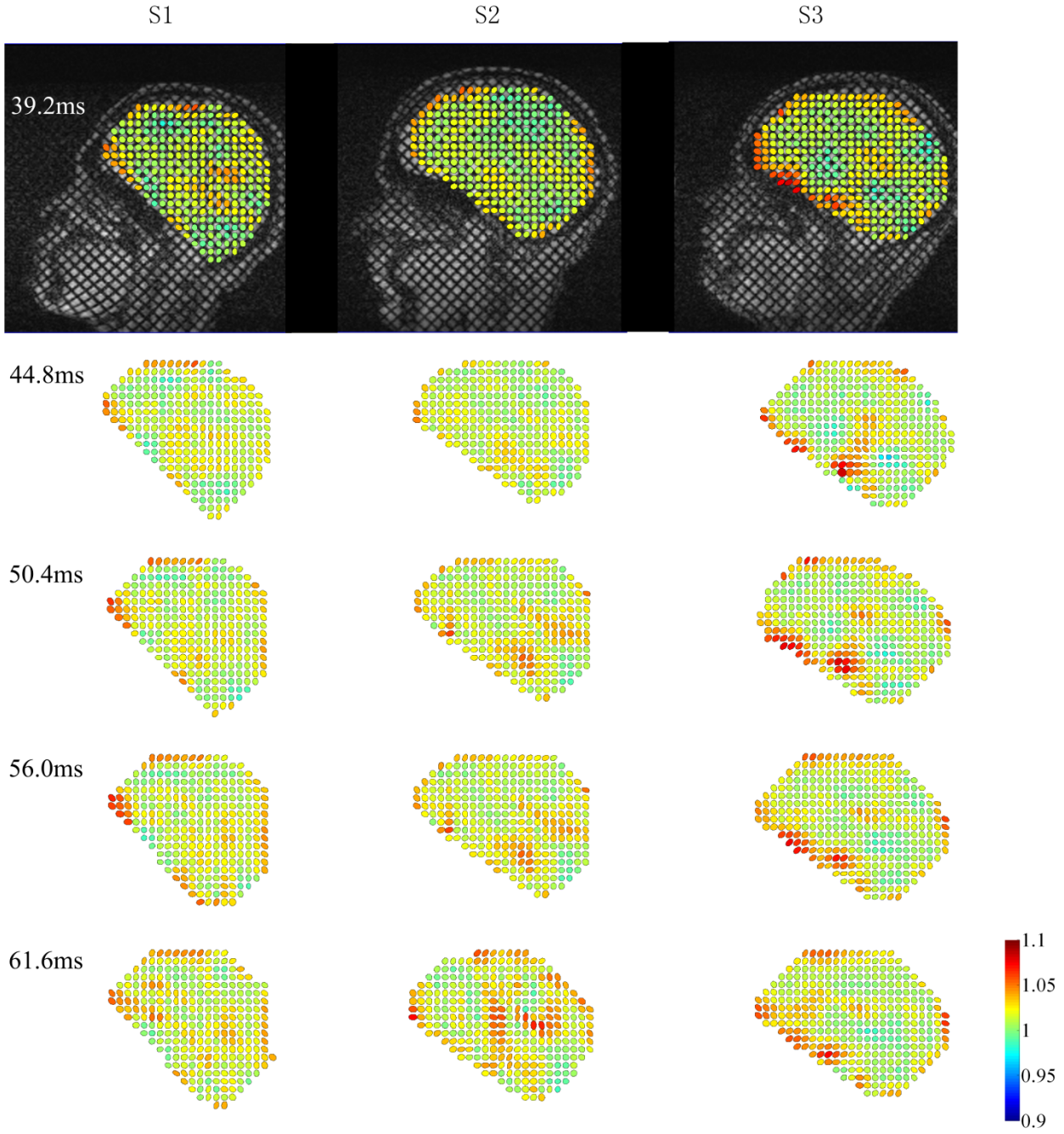

Figure 3.11 Strain ellipse plots for all three subjects at specified time points. Each ellipse is formed by using the deformation gradient tensor to map the undeformed circle into its corresponding elliptical deformed configuration. The centre-to-centre distance between undeformed circles is 6.5 mm and the original radius is 1.9 mm. Each deformed ellipse is colored by its maximum principal stretch ratio λ_1 at the sampled point.

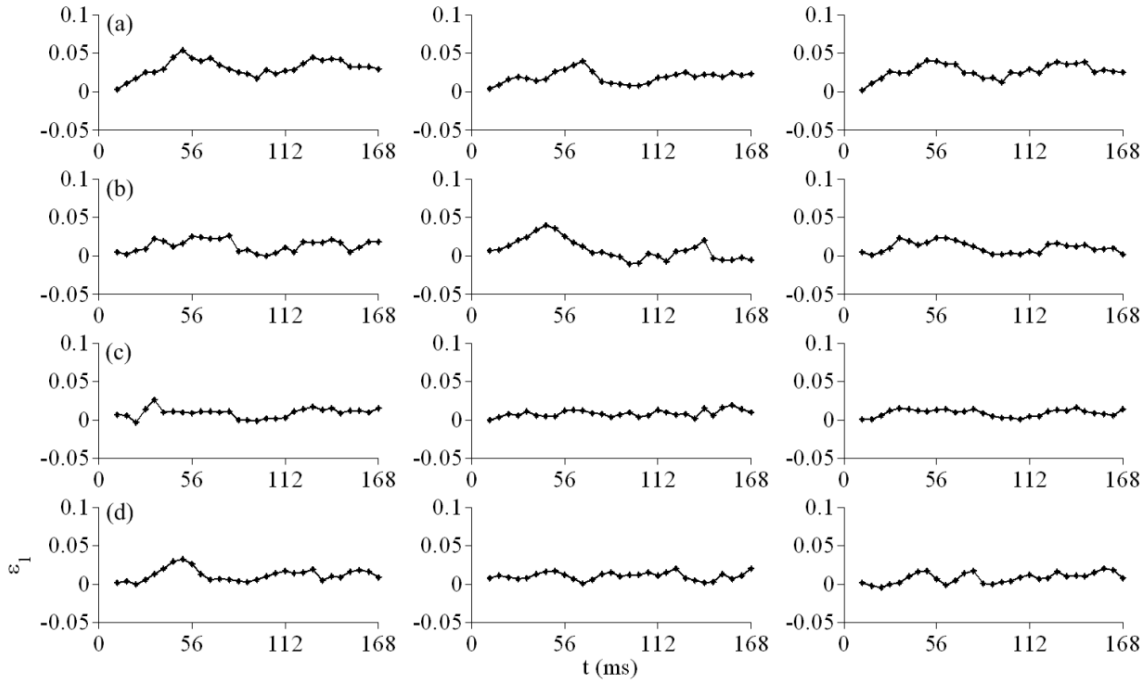

Figure 3.12 Time series of maximum principal strain in all three subjects estimated at the four material locations (a, b, c and d) indicated in the upper-right panel (S3, t = 44.8 ms) of Figure 3.9.

3.5 Discussion

The biomechanics of TBI have been a topic of active research for decades, and computer modeling is becoming increasingly important [24, 115]. Data showing the relative displacements in the brains of human subjects during head acceleration are useful for both the development and validation of simulations. Zhang [115] and several other groups have used human cadaver data from Hardy [111]. These prior data provide useful information on the brain's response to high acceleration, but suffer from limited spatial resolution and spatial coverage, as well as from the differences between cadaveric specimens and live humans. The current study provides well-resolved fields of relative displacement in the brains of live human subjects during mild acceleration, showing the time-varying, non-uniform distribution of relative displacement in a 2D sagittal plane. Oscillating patterns of displacement between the brain and skull were found, due both to relative rigid-body motion and deformation. The small experimental sample, which

spans a relatively large age range, shows distinct individual differences in relative brain displacement under similar acceleration loading.

The patterns of displacement and deformation can be partially explained by the following scenario. Connections between the skull and brain exist at the brain stem, and at various vascular, neural or membranous connections at the base and boundary of the brain. Very roughly, the brain can be thought of as a mass suspended by springs in a rigid container (Figure 3.13). Impact or rapid deceleration of the container will induce oscillation of the mass, which is grossly analogous to the motion of the brain inside the skull [14]. This simplified model also illustrates why the brain has the large displacement magnitude at the boundaries and the displacement near the base is usually smaller. It appears as though the attachment of the brain to the skull is firmest at its base, so that the deceleration of the skull induces brain rotation as well as translation [112].

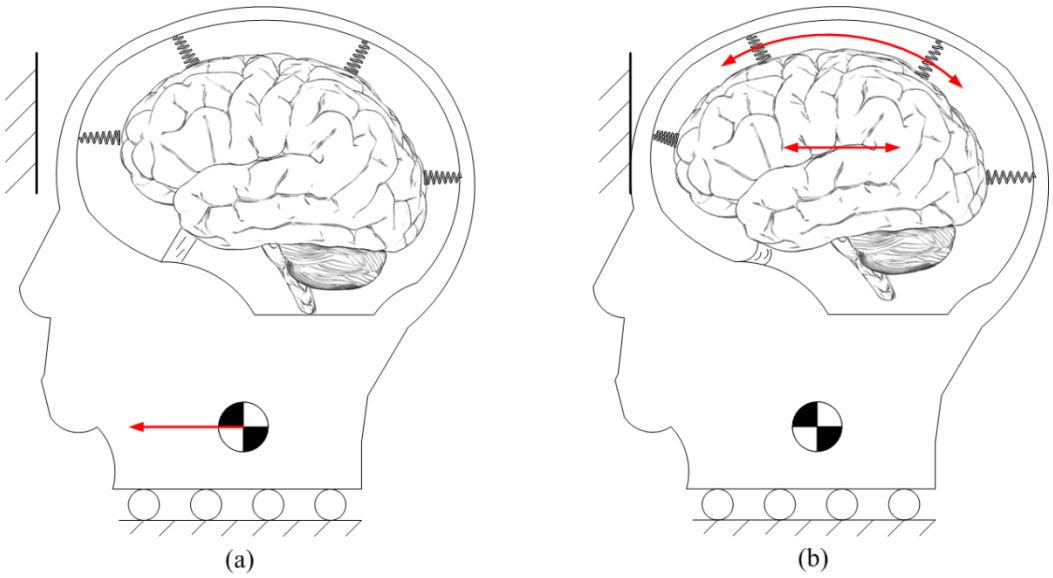

Figure 3.13 A highly simplified model for the gross motion of the brain in its elastic suspension. The skull is shown in pure translation. The elastic element at the base and the springs at the perimeter represent the brain's attachments to the skull. Note that linear deceleration of the skull leads to both linear and angular displacement of the brain relative to the skull.

Contrary to this simple model, however, displacement in the brain does not reflect only rigid body motion; rather the spatially and temporally varying displacement field reflects dynamic deformation (Figure 3.7, Figure 3.8). A vortex-like pattern in the displacement field arises near the time of peak deceleration (Figure 3.7, Figure 3.8). This reflects the

apparent shearing deformation of soft brain tissue. The occurrence of peak relative brain displacement around the time of maximal deceleration is consistent with simple physical models, and with observations from previous studies of the anesthetized monkey brain [109]. Deformation is characterized by spatial gradients of the displacement field. Here we illustrate deformation by "strain ellipse" plots (Figure 3.11), which also exhibit oscillatory (Figure 3.12), spatially varying patterns. In all the subjects, at different times, large stretches occur near the superior surface of the cortex, in basal frontal regions, and at the back of the occipital lobe. These features all appear to show the brain pulling away from attachment points, rather than compressing due to contact with the walls of the skull. Tethering at the base of the brain is likely to contribute to these strain patterns. Stiff anatomical features in this region that connect brain to skull and penetrate the soft brain parenchyma include bony prominences, internal carotid arteries, the optic nerves, the olfactory tracts, the oculomotor nerves, and the pituitary stalk.

Our results are generally consistent with those reported by earlier investigators, such as Hodgson et. al. (1966) [108], Hardy et al. (2001)[111], and Zou et al. (2007)[112]. Hardy et al. (2001) [111]show that the displacement-time curve in the impact direction has a sinusoidal shape for all three of their cadaveric subjects. In the work of Hardy et al. (2001) [111], the peak linear accelerations angular accelerations are at least two orders of magnitude greater than those of the current study, but the magnitude of displacement is only about 4-5mm (~50% more than our results). This may be due to (1) nonlinear effects (the brain makes contact with the walls of the skull; slack in vessels and membranes is taken up), (2) differences between cadavers and live humans (the cadaveric brain is likely much stiffer than the live brain) and (3) the viscoelastic stiffening of the brain and other soft tissue at high strain rates. The duration of acceleration is also longer in the current study. Zou et. al. (2007)[112] note in their studies of neutral-density markers that relative brain-skull displacement magnitudes increased very little as skull accelerations increased from 12g to 100g (120 m/s^2 – 1000 m/s^2).

The methods of the current study are aimed at providing a comprehensive map of displacement in a 2D section of the brain. This is in contrast, for example, to the complementary study of Hardy et al. (2001) [111] in which displacement was obtained at only the few locations where neutral density targets were located. However, the high accelerations used in the study of Hardy et al. (2001) [111] are directly relevant to TBI; the accelerations used in the current study probe only the response to sub-injury levels of acceleration. Ji (2007) [114] investigated the quasi-static motion of the pons inside the skull by comparing in vivo MR images of the undisplaced and displaced pons. The displacement field was obtained with an auto-correlation technique with resolution on the order of pixel size. The point-based registration method used in the current study proved preferable because motion artifact in MR images can confound grayscale-based registration methods. The current method can provide sub-pixel accuracy, given accurate manual identification of landmark points. Zou et al. (2007) [112] separated the relative displacement of the brain with respect to the skull into a rigid body component and a deformation component. However, Zou et al. (2007) [112] used the spatially sparse data from the study by Hardy et al. (2001) [111]. The current study provides complementary information: higher spatial resolution over a larger spatial domain, but at lower accelerations.

The current study is limited to motion of the brain and skull in a sagittal plane during mild decelerations approximating frontal impact. Since the deceleration is in this plane, and the plane is near the midline of the symmetric brain, out-of-plane displacements are expected to be much smaller than in-plane displacements. If volume invariance is assumed, the magnitude of out-of-plane stretching or compression can be estimated from the in-plane change in area, since the determinant, J, of the deformation gradient (the product of the principal stretches) is unity. Using this estimate, out-of-plane strains do not exceed 1% in this study. However, the effects of out-of-plane motion may not be negligible. It is almost certain that anatomical features outside the image plane affect the motion of points in this plane. Such features include the falx cerebri, the tentorium, various vessels, bony prominences, and membraneous sheaths of major nerves. By increasing the number of imaging planes, 3D displacement fields can be constructed. However, using the current technique, this would require more repetitions of impact,

which are undesirable in human subjects. Extension of this technique to an animal model would facilitate the acquisition of more complete spatial information, but would be less relevant to the problem of human brain injury. Temporal resolution in the current study is 5.6 ms, obtained by a standard "fast, low angle" (FLASH2D) gradient echo imaging sequence. More advanced fast imaging techniques should allow increased temporal resolution in future studies. Accuracy of image registration relies on good image quality (high signal-to-noise, low blurring) and high resolution, which are competing goals of the MR pulse sequence. The current set of MR pulse sequence and sequence parameters appears to provide an appropriate compromise, which, again, may be improved by new MR sequences in future work.

In conclusion, this study provides the first comprehensive, high resolution, quantitative data on the relative displacement of the brain with respect to the skull caused by mild frontal impact. The results can be used to validate models of brain trauma, understand mechanisms of TBI and improve the understanding of the mechanical properties of brain tissue. This approach complements both experimental studies of the cadaveric and animal brains under high accelerations, and numerical studies of injury mechanics in the human brain. Future studies will aim to continue to improve our quantitative knowledge of the kinematics of the human brain during linear and angular skull acceleration.

Chapter 4

Characterization of Brain Tissue by Magnetic Resonance Elastography

Although mechanical testing of brain tissue provides valuable data for characterizing brain tissue, in vivo characterization is still indispensable. Characterization of the dynamic mechanical behavior of brain tissue is essential for understanding and simulating the mechanisms of traumatic brain injury (TBI). Changes in mechanical properties may also reflect changes in the brain due to aging or disease. In this chapter, we used magnetic resonance elastography (MRE) to measure the viscoelastic properties of ferret brain tissue in vivo. Three-dimensional (3D) displacement fields were acquired during wave propagation in the brain induced by harmonic excitation of the skull at 400 Hz, 600 Hz and 800 Hz. Shear waves with wavelengths on the order of millimeters were clearly visible in the displacement field, in strain fields, and in the curl of displacement field (which contains no contributions from longitudinal waves). Viscoelastic parameters (storage and loss moduli) governing dynamic shear deformation were estimated in gray and white matter for these excitation frequencies. To characterize the reproducibility of measurements, two ferrets were studied on three different dates each. The estimated storage modulus[1] (G') and loss modulus (G'') increased over the measured frequency range in both gray matter and white matter. White matter in the ferret brain generally appears to be slightly stiffer and more dissipative than gray matter, especially at lower frequencies. These measurements of shear wave propagation in the ferret brain can be used to both parameterize and validate finite element models of brain biomechanics.

[1] Note the complex shear modulus ($G^* = G' + iG''$) used in this Chapter is the same as $\mu^* = \mu' + i\mu''$, which is stated in Eq. (2.94). Chapters 5 and 6 will keep the same notation as in Eq. (2.94).

The material in this chapter has been submitted for publication in the Journal of Biomechanics (Feng, Clayton, Chang, Okamoto, and Bayly 2012). Feng and Chang performed the experiment. Feng analyzed the displacement, strain, and curl data, and wrote the manuscript. Clayton analyzed the elastogram data. Feng, Okamoto, and Bayly designed the study. Bayly conceived the project. All the authors reviewed and edited the manuscript.

4.1 Introduction

Mathematical modeling and computer simulations can illuminate the mechanics of traumatic brain injury (TBI) [24, 115-116], but only if the parameters of the model are accurate. Because of their importance to the understanding of TBI [3], the mechanical properties of brain tissue have been studied for over half a century [26]. Although many *ex vivo* studies of brain tissue have been performed, such as indentation tests [32, 121] or shear testing [30, 49] , in vivo data is needed to understand the response of intact, living brain tissue.

Magnetic resonance elastography (MRE) has proven useful for in vivo measurement of biological tissue properties [57, 122]. MRE has been applied to study many human organs, including liver [59, 123], breast [70], and brain [59-61, 124-128]. The initial inversion methods of MRE were based on the assumption of linear, isotropic, elastic material behavior. Recent studies have extended the application of MRE to more general viscoelastic models [59, 71, 123]. Understanding the viscoelastic response of brain tissue is particularly important to the study of TBI, since it is inherently a dynamic phenomenon.

Although studies of the human brain provide essential and directly relevant information for human TBI, animal studies are indispensable. Several groups have used MRE to investigate the mechanical properties of brain tissue in rodents such as mice [64, 66, 129-130] and rats [67] in vivo. However, the rodent brain does not contain large distinct white matter regions. Ex vivo MRE studies have been performed in the brains of large

mammals such as the cow [63] and pig [41], but tissue parameters may be affected by post-mortem time and tissue handling. Only Pattison et al. [131] has used MRE to study the differences between white and gray matter tissue properties in a small animal (feline) model in vivo; they considered only a pure elastic model.

In the current study we estimate viscoelastic properties of white and gray matter in the ferret brain in vivo at several frequencies. The ferret is the smallest mammal with a folded brain, and its brain has a significant volume of white matter. The ferret is a well-known animal model for the study of brain development processes, such as cortical folding [79, 132-134]. In this study, we choose the ferret for its combination of small body size and the features of its brain (folds and white matter tracts) that are shared with larger mammals, including primates. To perform the study, a custom apparatus was designed using an MR-compatible piezoelectric actuator to excite the skull through a vibrating bite bar. Phase contrast MR images proportional to displacement were acquired during the propagation of shear waves in the brain. The 3D displacement fields were then inverted to estimate viscoelastic properties of white and gray matter.

4.2 Methods

4.2.1 Experimental Methods

Two adult female ferrets (Marshall Bioresources, New York) were used for this study. Each ferret was scanned three times at 1-2 week intervals, each time with 400 Hz, 600 Hz, and 800 Hz vibration frequencies. Anesthesia was induced with 4% isoflurane before the scan, and maintained with 2% isoflurane in 1.0 L/min oxygen during the scan. To keep the ferret physiologically stable, warm water (45°C) was circulated through tubes under its body. The experimental protocol was approved by the Institutional Animal Studies Committee and studies were supervised by the Division of Comparative Medicine (DCM) at the Washington University School of Medicine.

The head of the ferret was placed in a custom-built head-holder with ear supports, a nose cone for delivery of isoflurane anesthesia, and a bite bar (Figure 4.1). A low-pass, "birdcage" quadrature coil [135], which could both transmit and receive radiofrequency (RF) signals was positioned around the head-holder and the animal. Shear waves in the brain were induced by vibration of skull transmitted via the bite bar. A harmonic signal was generated by a function generator (FG-7002C, EZ Digital Co.,Ltd., Korea), amplified by a piezo amplifier (EPA-102, Piezo Systems Inc., Cambridge, Massachusetts) and used to drive a piezo-ceramic actuator (APA150M-NM, Cedrat Technologies, France) connected to the bite bar. The ferret's teeth were hooked over the bite bar; preloading of the teeth against the bite bar was accomplished by sliding the nose cone to provide light pressure against the animal's snout.

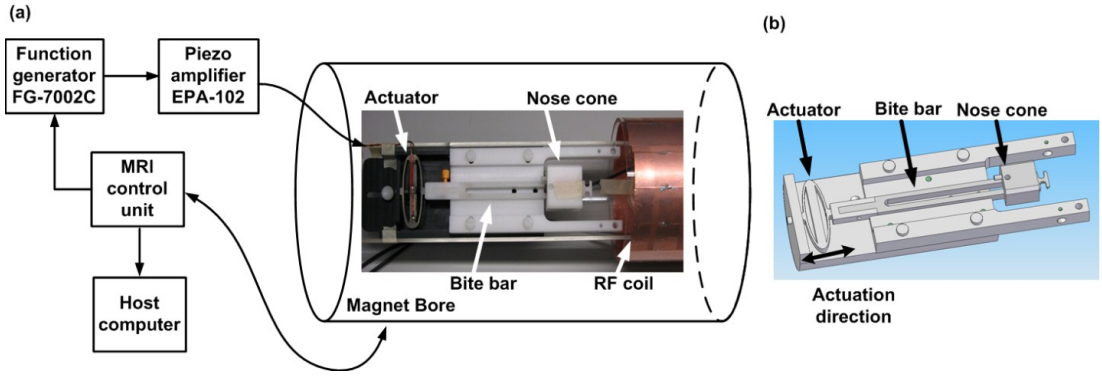

Figure 4.1 (a) Setup for inducing and imaging mechanical waves in the ferret brain. The piezoelectric actuator generates mechanical vibration at frequencies of 400, 600, and 800 Hz, which was transmitted through the bite bar to the teeth. The teeth were pre-loaded against the bite bar by adjusting the nose cone position. The RF coil served as both the transmitting and receiving coil for MRI. (b) Schematic view showing the position detail of actuator, bite bar, and nose cone. The direction of actuation is along the long axis of the bite bar, which is anterior-posterior with respect to the skull.

A 4.7 T superconducting MRI scanner (Varian, Inc.) was used to acquire images. A gradient-echo, multi-slice (GEMS) imaging sequence was modified with motion-sensitizing gradients (Figure 4.2) to measure the dynamic displacement of the brain. Motion-encoding gradients were synchronized with mechanical waves at frequencies of 400, 600, and 800 Hz. In each harmonic wave cycle, four or eight temporal points were acquired by varying the phase shift θ between the motion-sensitizing gradient and the mechanical wave. The imaging field of view (FOV) was 48 mm × 48 mm with an image

matrix of 96 × 96 voxels. A total of 11 slices were acquired, with a slice thickness of 0.5 mm, and no gap between each scanned slices. No cardiac or respiratory gating was used. The scan parameters for each actuation frequency are summarized in Table 4.1.

Table 4.1 MRE scanning parameter

Frequency (Hz)	400	600	800
Repetition time -TR (ms)	200	200	350
Echo time - TE (ms)	13	13	26
Flip Angle (°)	25	25	40
Motion encoding cycles (N)	4	6	16
Measurement time (min)	16	16	27

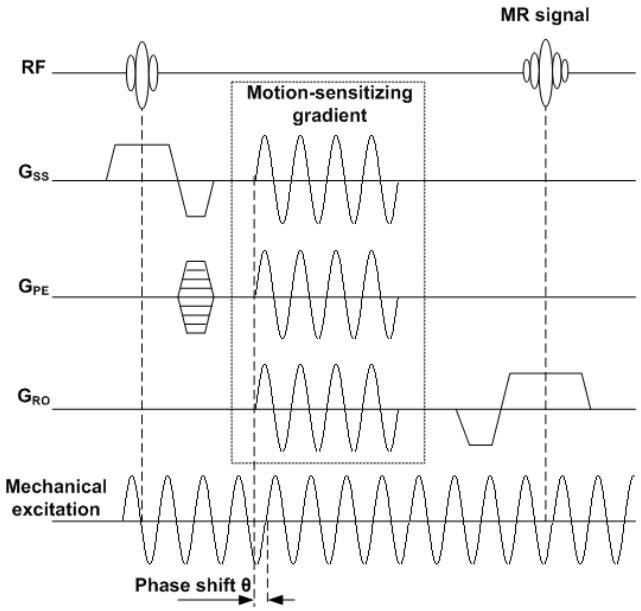

Figure 4.2. Gradient-echo multi-slice (GEMS) MRE sequence. The motion encoding gradient can be applied in any or all of the three directions in Cartesian coordinates. The phase shift $\boldsymbol{\theta}$ between mechanical excitation and motion-sensitizing gradient was chosen to be either $[0, \pi/2, \pi, 3\pi/2]$, or $[0, \pi/4, \pi/2, 3\pi/4, \pi, 5\pi/4, 3\pi/2, 7\pi/4]$ within one sinusoidal motion cycle.

4.2.2 Data Processing

The phase ϕ of the MR signal and the displacement $\boldsymbol{u}$ are related by the magnetic field that the spin packet experiences as it moves. If the displacement and the motion-

sensitizing gradient oscillate at the same frequency, a simple relation can be obtained between ϕ and the projection of displacement onto the direction of the motion-sensitizing gradient: $u_G = \frac{\omega\phi}{\gamma\pi N G_0}$ [64]. Here ω is the vibration frequency, γ is the gyroscopic ratio of a hydrogen proton, N is the number of motion-sensitizing gradient cycles, and G_0 is the amplitude of the motion sensitizing gradient. By applying the motion-sensitizing gradient in three orthogonal directions, we acquired phase images $\phi_n, n = 1,2,3$ corresponding to the 3D displacement vector field, $\boldsymbol{u}$ ($u_n, n = 1,2,3$).

MR phase images were first unwrapped by a modified 3D quality guided flood-fill phase unwrapping algorithm [136], to eliminate the 2π ambiguity which is inherent in phase measurements. Data were temporally filtered by Fourier transforming in time and keeping only the fundamental frequency (the dominant frequency component). Then the images were spatially filtered with a 3D Gaussian filter (convolution kernel 3 × 3 × 3 pixels, standard deviation 1 pixel).

The strain field was calculated by numerical differentiation:

$$\varepsilon_{mn} = \frac{1}{2}\left(\frac{\partial u_m}{\partial x_n} + \frac{\partial u_n}{\partial x_m}\right). \tag{6.1}$$

According to the Helmholtz theorem [71, 137-139] , the displacement vector field $\boldsymbol{u}$ can be decomposed into a curl-free ("longitudinal") component ($\boldsymbol{u}_L$) and a divergence-free ("transverse") component ($\boldsymbol{u}_T$). The transverse, or shear, displacement component ($\boldsymbol{u}_T$) describes volume-conserving deformation ($\nabla \cdot \boldsymbol{u}_T = 0$). The curl of the displacement field, which contains no contributions from longitudinal waves is obtained using:

$$curl(\boldsymbol{u}) = \nabla \times \boldsymbol{u} = \epsilon_{mnk} \frac{\partial u_n}{\partial x_m} \boldsymbol{e}_k, \tag{6.2}$$

where ϵ_{mnk} is the permutation symbol and $\boldsymbol{e}_k$ is the base vector of the Cartesian coordinate.

4.2.3 Parameter Estimation

The governing equations of shear wave propagation in an isotropic, linearly elastic material are presented in Chapter 2, Eq. (2.95). The complex shear modulus at each local pixel can be calculated by using Eq. (2.99), which is a local result that can be used, in theory, to estimate the complex shear modulus at every voxel in the image volume. In practice, numerical differentiation is required to estimate the second derivatives in the Laplacian, and the fit is performed in a 3 × 3 × 3 voxel fitting region. The normalized residual error of each fit was computed [129]; estimates of parameters were rejected if normalized residual error >0.5. This general procedure was performed first by applying Eq. (2.99) to the displacement field $\boldsymbol{u}$, and second by applying Eq. (2.99) to the curl of the displacement field (i.e., replacing the components of displacement in Eq. (2.99) with the components of the curl) [129]. The second approach was implemented in order to eliminate contributions from longitudinal waves, at the cost of an additional numerical spatial derivative.

4.3 Results

All the MRE images were acquired in the coronal plane (Figure 4.3). To construct a 3D displacement volume for analysis, 11 slices (Figure 4.4) were scanned. The x-y plane of the Cartesian coordinate defines the coronal plane (Figure 4.4). By activating the motion-sensitizing gradient along different directions, all three displacement components (u_x, u_y, u_z) in the Cartesian coordinates were acquired during MRE.

Representative 3D displacement fields acquired at actuation frequencies of 400 Hz (Figure 4.5a) and 600 Hz (Figure 4.5b) show a shear wave propagating in the y-direction (inferior-superior). The dominant displacement component is along the z-direction

(anterior-posterior), with a maximum magnitude about 11.2 μm for 400 Hz and 7.4 μm for 600 Hz. The displacement field at 800 Hz is qualitatively similar, with lower amplitude and shorter wavelength.

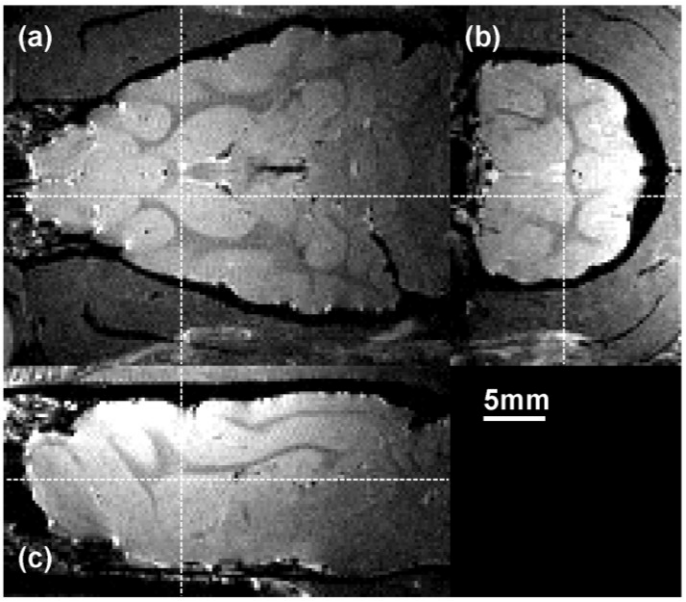

Figure 4.3 (a) Transverse view, (b) coronal view, and (c) sagittal view of ferret brain anatomy images (spin echo: T2W; TR = 4000 ms, TE = 25 ms) showing the field of view (FOV) with a pixel size of 0.25 mm x 0.25 mm. The white lines on the transverse slice indicate the position of the coronal and sagittal imaging planes.

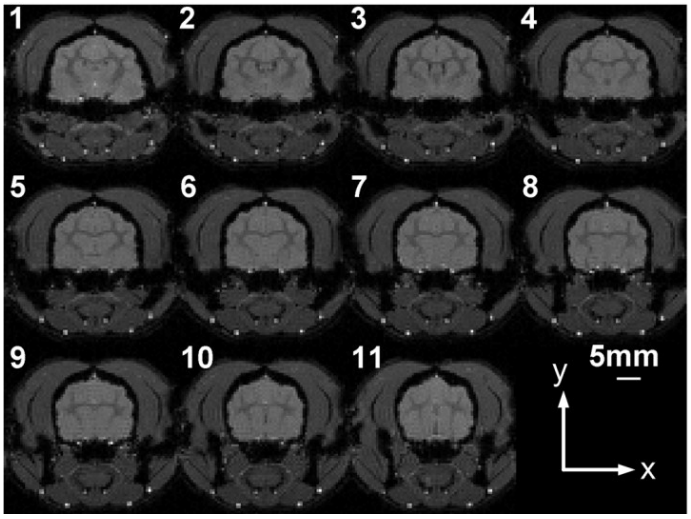

Figure 4.4 Eleven coronal image slices obtained by a standard gradient echo multi-slice (GEMS) imaging sequence (TR = 500 ms; TE = 20 ms). The same image slices were used in MRE. The FOV is 36 mm × 36 mm with a pixel size of 0.5 mm x 0.5 mm. The slice thickness was 0.5 mm with no gap between each slice.

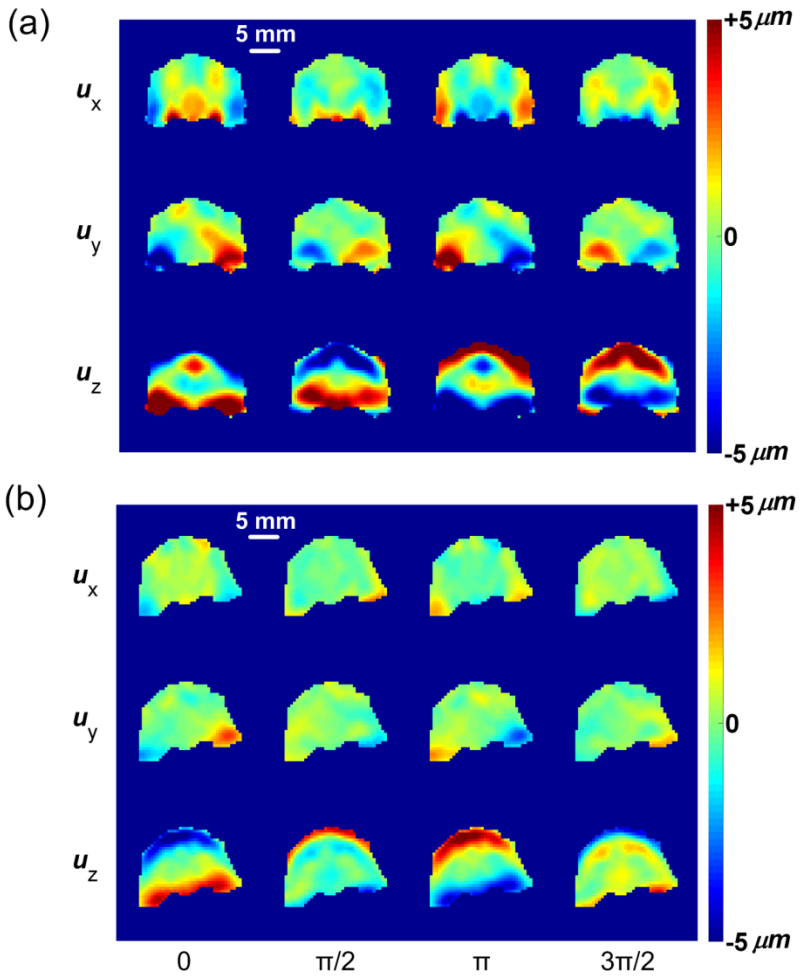

Figure 4.5 Displacement fields at (a) 400 Hz and (b) 600 Hz actuator frequencies. Four phases of the periodic motion ($0, \pi/2, \pi, 3\pi/2$) are shown in sequence from left to right. Three displacement components in x (left-right), y (inferior-superior), and z (anterior-posterior) directions in Cartesian coordinates are shown. Scale bar in each panel are 5 mm.

The normal and shear Cartesian components of strain are shown in Figure 4.6 for 400 Hz (Figure 4.6a) and 600 Hz (Figure 4.6b). At these actuation frequencies we see clear wave propagation in the y-direction dominated by the ε_{yz} component of shear. Using the approximation for strain $\varepsilon = \varepsilon_0 \, e^{i\omega t}$, we estimate strain rate as $\dot{\varepsilon} = i\omega\varepsilon_0 \, e^{i\omega t}$, and thus maximum strain rates are approximately 16 s^{-1} for 400 Hz, 20 s^{-1} for 600 Hz, and 25 s^{-1} for 800 Hz. Curl fields for 400 Hz (Figure 4.7a) and 600 Hz (Figure 4.7b) indicate that a volume-conserving transverse wave traveling in the y-direction is the major component of the response to external vibration in the z-direction. The curl field wave pattern is consistent with the wave pattern observed in the ε_{yz} component.

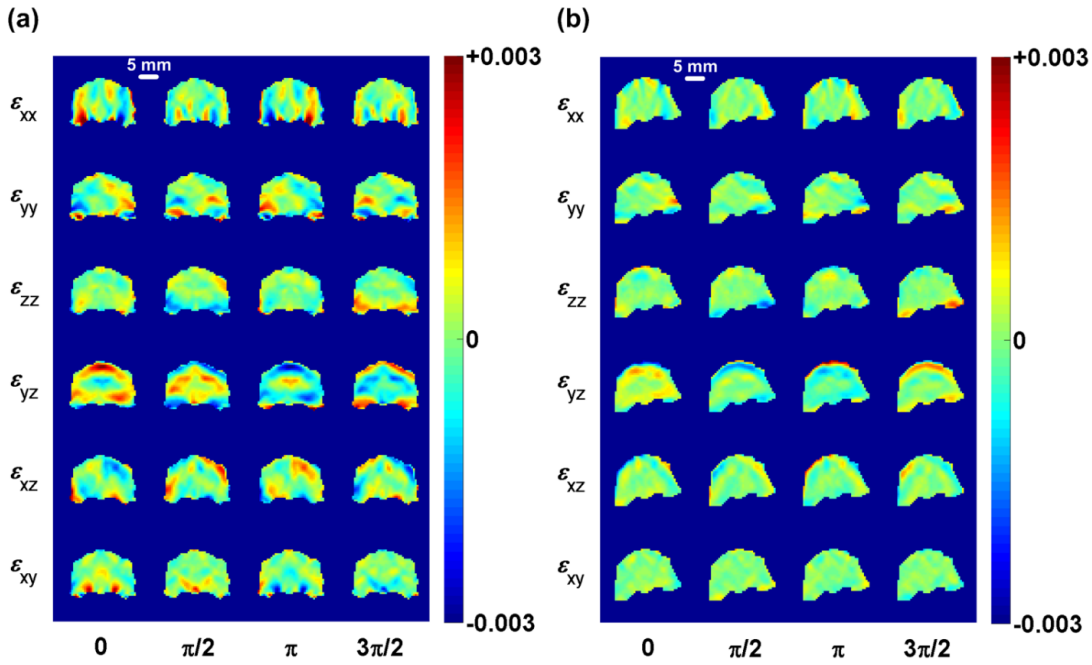

Figure 4.6 Normal and shear components of the strain tensor in Cartesian coordinates at four phases ($\phi = 0, \pi/2, \pi, 3\pi/2$) of the periodic motion. (a) 400 Hz and (b) 600 Hz. Scale bars shown at the top of each panel are 5 mm.

Representative elastograms for 400 Hz, 600 Hz, and 800 Hz actuation frequencies are shown in Figure 4.8 (a-f). Elastograms obtained using the curl of the displacement field (Eq. 2) (Figure 4.8 (d-f)) are shown together with those obtained from the raw displacement field (Figure 4.8 (g-i)). A map of average octahedral shear strain $\varepsilon_{oct} = \frac{2}{3}\sqrt{(\varepsilon_{xx}-\varepsilon_{yy})^2+(\varepsilon_{xx}-\varepsilon_{zz})^2+(\varepsilon_{yy}-\varepsilon_{zz})^2+6(\varepsilon_{xy}^2+\varepsilon_{xz}^2+\varepsilon_{yz}^2)}$ [140] for 400 Hz, 600 Hz, and 800 Hz actuation frequencies (Figure 4.8 (g-i)) indicates the contrast-to-noise ratio (CNR) of the measurement. Higher octahedral shear strain ε_{oct} generally implies higher confidence in local parameter estimates obtained by MRE.

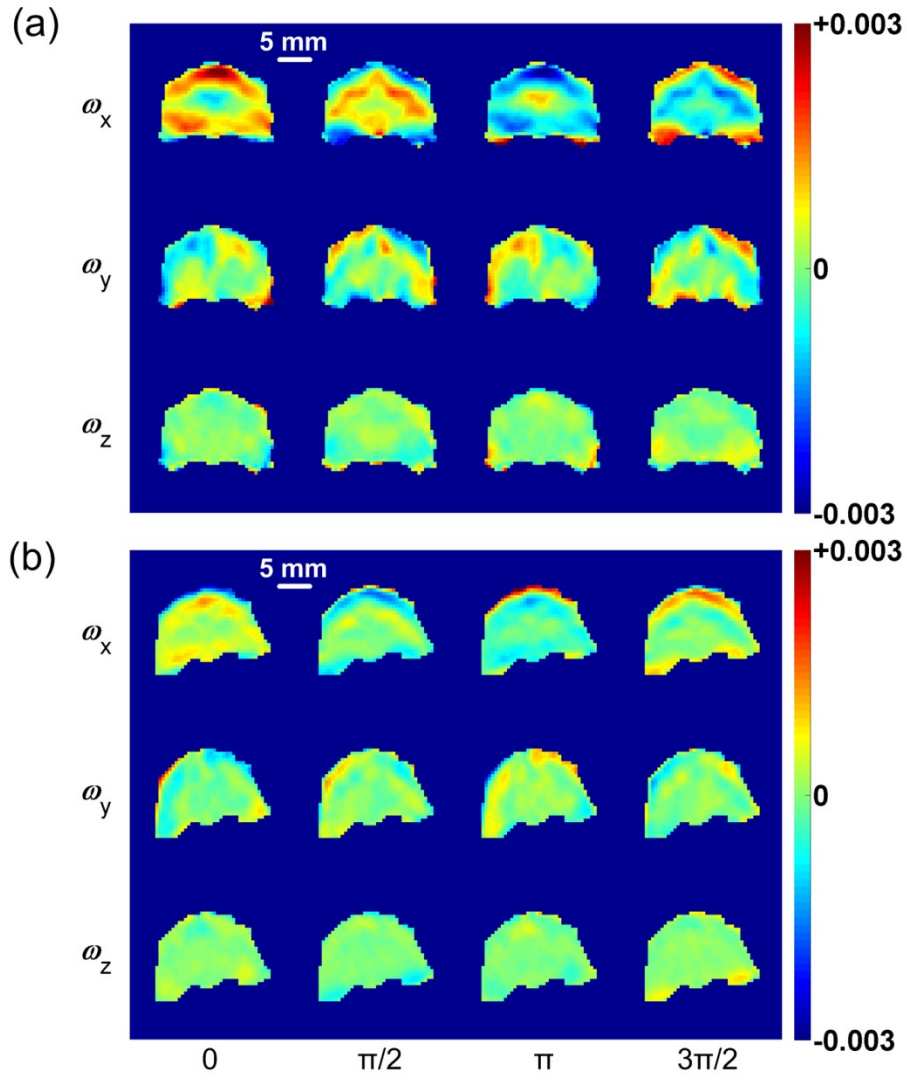

Figure 4.7 Curl fields $= \nabla \times \boldsymbol{u}$. The ω_x, ω_y, and ω_z components are shown at four temporal points in one motion cycle at (a) 400 Hz and (b) 600 Hz. Scale bars at the top of each panel are 5 mm.

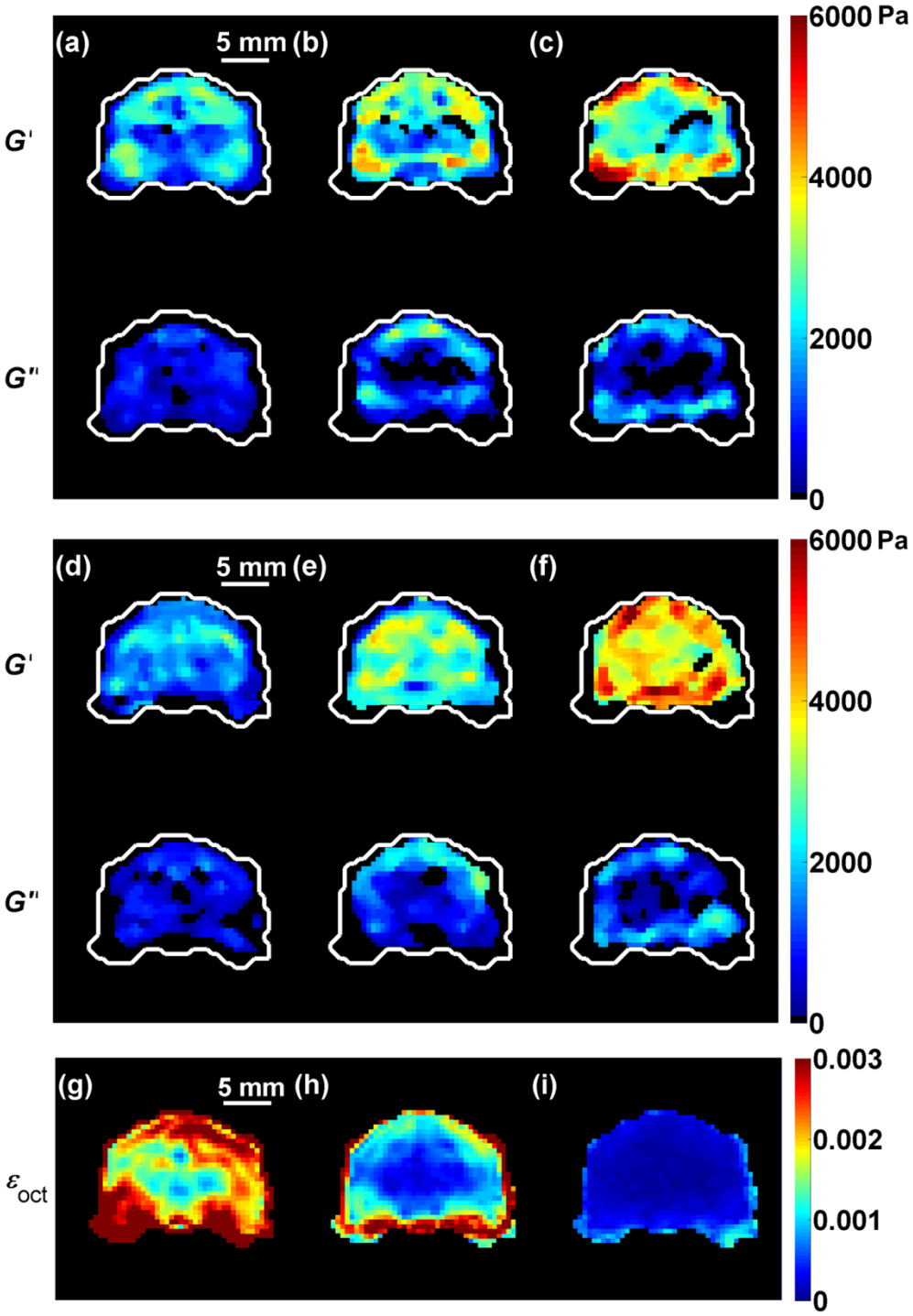

Figure 4.8 Storage (G') and loss (G") modulus estimates for (a, d) 400 Hz, (b, e) 600 Hz and (c, f) 800 Hz actuation frequency for one ferret. Parameter values were estimated from displacement fields before (a-c) and after (d-f) applying the curl operation. White outlines indicate region over which modulus estimates were attempted – black areas within the outlines indicate regions where normalized residual error of fitting exceeded 0.95. Corresponding average octahedral shear strain (ε_{oct}) [140] for for (g) 400 Hz, (h) 600 Hz and (i) 800 Hz indicates the effective contrast-noise-ratio (CNR) of the measurements.

The white and gray matter regions of interest were identified by applying to each elastogram a selection mask based on the anatomic image of the same slice (Figure 4.9a). A summary of shear moduli values for all three frequencies from both displacement and curl fields (Figure 4.9 (b-e)) shows that the white and gray matter viscoelastic properties are very similar between the two ferrets. Overall statistics for both animals of the parameter estimated from the curl fields are summarized in Table 4.2. At all three frequencies, estimates of loss modulus (G'') of white matter obtained by both methods are larger than those of gray matter. Estimates of storage modulus (G') in white matter and gray matter are similar at all three frequencies; white matter appears slightly stiffer at lower frequency. Due to the small number of animals these results were not tested for statistical significance, but these relationships are consistent both between animals and among repeated tests in the same animal.

Table 4.2 Values of shear and loss modulus estimated from the curl field

	White matter		Gray matter	
Frequency (Hz)	G' (kPa)	G'' (kPa)	G' (kPa)	G'' (kPa)
400	1.64±0.15	0.63±0.10	1.37±0.08	0.58±0.11
600	3.14±0.30	1.50±0.27	2.85±.21	1.33±0.17
800	4.64±0.52	1.74±0.53	4.81±0.38	1.78±0.30

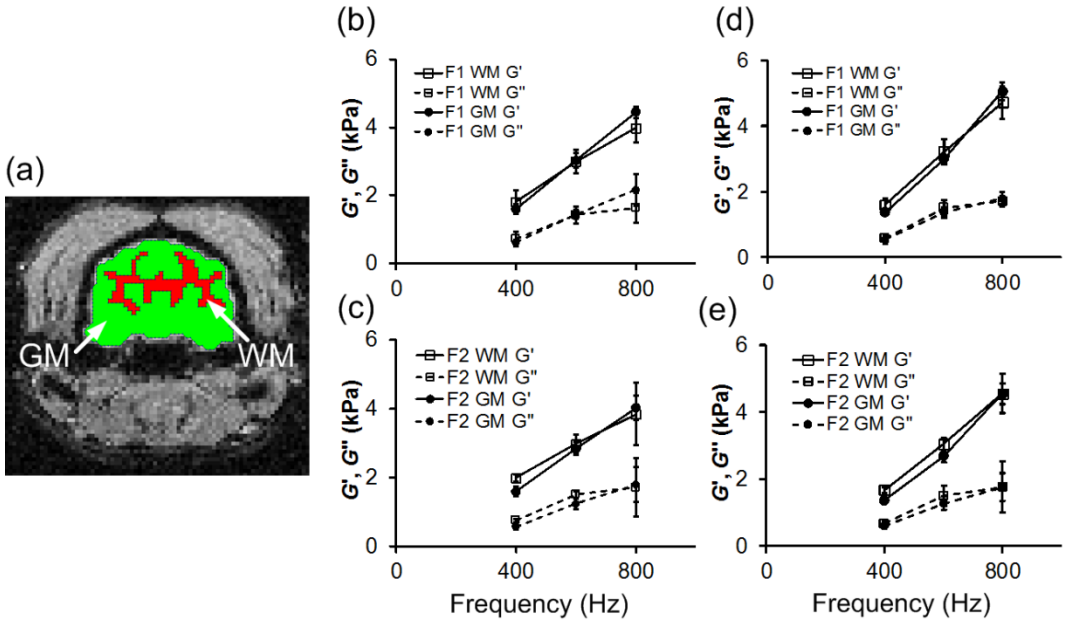

Figure 4.9 (a) White matter (WM, shaded in red) and gray matter (GM, shaded in green) segmentation for ferret brain. Viscoelastic parameters (mean ± std. dev., storage modulus, G', and loss modulus, G'') of white and gray matter at 400 Hz, 600 Hz, and 800 Hz for (b) ferret F1, and (c) ferret F2 estimated from the displacement field; and for (d) ferret F1, and (e) ferret F2 estimated from the curl of the displacement field. Statistics are based on three different scan dates for each ferret.

4.4 Discussion

Quantitative measurements of white and gray matter viscoelastic material properties were performed in living ferrets using MRE measurements of harmonic shear wave propagation at 400, 600, and 800 Hz. A clear wave propagation pattern was observed in the ferret brain under external vibration of the skull, which was applied in the anterior-posterior direction via a piezo-electrically-driven bite bar. The complex shear modulus (storage and loss moduli) were obtained by fitting the 3D displacement fields obtained by MRE to the equations of shear wave propagation in a viscoelastic medium.

Our estimates for the viscoelastic parameters of ferret brain fall within the range of parameters of elastic and viscoelastic models estimated by MRE in other animal and human studies. Ferret white matter and gray matter appear similar to mouse brain tissue at similar frequencies [129], which exhibited average storage modulus 1.6-8 kPa and loss

modulus 1-3 kPa over a frequency range from 600-1800 Hz. MRE estimates of viscoelastic parameters of the human brain, which were obtained at lower frequencies, are comparable to the current estimates: white matter G'=3.3-4.7 kPa, G''=1.3-2.4 kPa; gray matter G'=2.8-4.4 kPa, G''=0.8-2.3 kPa [127]. The current results extend a recent MRE investigation of the elastic parameters of the feline brain at 85 Hz [131] in which (purely) elastic shear modulus was estimated to be 8.32 ± 3.67 kPa in white matter and 7.09 ± 2.78 kPa in gray matter. Many ex vivo studies of material properties have been performed [26]; our estimates fall within the broad range of observed parameter values from ex vivo studies. Some of the variations in ex vivo parameter estimates are attributable to differences in tissue handling and experimental procedures. Comparison between parameter estimates from different studies highlights the effect of excitation frequency. In the current study, we observe that the complex shear modulus increases strongly with increasing frequency, which has also been observed in other MRE studies [59, 68, 71, 123, 129].

We found that the complex shear modulus of white matter is generally slightly greater than that of gray matter; this is consistent with observations from human studies performed at lower excitation frequencies [124, 127-128, 141]. As an exception, we note that at the highest frequency in the current study (800 Hz), white matter exhibits a slightly smaller storage modulus than gray matter. The loss modulus of white matter is greater than the loss modulus of gray matter at every frequency, which indicates that white matter is more dissipative than gray matter. Although Pattison et al. [131] did not consider dissipation, they also noted that white matter appears stiffer than gray matter at 85 Hz. Most small animal MRE studies using mice [64, 66, 129] or rats [67] did not analyze white and gray matter tissue properties separately, because of the small amount of white matter. The study of Schregel et al. [130] is an exception; these authors estimated the shear modulus magnitude in white matter to be approximately 10 kPa at 1000 Hz. The relatively large percentage of white matter tissue in the ferret brain, compared to the rodent brain, provides an opportunity to study the mechanical heterogeneity of white and gray matter over larger regions. Ex vivo mechanical tests of adult ferret brain tissue [79] suggested that white matter tissue is stiffer than gray matter. The indentation strain rate in the study by Xu et al. [79] was much lower than the MRE

actuation frequency in the current study, so that the effective modulus was observed to be lower as well, however both studies indicate heterogeneity between white and gray matter.

In this study, 3D image volumes of 3D displacement fields were acquired by MRE. 3D MRE provides more accurate estimates of shear modulus than 2D MRE, because only 3D imaging can accurately characterize wave propagation in directions out of the 2D imaging plane. 2D MRE has been suggested to generate upper bounds on estimates of material parameters [142], because 2D projections of 3D wave fields will appear to have longer wavelengths and thus lead to higher estimated moduli.

We acknowledge several limitations and caveats to this study. The shear modulus inversion method in the current study is based on an isotropic viscoelastic material model. Although this model is likely to be accurate for gray matter, which is structurally isotropic, it neglects the anisotropy of white matter, which is composed of myelinated axonal fibers. White matter may exhibit shear moduli that differ by 30-50% for shear in planes parallel or perpendicular to the local fiber direction [49, 143-146].The study by Romano et al. [146], performed in humans at lower frequencies than the present study, is the first MRE study to systematically address the issue of anisotropy in white matter; their approach requires the simultaneous acquisition of diffusion tensor images. in the current study, the estimated G' and G'' values tend to be slightly lower when estimated from the curl of the displacement field, rather than from raw displacement data. This is likely due to the fact that the curl operation eliminates the effects of longitudinal waves , which in soft tissue have longer wavelength than shear waves [147]. Modulus maps estimated from curl also appear more homogeneous than those estimated directly from displacement. However, both sets of estimates are quantitatively and qualitatively similar and both sets show that the storage (G') and loss (G'') shear moduli increase with frequency. We interpret the combined results as reasonable lower and upper bounds on the parameter values. Furthermore, the linear viscoelastic models used for inversion are strictly applicable only to small deformations. The deformations in this study clearly fall within that category. Complementary studies (likely including ex vivo mechanical tests) will be needed to understand the behavior of brain tissue at large strains. However, the

in vivo 3D results of the current study provide an important limiting case, since more general models valid for large strain should be consistent with appropriate linear models in the infinitesimal limit.

Chapter 5

Preliminary Study of Transversely Isotropic Material

This chapter develops a mechanical testing protocol for characterizing transversely isotropy in soft biological tissue, based on the combination of dynamic shear testing (DST) and asymmetric indentation. The procedure was demonstrated by characterizing a nearly incompressible transversely isotropic soft material. A soft gel with controlled anisotropy was obtained by polymerizing a mixture of fibrinogen and thrombin solutions in a high field magnet (B=11.7 T); fibrils in the resulting gel were predominantly aligned parallel to the magnetic field. The device setup of DST and indentation is described, along with the testing protocols for characterizing material anisotropy. Aligned fibrin gels were subject to dynamic (20–40 Hz) shear deformation in two orthogonal directions. The shear storage modulus was 1.08±0.42 kPa (mean±std. dev.) for shear in a plane parallel to the dominant fiber direction, and 0.58±0.21 kPa for shear in the plane of isotropy. Gels were indented by a rectangular tip of a large aspect ratio, aligned either parallel or perpendicular to the normal to the plane of transverse isotropy. Aligned fibrin gels appeared stiffer when indented with the long axis of a rectangular tip perpendicular to the dominant fiber direction. This approach enables the estimation of a complete set of parameters for an incompressible, transversely isotropic, linear elastic material. The testing procedures described in this chapter provide experimental foundations for characterization of brain tissue described in chapter 6.

The material presented in this chapter is published in the Jornal of Biomechanical Engineering (Namani, Feng, Okamoto, Jesuraj, Sakiyama-Elbert, Genin, and Bayly, 2012). Feng did the DST test and analyzed the DST data, Namani did the indentation

test, analyzed the indentation data, and wrote the manuscript, Okamoto analyzed the data, Namani, Feng, and Jesuraj made the fibrin gel. Okamoto, Sakiyama-Elbert, Genin, and Bayly conceived the project. All the authors reviewed and edited the manuscript.

5.1 Introduction

Mechanical anisotropy is a feature of many soft tissues [39, 70, 148]. The dependence of the mechanical response on the direction of loading arises from microstructural features such as collagen fiber bundles. The mechanical characterization of anisotropic materials is a fundamental challenge because of the requirement that the responses to multiple loadings must be combined to develop even a linear elastic material characterization [149].

Our specific interest is brain tissue, which presents additional experimental challenges because it is delicate and highly compliant (moduli lie in the 0.1-1 kPa range) [26]. Brain tissue contains both white matter (myelinated axonal fibers), which is structurally anisotropic, and gray matter, which has no apparent structural anisotropy. Brain tissue mechanics are central to mathematical models of brain biomechanics and might be an important determinant of injury susceptibility [13]. Such models would ideally include the complete characterization of the anisotropic mechanics and structure-function relationships in brain tissue. However, techniques involving stretching, such as biaxial stretch plus indentation [150], are not feasible for brain tissue, because of the difficulty of gripping specimens. Cyanoacrylate adhesives have been used to hold samples in tension [46], however, the use of adhesives preclude testing a single sample in more than one direction. (The requirement for multiple loading scenarios to characterize anisotropic materials restricts test procedures to those that do not permanently alter the mechanics of a specimen.) Furthermore, fibrous anisotropic materials may exhibit different properties when loaded in tension and compression, because fibers stretch in tension, but may buckle in compression.

As a first step towards anisotropy of brain tissue, this chapter develops and demonstrates a procedure for finding the complete set of parameters of a transversely isotropic linear elastic model for a soft gel undergoing small strain. The proposed procedure involves the combination of dynamic shear and asymmetric indentation tests, which are promising methods for probing mechanical anisotropy in brain tissue because they require only simple fixtures to hold the sample, and they are non-destructive at small strains. This chapter shows that the combination of these two tests can be used to determine all of the parameters of an incompressible transversely isotropic linear elastic material. Shear tests, performed in the plane of isotropy and in a plane perpendicular to the plane of isotropy, uniquely identify two distinct shear moduli. Indentation with a rectangular tip, as proposed by Bischoff [151] applies different stresses to the material in directions parallel and perpendicular to the long axis of the tip. Thus, a different force-displacement curve will be obtained depending on whether the long axis is aligned with the predominant fiber direction.

Several groups have measured the mechanical properties of brain tissue either by symmetric indentation [152] or by dynamic shear testing (DST) alone [27, 39]. Dynamic shear testing can characterize anisotropy in a shear modulus, if the plane in which the shear is applied is either parallel or normal to the dominant fiber direction. It is very difficult, however, to use DST to illuminate the contribution of fiber stretch to the mechanical response. Studies using symmetric indentation or unconfined compression alone do not detect anisotropy. Cox et al. [153] used an inverse algorithm to extract anisotropic hyperelastic parameters using both the force-displacement curve from symmetric indentation and the principal stretches (determined by viewing the material under the tip with an optical microscope) combined with a computational model. However, the principal stretches are difficult to determine reliably, and require significant additional instrumentation. In contrast, the proposed asymmetric indentation method requires only the force-displacement curves, interpreted in the context of corresponding numerical simulations.

In this chapter, we demonstrate the combined shear-indentation approach by applying it to characterize the linear elastic properties of an anisotropic fibrin gel. Fibrin gel can be

made anisotropic by allowing the gel to polymerize in a high magnetic field, which leads to a network with a preferred fiber axis aligned with the magnetic field [154]. The mechanical properties of this network depend on fiber bending and rotation; hence, they are related to the orientation of fibrils [155]. Thus, fibrin gel is suitable for testing as a brain-mimicking material. The following sections describe the theory and methods behind the use of combined shear-indentation procedures to measure the mechanical parameters of soft transversely isotropic materials

5.2 Fibrin Gel Preparation

Human plasminogen-free fibrinogen (EMD Biosciences, La Jolla, CA, product No. 341578) was dissolved in stris-buffered saline (TBS) (33mM tris, 8g/L NaCl, 0.2g.L KCl, pH7.4) and transferred to a polymer tubing (Thermo Scientific, Rockford, IL, product No. 68700, 8,000 MWCO) and dialyzed in TBS overnight. The fibrinogen solution left in the dialysis tube was filtered with a 5 μm filter, the concentration was determined by measuring light absorbance at 280nm with a spectrophotometer and the fibrinogen solution was diluted with TBS to a final concentration of 10mg/ml. Thrombin (Sigma-Aldrich, St. Louis, MO, product No. T4648) was diluted to 0.4 NIH units/ml with TBS and 50mM Ca^{++}. The solutions were allowed to cool in ice at 0 °C before transported to the magnet [155].

Fibrin gels were prepared and divided into a "control" set and an "aligned" set. Each sample in the aligned set was polymerized (Figure 5.1) in the bore of the 11.7 T Varian INOVA (Varian, Inc.; Palo Alto, CA) small animal MR imaging system so that the fibrins in the gel will be aligned with the magnetic field to generate anisotropy. Each sample in the control set was formed outside magnetic field so that the fibrin network of the gel is expected to have random orientation, and isotropic mechanical properties.

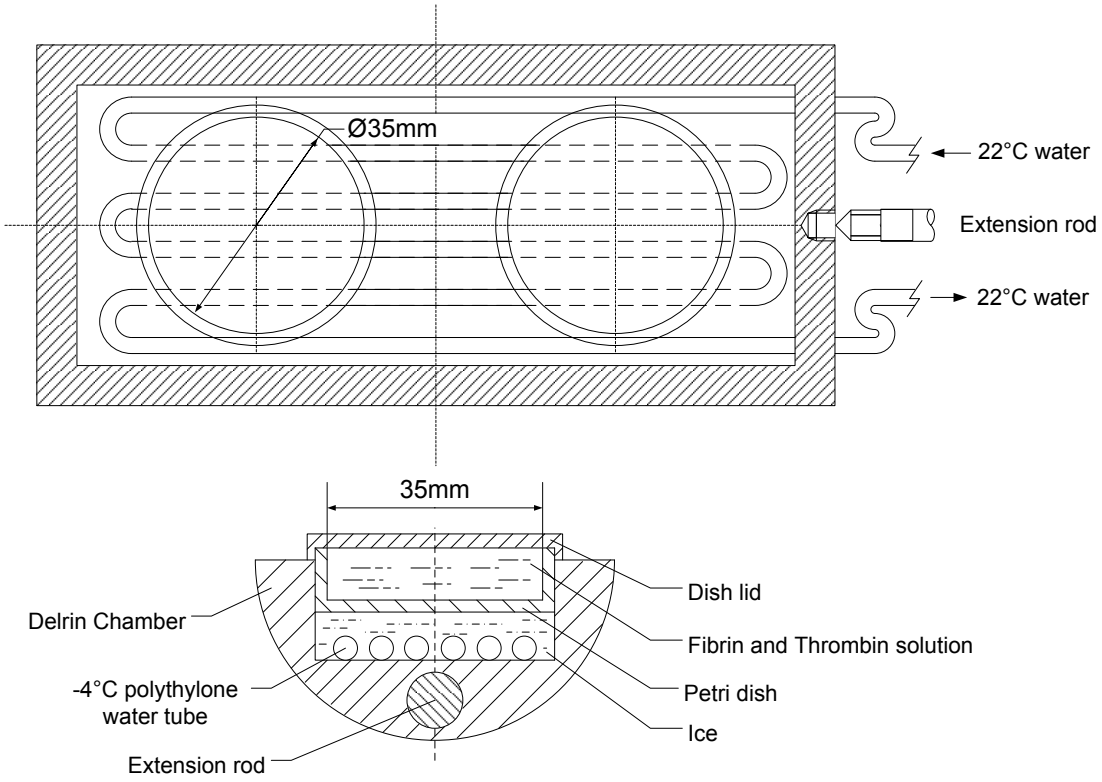

Figure 5.1 Fibrin gel polymerization setup (a) top view (b) side view of temperature chamber with two 35 mm petri dishes surrounded by ice at 0 °C. Latex tubing underneath the dish acts a heat exchanger to heat the ice to 220°C after 30 minutes of fibrin gel polymerization. An extension rod is attached to the chamber to guide it into the 12 T magnetic bore. Flattened surfaces at the two ends of the cylindrical rod allowed for placement of levels. The extension rod could be screwed in and out of the chamber based on flatness of the chamber with respect to the magnet floor as indicated by the level.

5.3 Dynamic Shear Testing

Circular samples were cut using an 11.6 mm inner diameter circular punch from the first 35 mm dish with direction of alignment marked on each aligned fibrin gel sample. The complex shear modulus over 20 – 200 Hz oscillatory frequency range was measured using a dynamic shear testing (DST) device [100, 156]. Two horizontal force transducers (PCB Piezotronics, Depew, NY) rigidly connected to the upper shear plate (Figure 5.2) give a measurement of shear force F_s. The sample area A was estimated from its measured weight m and sample thickness h by $A = m/\rho gh$, with an estimated $\rho = 1000$ kg/m^3. Each sample was weighted before and after the test. The sample

thickness was measured by determination a good contact between the tissue sample and the upper shear plate.

A consistent identification of the contact point was adopted by first calibrating a zero gap between the upper shear plate and the lower shear plate. Then, after lowering the upper shear plate towards the tissue sample placed on the lower shear plate, a contact position was determined by observing the 90-degree phase difference between the left and the right force transducer. The height micrometer (The L. S. Starrett Company) reading was recorded and tissue's sample thickness could be calculated by subtracting the reading from the zero-gap reading.

DST data were acquired with the gel compressed by 5% of its thickness. The average shear stress τ is $\tau = F_s/A$, and the nominal shear strain is $\gamma = \frac{u_x}{h} = \frac{U_x\, cos(\omega t)}{h}$ (Figure 5.3a). The shear vibration of the flexure was produced by a voice coil. Horizontal displacement of the flexure, u_x, was measured by a capacitance probe with its amplitude U_x about 0.03 mm. DST sweeping frequency ω ranges from 20 to 200Hz. All the data were acquired by the SigLab data acquisition system (Spectral Dynamics, Inc.). Complex shear modulus can be calculated based on τ and γ:

$$\mu^*(\omega) = \frac{\tau(\omega)}{\gamma(\omega)} = \frac{F_s(\omega)/A}{u_x(\omega)/h} = \mu'(\omega) + i\mu''(\omega) \qquad (2.101)$$

where μ' is storage modulus and μ'' is loss modulus. We average the shear modulus between 20 and 40 Hz because a wave length between that frequency range is at least above 6 times longer than the thickness of the sample, thus preventing inertial effect [156].

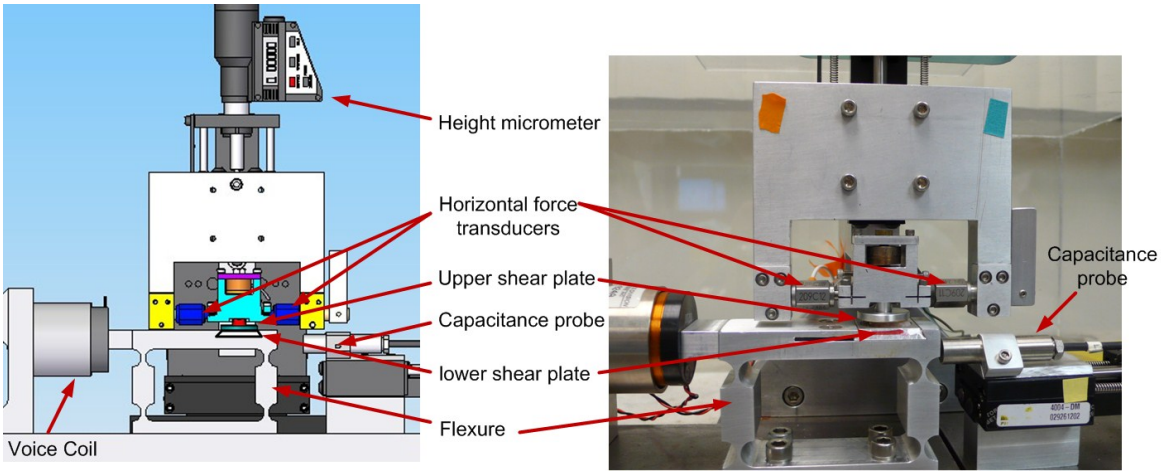

Figure 5.2 (a) CAD drawing of DST device setup. (b) Actual DST device in experiment. The height micrometer measures the thickness and the compression of the sample. Two horizontal force transducers measure the shear force F_s, which produced by voice coil connected to flexure. The detachable lower shear plate can be rotated 90 degrees.

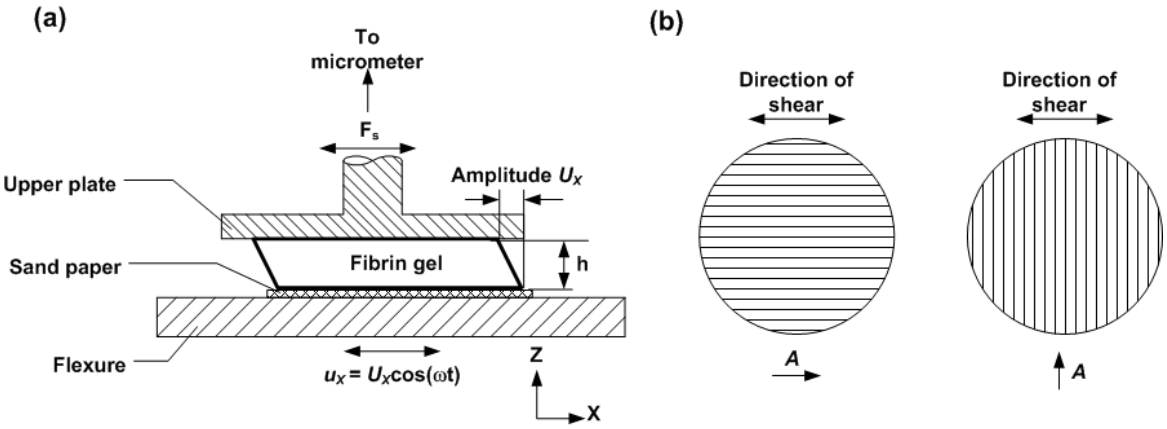

Figure 5.3 (a) Schematic diagram of dynamic shear testing (DST). The sample is deformed in simple shear by harmonic displacement of the base, while the force on the stationary upper surface is measured. (b) Fibrin gel orientation for DST. The vertical and horizontal lines indicate the dominant fiber directions of the aligned gel. When the imposed displacement is parallel to the dominant fiber axis, shear is imposed in a plane normal to the plane of isotropy. When displacement is perpendicular to the dominant fiber axis, the plane of isotropy undergoes shear deformation.

Aligned fibrin gel samples were placed on the tester with the fiber direction either parallel ($\boldsymbol{A} = \boldsymbol{e}_X$) or perpendicular ($\boldsymbol{A} = \boldsymbol{e}_Y$) to the direction of flexure oscillations (Figure 5.3b). Control gels were also tested in two orientations by rotating the sample ninety degrees after the first test. The gel was then rotated 90° about the $\boldsymbol{e}_Z$ axis and another set of data were acquired in the new orientation. The lower shear plate (Figure 5.2) was detachable for an easy rotation of the samples. Both lower and upper plates were attached with sand paper in order to prevent the samples from slipping. The sample was weighed again at the conclusion of the test to measure fluid loss during testing. A total of 13 aligned gels and 5 control gel samples were tested in two configurations (Figure 5.3b).

5.4 Asymmetric indentation

(Contribution of R. Namani)

Each fibrin gel sample was cut with a 17.5 mm diameter punch from the second 35 mm dish, weighed and placed at the bottom of a glass Petri dish. An asymmetric rectangular stainless steel indenter tip with dimensions 19.1 mm by 1.6 mm was used to indent the gel. The bottom edges of the indenter were rounded with a 0.3 mm radius. The top of the indenter tip assembly was connected to a load cell (Honeywell Sensotec, Model 31, 150g), which was connected in turn to an actuator (Model M-227.25, Mercury DC-Motor Controller, Polytech PI, MA) mounted on a stainless steel frame. The absolute movement of the actuator tip was recorded with a non-contact proximity probe (Model 10001-5MM, Metrix Instrument, TX). The thickness of the gel sample was measured separately. Voltage signals from the load cell and proximity probe were sampled at 1000 Hz using an analog-to-digital data acquisition card (Model USB-9162, National Instruments). The system actuator was controlled by custom written software (Matlab v2009, The Mathworks, Natick, MA).

Gel surface contact was measured by moving the indenter tip downwards in approximately 14 μm increments until the force change between successive increments was at least 0.2 mN. Subsequently, the gel was submerged in phosphate-buffered saline

(PBS) and allowed to equilibrate for 10 min. The actuator was moved approximately 10 µm further downwards and the force recorded. This was considered the nominal contact point of the sample surface in water and the gap between the indenter and bottom of the dish was defined as the gel thickness. The indentation protocol was a three step displacement controlled stress relaxation test (Figure 5.5c). Each displacement step (0.2 mm) was completed in 0.33 s. After each step, the indenter was held stationary for 240 s to allow the sample to relax. The actuator was then retracted and the gel was rotated approximately 90° with respect to the long axis of the asymmetric tip. The tip was then moved down to its previous contact position, and the multi-step indentation test was repeated. The sample was weighed at the end of the test.

Analysis was performed as follows: (a) Displacement and force signals were measured relative to the first recorded values and converted to µm and mN respectively. (b) Each loading and relaxation step was identified and a linear fit to the force-displacement curve of each loading step in the indentation test was used to estimate the indentation stiffness. The indentation stiffness from the second displacement step was used for parameter estimation. In some cases force did not increase until the second displacement step, indicating lack of contact. In these cases the stiffness from the third displacement step was used for parameter estimation.

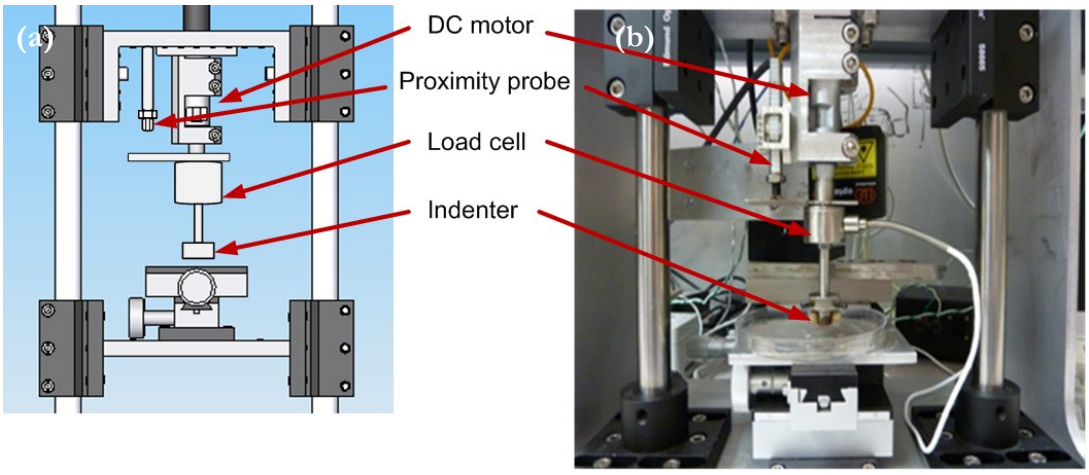

Figure 5.4 (a) CAD drawing showing indentation test device setup. (b) Actual indentation device in experiment. Indentation was actuated by DC motor which is connected to indenter. The proximity probe measures the displacement of the indenter and the load cell measures the indentation force.

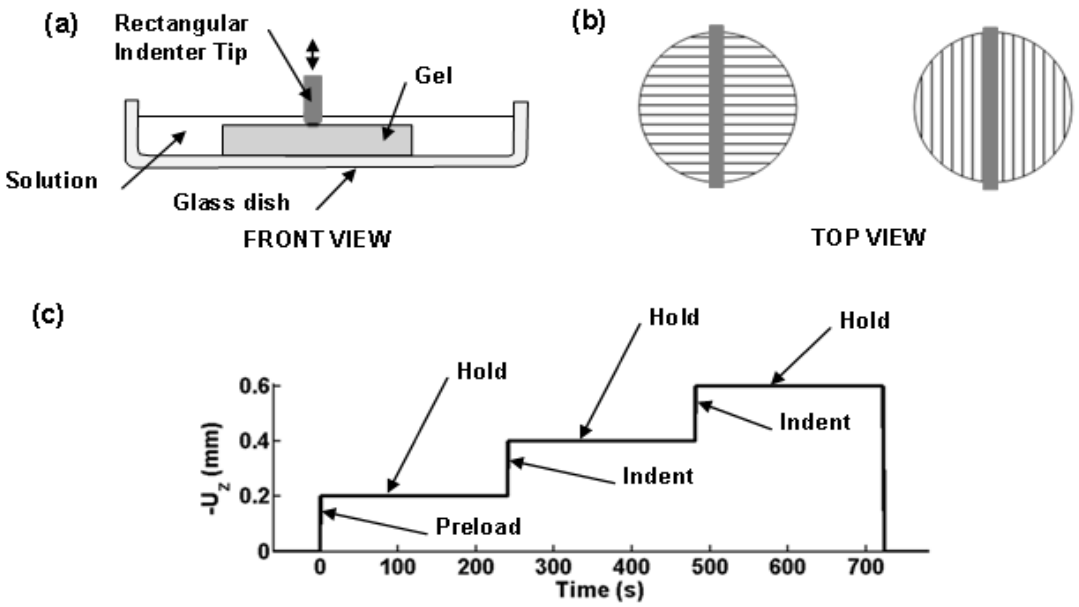

Figure 5.5 Experiment setup for asymmetric indentation of aligned fibrin gels. (a) Schematic diagram of disk-shaped gel sample (dia. 18 mm; thickness 3.0 mm) and an indenter with a rounded rectangular tip of length 19.1 mm and width 1.0 mm to 1.6 mm. The gel is submerged in a PBS solution and rests on the bottom of a glass dish. (b): Top view of indentation with fibers aligned perpendicular or parallel to the long axis of the indenter. Lines indicate the direction of magnetic alignment. (c) The indentation protocol consisting of a series of imposed displacements during which force and displacement are measured. A preload and hold (force-relaxation) step is followed by the actual indentation step which was used for data analysis. A third displacement step is performed to observe the relaxation behavior of the fibrin gel.

5.5 Results

5.5.1 Dynamic Shear Testing

The complex shear modulus, $\mu^*(\omega)$ of the fibrin gels was calculated using Eq. (4.1) for samples pre-compressed by 5% (this pre-strain satisfies small-strain conditions, but provides consistent contact and traction). For aligned gels, the storage and loss components of the shear modulus, μ' measured with fibers parallel to the excitation direction for aligned gels is denoted by $\mu_1{}'$ and $\mu_1{}''$ and the shear modulus components measured with fibers perpendicular to the excitation direction are denoted by $\mu_2{}'$ and $\mu_2{}''$. For control gels, the shear modulus components for the first test are denoted by $\mu_A{}'$ and $\mu_A{}''$, and for the components for the second test by $\mu_B{}'$ and $\mu_B{}''$.

The components of $\mu^*(\omega)$ are shown as a function of frequency f from 20 Hz to 40 Hz for a representative control and aligned gels (Figure 5.6a, b). The values of μ' and μ'' averaged over the frequency range from 20 to 40 Hz were used to characterize each fibrin gel sample (Figure 5.6c, d). The order of the tests for aligned gels was varied as described below. Differences between $\mu_1{}'$ and $\mu_2{}'$ and between $\mu_1{}''$ and $\mu_2{}''$ are statistically significant for aligned gels ($p < 0.001$, paired student's t-test), but differences between $\mu_A{}'$ and $\mu_B{}'$ and between $\mu_A{}''$ and $\mu_B{}''$ (control gels) were not. It is clear that elastic and viscous properties of fibrin gel are direction-dependent in shear for aligned gels but not for control gels. For both types of gels, the elastic component μ' is the dominant term in $\mu^*(\omega)$ and is approximately 4 to 5 times greater than the viscous component μ''.

To account for any effect of testing order on the DST results, aligned gels were divided into groups where the shear plane was parallel to the fiber direction (n = 7) or perpendicular to the fiber direction (n = 6) for the first of the two tests. The ratio $\mu_1{}'/\mu_2{}'$ was calculated for each gel. There were no significant differences between the ratios computed for the gels in the two groups.

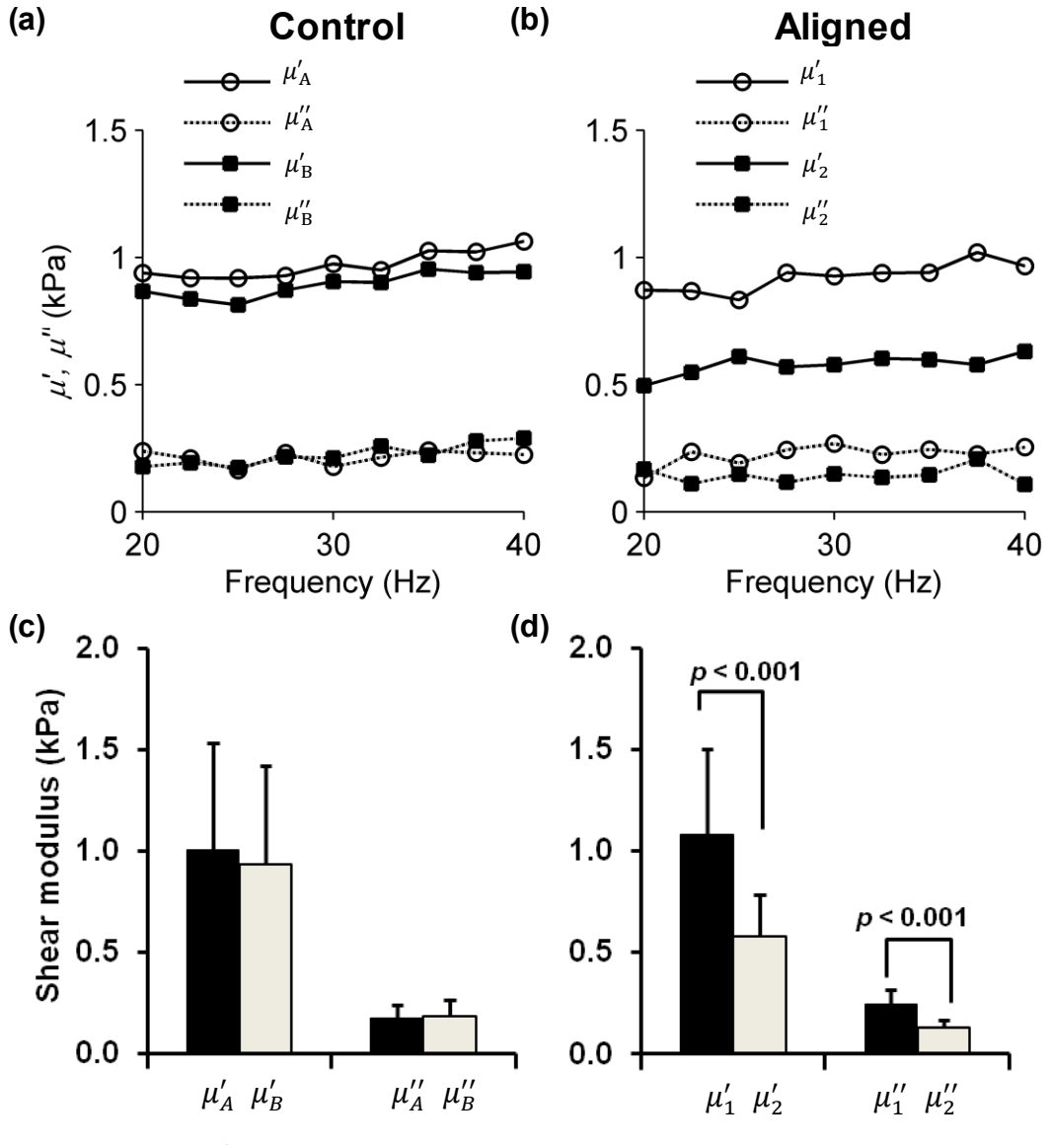

Figure 5.6 Storage (elastic) and loss (viscous) components of the complex shear modulus $\mu^* = \mu' + i\mu''$ measured using DST. for (a) a representative control gel tested in one orientation (μ_A) and then rotated about the vertical axis by 90° (μ_B) (b) a representative aligned gel tested with shear loading applied in a plane parallel to the dominant fiber axis (μ_1), or in a plane normal to the dominant fiber axis (μ_2). Data are shown over the frequency range of 20-40 Hz. Samples were tested at 0%, and 5% pre-compression; data is shown only for 5% pre-compression. Comparison of the components of the complex shear modulus of (c) control gels (n = 5) and (d) aligned gels (n = 13) samples, estimated by DST over the range of 20 – 40 Hz. Differences between storage moduli (μ'_1 and μ'_2) and between loss moduli (μ''_1 and μ''_2) for the aligned gels were statistically significant (p values as shown; Student's t-test). Error bars show one standard deviation.

5.5.2 Asymmetric Indentation

(Contribution of R. Namani)

Force-displacement curves for representative control and aligned fibrin gels are shown in Figure 5.7a and Figure 5.7b for the two indenter orientations. Force-time curves during the hold period show the stress-relaxation response of the gels (Figure 5.7c, d). In the control gel, the indentation loading response is independent of tip orientation, but in the aligned gel the forces are larger when indenting with the fibers perpendicular to the indenter. The force relaxation curves for the two tests of the control gel are similar, while the force relaxation curves of the aligned gels differ initially but eventually reach similar, small force values. The control gel appears to have a faster relaxation response between 0 s and 10 s compared to the aligned gel.

The loading portion of the force-displacement curves selected for each of the two orientations was fit with a straight line to obtain the stiffness values $k_{\parallel}^{exp}$ and $k_{\perp}^{exp}$. The R^2 value was greater than 0.9 for all the linear fits. The stiffness when indenting with fibers perpendicular to the indenter, $k_{\perp}^{exp}$, was greater than the perpendicular stiffness $k_{\parallel}^{exp}$ in all indentation tests of aligned gels. The values of $k_{\parallel}^{exp}$ and $k_{\perp}^{exp}$ were significantly different (paired student t-test, p = 0.013, n = 8) for the aligned gels (Figure 5.8a). For control gels, the mean value of the indentation stiffness measured in the second test was 7% lower than in the first test, and the decrease was significant (paired student t-test, $p = 0.04$, $n = 6$). The stiffness ratio $k_{\perp}^{exp}/k_{\parallel}^{exp}$ was significantly greater for aligned gels than control gels, but differences in the normalized equilibrium stiffness ratio in aligned gels and control gels in the two directions were not significant (Figure 5.8b).

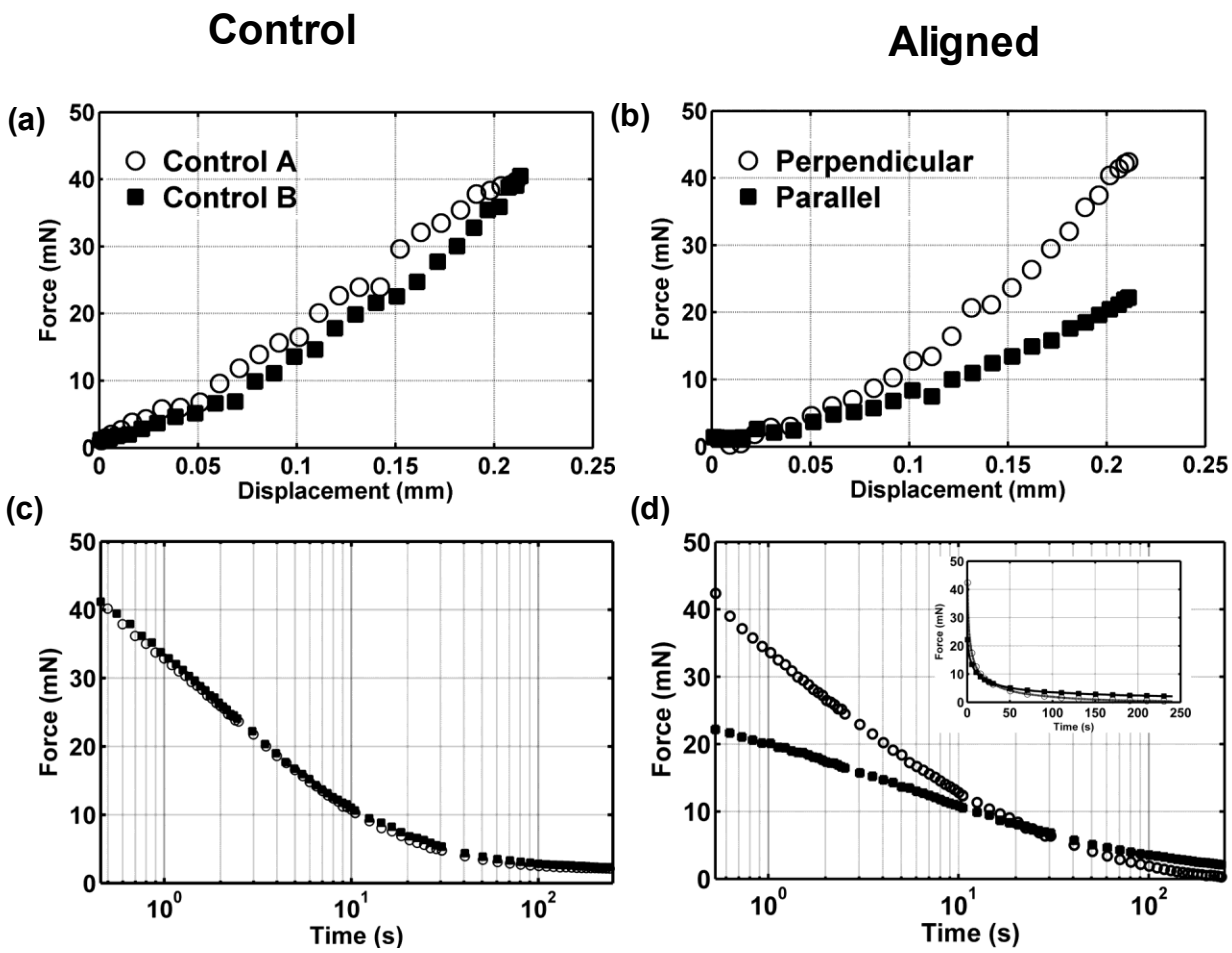

Figure 5.7 (a, b) Force-displacement measurements during indentation of (a) control (non-aligned) fibrin gels (open circles, first test; closed squares, second test) and (b) aligned fibrin gels. (open circles, indenter perpendicular to dominant fiber direction; closed squares, indenter aligned with dominant fiber direction). The indentation loading ramp duration was 0.33 s. (c, d) Force relaxation for 240 seconds after indentation of control fibrin gels and aligned fibrin gels. Relaxation time is plotted on a logarithmic scale. Both control and aligned fibrin gels lose more than 90% of their peak indentation force after 240 seconds. Inset in panel (d) shows force relaxation for aligned gels on a linear time scale.

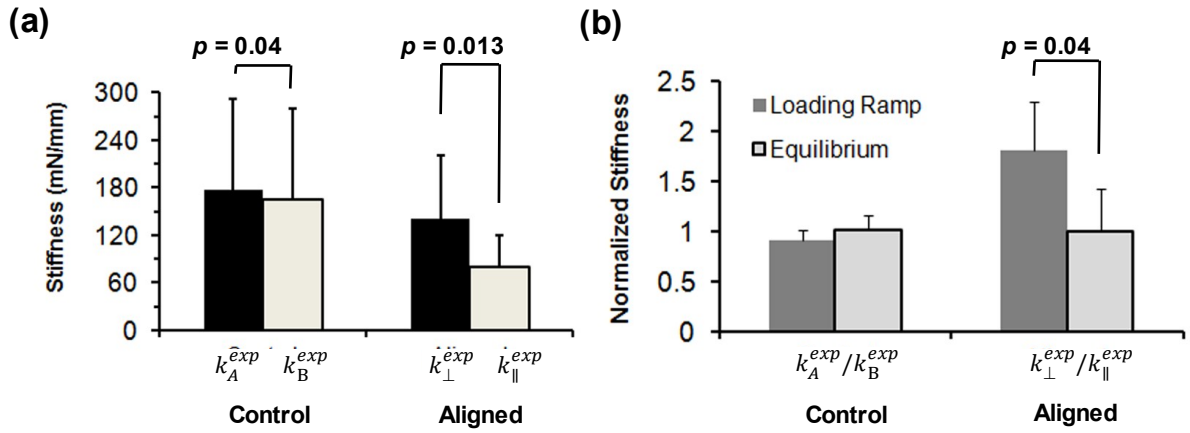

Figure 5.8 (a) The stiffness of fibrin gel samples is the slope of the indentation force-displacement loading curve (Fig. 6a, 6b). The perpendicular stiffness, $k_\perp^{exp}$, and the parallel stiffness, $k_\parallel^{exp}$, were significantly different for the aligned gels (n = 8, paired Student's t-test, p = 0.013). The indentation stiffness of control gels was slightly but significantly higher for the first test, k_A^{exp}, than the second test, k_B^{exp} (n = 6, paired Student's t-test, p = 0.04). (b) Normalized stiffness during the loading ramp and at equilibrium (after relaxation) in aligned and control gels. The normalized stiffness during loading was significantly different from the normalized stiffness at equilibrium for the aligned gels (n = 8, paired Student's t-test, p = 0.04), but not for the control gels.

5.6 Discussion

A combined shear-indentation test protocol was developed to measure mechanical properties of transversely isotropic soft materials. The procedure was demonstrated on soft anisotropic fibrin gels polymerized at a high magnetic field strength. Dynamic shear tests in the frequency range 20 – 40 Hz showed significant differences in the storage and loss components of μ^*. The values of μ' and μ'' differed significantly with fiber orientation in aligned fibrin gels but not in the control gels. The frequency range from 20 - 40 Hz was chosen to obtain average estimates of μ' and μ'' (Figure 5.6a, b), as the values were relatively constant in this frequency range. The amplitude of shear strain (<1%) is well within the small-deformation regime. For fibrin gels aligned in a strong magnetic field, the ratio of the shear storage moduli μ_1'/μ_2' measured by DST was 1.9 ± 0.3, which is consistent with the ratio μ_1'/μ_2'=3.2 ± 1.3 estimated by MRE at 400 Hz in our previous study [155]. Details of the gel preparation method and alignment protocols differ slightly between the two studies, which may explain quantitative differences between the ratios.

A multi-step indentation protocol (Figure 5.5c) was chosen to identify the equilibrium and instantaneous elastic response of the fibrin gel. The total indentation depth, which was ~20% of the sample thickness, was chosen based on the load cell resolution. The primary focus was to characterize elastic anisotropy, so only the indentation (loading) portion of the data was analyzed in detail. The loading curves in the asymmetric indentation test (Figure 5.7a, b) were obtained at the fastest possible loading rate (~0.5 mm/s) for this instrument, and the indentation time was much less than the relaxation time constant, so we assume that the loading curve was dominated by the elastic response of the fibrin network. During the hold period of 240 s, the indenter force decreased to less than 10% of the maximum forces measured during indentation. Since the equilibrium (long-term) values of indentation force were on the order of the load cell resolution, definite conclusions cannot be drawn about the apparent lack of anisotropy in the equilibrium elastic response.

Asymmetric indentation tests have been proposed previously [151], and numerical simulations have supported their utility to extract anisotropic properties of tissues. In the current work we demonstrate the feasibility of this approach in aligned fibrin gel, a structurally anisotropic soft material.

In control gels, the average elastic shear modulus obtained by indentation is higher compared to DST. This may be attributed to the larger strains in indentation (> 10%) at the end of the second indentation ramp compared to the maximum shear strains (<1%) in DST. A similar trend was seen in aligned gels. We also observed relatively large batch-to-batch differences in fibrin properties, which were reflected in range of values obtained for the material parameters from DST and indentation. Nonetheless, consistent trends in the DST and indentation data established that fibrin gels are mechanically anisotropic, with stiffer properties in the direction of primary fiber alignment.

Although a linear elastic constitutive model will not fully characterize the viscoelastic or large-strain behavior of soft materials like fibrin or brain tissue, this study shows that in

fibrin, the strain energy function should include both a term due to fiber stretch (associated with the invariant I_4) and a term due to shear in planes normal to the plane of isotropy (associated with the invariant I_5). While the linear material model itself may not apply to larger deformations, the strain energy function ψ of a more general, hyperelastic material model must depend on both I_4 and I_5 in order to reduce to the appropriate form in the limit of small strains. Thus linear models and the associated experiments presented here guide the formulation of appropriate nonlinear constitutive laws.

This approach may be used to improve our understanding of the biomechanics of traumatic brain injury. Axonal injuries induced by head impact and acceleration vary by region in the brain and also the direction of external loading [156]. Although axonal injury induced by head acceleration likely occurs at strain levels above the infinitesimal strains accessible by the current implementation of our method, accurate data on the spatially-varying, anisotropic mechanical properties of white and gray matter remain illuminating, especially when combined with numerical analysis. Such data will be useful in understanding the susceptibility of specific tissue regions to the amplified stresses experienced during trauma.

Chapter 6

Characterization of Mechanical Anisotropy of White Matter

White matter in the brain is structurally anisotropic, consisting of bundles of myelin-sheathed axonal fibers. White matter is believed to be mechanically anisotropic as well. Specifically, transverse isotropy is expected locally, with the plane of isotropy normal to the local fiber axis. In this chapter I use first principles to identify transversely isotropic hyperelastic material models (developed in Chapter 2) suitable for white matter. Based on the experimental methods developed in Chapter 5, the necessary form of such models is determined. Suitable models involve strain energy density functions with specific terms added to model the effects of stiff fibers. We show that models with added terms based only upon the pseudo-invariant I_4, which is the square of the stretch ratio in the fiber direction, do not predict anisotropy in shear with respect to the fiber axis. However, modeling of anisotropy in both tension and shear is possible using terms including both I_4 and an additional pseudo-invariant I_5 that contains the contributions of shear strain in planes parallel to the fiber axis. We show experimentally, using a combination of shear and asymmetric indentation tests, that white matter does exhibit anisotropy in shear due to fiber-matrix interactions as well as anisotropy due to fiber stretch. Indentation tests were interpreted through inverse fitting of finite element models in the limit of small strains. Results highlight that: (1) hyperelastic models of white matter should include contributions of both the I_4 and I_5 strain pseudo-invariants; and (2) behavior in the small strain regime can usefully guide the choice and initial parameterization of material models for large deformations.

The material presented in this chapter is submitted for publication in the Journal of Biomechanics and Mechanobiology (Feng, Okamoto, Namani, Genin, and Bayly 2012). Feng developed the mechanics model, performed the DST and indentation experiments, analyzed the data, and wrote the manuscript. Okamoto did part of DST experiment, and ran the FEA simulations. Namani developed the methods for indentation experiments. Feng, Genin, and Bayly led the study. All the authors reviewed and edited the manuscript.

6.1 Introduction

6.1.1 Background and Motivation

Traumatic brain injuries (TBI) are a common cause of death and disability in the United States [2]. In such injuries, shearing and stretching of brain parenchyma arise from deformation patterns that are spatially inhomogeneous and sensitive to the details of the external loading [54, 127, 157-158]. Predicting the macroscopic regions that will experience injurious stresses and strains during external loading is a primary goal of understanding TBI. Computer simulation methods (predominantly finite element (FE) simulations) have been proposed for prediction of injuries and development of preventive strategies [11, 13] have been applied to predict strains in neural fibers (axons) [159] which are hypothesized to underlie diffuse axonal injury (DAI). Predicted strains from simulations can be correlated with injury markers [20] using strain-based thresholds for cellular and tissue injury determined under in vitro test conditions [21-22, 159].

A number of challenges remain before predictions of FE simulations can be applied with confidence. A central role of brain/skull tethering in determining the brain's response to skull acceleration has been reported [54-55, 113-114, 127, 160-162], but these boundary conditions have only recently been incorporated into FE models [159, 163]. The relationship between mechanical strain and cell death appears to be more

complicated than can be predicted by a simple strain or strain rate criterion, and should likely incorporate effects of the brain's structure [161]. Finally, a complete and accurate picture of the mechanical properties of brain tissue is needed [164].

This latter area is the focus of this article. The effort to characterize brain material properties has been sustained for over fifty years [26-27, 32-33, 90-91, 152, 165]. This chapter adds to this substantial body of literature by identifying necessary features of transversely isotropic hyperelastic models for modeling of white matter, which is neural tissue composed mainly of axons and their myelin sheaths, and demonstrating the initial parameterization of one such material model.

6.1.2 Characterization of Mechanical Properties of White Matter Tissue

White matter tissue appears to be deformed and injured during brain trauma [8]. The mechanics of white matter are important both for predicting this injury and for detecting this injury through changes that are observable noninvasively. This has been studied by both in vivo and in vitro methods. In vivo studies of brain tissue using magnetic resonance elastography (MRE) are promising but do not yet fully address the directional dependence of tissue properties [164]. Since white matter consists predominantly of aligned axonal fibers, it is hypothesized to be mechanically anisotropic, in contrast to gray matter, which is structurally isotropic [39]. More specifically, white matter is expected to be transversely isotropic with the fiber axis normal to the plane of isotropy.

The literature largely supports this hypothesis. In one study, white matter (brainstem) was found to demonstrate an anisotropic (transversely isotropic) response to oscillatory shear deformation [36]. Subsequent studies [39, 86], confirmed that gray matter appeared isotropic and that white matter from corona radiata, corpus callosum and brainstem appeared anisotropic when subjected to shear deformation at high strains and strain rates. Hrapko and co-authors [43] suggested that the anisotropy of corona radiata

increases with the magnitude of shear deformation but decreases with increasing frequency during dynamic oscillatory shear tests. On the other hand Nicolle and co-authors [44] observed that white matter from the corona radiata appeared isotropic in shear under small strain (0.0033%) and high strain rates (0.8 s^{-1}). When uniaxial tensile tests were performed on strips of porcine corona radiata, they appeared almost 3 times stiffer when the fiber axis was aligned with the direction of stretch [45].

Transversely isotropic materials may exhibit anisotropy in both shear and tension with respect to the fiber axis [166]. To our knowledge, prior experimental studies of white matter [39, 43, 45] have focused on either shear or tensile anisotropy, but not both. Measurement of anisotropy in both shear and classical tensile tests requires separate samples, as gripping brain tissue for tensile tests damages the tissue. To overcome this measurement problem, dynamic shear tests can be combined with subsequent asymmetric indentation tests to measure the anisotropy of brain tissue. This protocol involves both fiber-matrix shear and fiber stretch in the same sample [100]. These tests require only simple fixtures to hold the sample, are non-destructive at small strains, and in theory can be used to estimate all the parameters of an incompressible, transversely isotropic, linear elastic model of brain tissue.

Although linear elasticity is not sufficient to describe the mechanical properties of white matter under large deformations, all hyperelastic models for white matter must match the predictions of linear elasticity in the limit of small strains. Linear elasticity is therefore valuable for guiding the selection of the form of a more general model.

A central insight that emerges from the current work is the set of strain invariants upon which these more general models can be based. Structurally-based models [87] and transversely isotropic hyperelastic models [12, 45, 86] of white matter have been proposed. In published hyperelastic models, a standard fiber reinforcement formulation [98, 167] has been used. In standard fiber reinforcement models, tissue anisotropy observed during tensile or shear tests is related to an additive term in the strain energy due to fiber reinforcement, captured by the pseudo-invariant I_4 of the right Cauchy-Green strain tensor. Holzapfel and Ogden (2009)[149] have discussed the general

requirements for full characterization of incompressible hyperelastic materials; they advocate use of a material model in which strain energy depends only on I_1 and I_4, unless evidence supports a more complicated constitutive law. However, a material model that incorporates only I_4 to model fiber reinforcement does not predict anisotropy in shear in the small strain regime [168]. In contrast to this theoretical picture, anisotropy has been observed in shear tests of white matter [39] and brain stem [36]. For a hyperelastic material to exhibit anisotropy in shear under small deformations, the strain energy function must depend on the pseudo-invariant I_5 [166]. We describe these pseudo-invariants and their roles in the material response in more detail below and show that both I_4 and I_5 are essential to predicting the mechanics of white matter.

6.1.3 Study overview

The goal of this chapter is to determine what features of constitutive models are needed to capture the mechanical anisotropy of white matter. We note that the response of a general hyperelastic material during small deformations depends on the form of its strain energy function [95]. To demonstrate this idea, a candidate transversely isotropic, hyperelastic model based on a specific strain energy density function described in chapter 2 is applied to describe the behavior of white matter; the model behavior in the infinitesimal strain limit is compared to relatively simple experiments that identify the specific anisotropic contributions of fiber stretch and fiber-matrix interaction. We tested samples of white matter (corpus callosum) and gray matter (cortex) from lamb brains, using a combination of dynamic shear testing (DST) [156] and asymmetric indentation tests [100]. White matter appeared anisotropic in both shear and indentation, while gray matter exhibited isotropic behavior. These results, while obtained in the small-strain regime, imply that for an accurate hyperelastic model of white matter the strain energy function should depend on both I_4 and I_5. We find that models written in terms of an isochoric pseudo-invariant $\overline{I_5^*}$ that contains no contribution from fiber stretch adopt particularly convenient forms. We use one such model as an example to demonstrate the form of the strain energy density function required for consistency with our experimental data.

6.2 Methods

White matter is a fibrous tissue with a clearly defined dominant fiber direction (left-right in the corpus callosum, which connects the brain's hemisphere). Experimental data is needed to determine the form and parameters of any material model. In chapter 2, it is shown that the simplest transversely isotropic, incompressible material model for characterizing white matter involves three independent parameters, μ, ζ and ϕ (Eq. (2.77)). The fitting of the candidate model to white matter involves estimating these three parameters from a combination of (1) simple shear with displacement either parallel or perpendicular to the fiber axis and (2) indentation with a tip of rectangular cross-section, in which the long axis of the tip is aligned either parallel or perpendicular to the fiber axis, with both tests performed on the same sample [100].

6.2.1 Sample Preparation

Lamb heads (8 to 10 months of age) were obtained from a local slaughter house (Star Packing Co., Inc.. St. Louis, MO) one to two hours post-mortem. The top of the skull was removed by cutting the bone on four sides. The dura mater, arachnoid and pia matter were carefully removed with a fine scissor. And the two lobes were separated by cutting the falx cerebri. Gray matter tissue samples were acquired from the temporal lobe (Figure 6.1(a)) close to the cerebellum. The cerebellum was separated from the two lobes by cutting the tentorium, and white matter tissue samples were harvested from the corpus callosum (Figure 6.1(b,d)), where axonal fibers can be seen running across and connecting the left and the right brain hemispheres. Brain samples were sliced using a vibrating microtome (Vibratome®, series 1000, St. Louis, MO), and test samples were punched from the cross-section to obtain predominantly gray matter (Fig. 1 (d)) or white matter (Fig. 1 (e)). Circular punched samples were ~2.8 mm thick and ~15.6 mm in diameter. All the samples were submerged in ice-cold artificial cerebrospinal fluid (CSF) [169] before testing, which was conducted within five hours post-mortem as

recommended by Garo et al. (2007) [42]. Testing was performed at room temperature (21°-23°C).

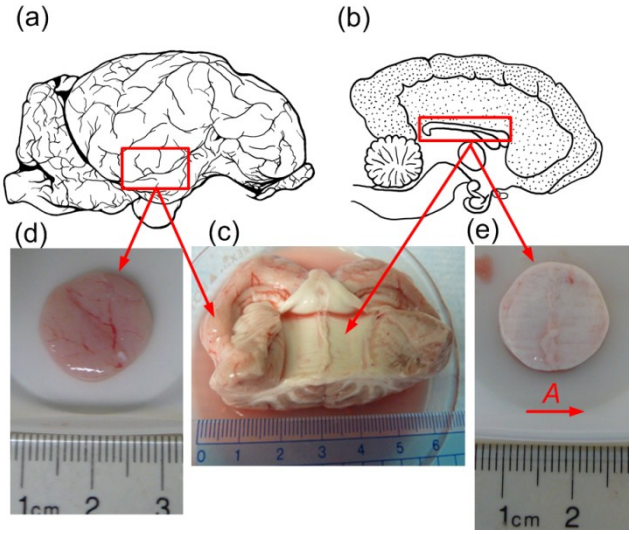

Figure 6.1 (a) Lateral sagittal view of lamb brain. The red box indicates the temporal lobe region from which gray matter samples were harvested. (b) Medial sagittal view of the lamb brain; the red box indicates the corpus callosum region from which white matter samples were harvested. (c) Portion of lamb brain showing the corresponding region where (d) gray matter sample and (e) white matter sample were dissected and punched for experiment. The ruler below the sample has 1mm scale increments. Vector *A* indicates the axonal fiber direction in the white matter sample.

6.2.2 DST and indentation

The complex shear modulus was measured using the dynamic shear testing (DST) device (Figure 5.2) [100, 156]. White matter samples were tested with the fiber direction either parallel (test 1,Figure 6.2a) or perpendicular (test 2, Figure 6.2b) to the direction of flexure oscillation. Gray matter samples were also tested in two orientations, rotating the sample by 90 degrees after the first test, with the first test marked as test A and second test as test B.

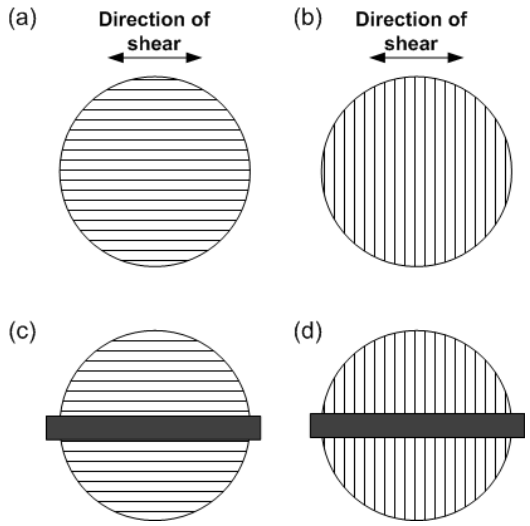

Figure 6.2. Sample configurations for mechanical testing of white matter (top view). In shear tests, each white matter sample was tested with axonal fibers (a) parallel and (b) perpendicular to the direction of imposed displacement. In indentation tests, each white matter sample was tested with axonal fibers (a) parallel and (b) perpendicular to the long side of the indenter head.

The average shear stress $\tau = F_s/A$, where A is the sample area. The nominal shear strain, γ, is $\gamma = u_x/h = (U_x\ cos(\omega t))/h$, where U_x (~0.03 mm) is the amplitude of the horizontal shear oscillation, h is the sample thickness, and $\omega = 2\pi f$, where f is the frequency (20 to 200 Hz). The complex shear modulus, μ^*, was calculated from Eq. (5.1). The indentation stiffness of each tissue sample was measured after the DST test. We used a custom-built asymmetric indentation device for measurement (Figure 6.4) and adopted a 3-step indentation protocol described in chapter 5.4. The rectangular stainless steel indenter head was 19.1 mm long × 1.6 mm wide. As with DST, we tested each sample in two configurations, rotated by 90°. White matter samples were tested with axonal fiber tracts parallel (∥, Figure 6.2c) or perpendicular (⊥, Figure 6.2d) to the longer side of the rectangular indenter head. Gray matter samples were placed on the device in an arbitrary position and then rotated by 90° after the first test, with the first and second test results noted as A and B, respectively. Each sample was indented to a depth of 5% of its thickness and then held at that position for 1 minute for tissue relaxation, which is sufficient for brain tissue to fully relax to a steady state isometric force [30, 32, 152, 170]. This process was repeated for a total of three indentation steps, reaching approximately 5%, 10%, and 15% of the sample thickness, respectively. Each

indentation step was completed within 0.5 sec with an average strain rate during indentation of 0.1 s^{-1}. The indenter was actuated by a piezo-electric actuator (Model M-227.5, Physik Instrumente, Auburn, MA) and the indentation force, F_i, was measured by a load cell (Honeywell Sensotec, Model 31, 150 g), where i=1,2,3 is the indentation step number. The vertical displacement of the indenter, d_i, was measured by a non-contact proximity probe (Model 10001-5MM, Metrix Instrument, Houston, TX). Custom written Matlab programs (The Mathworks, Natick, MA) were used for data acquisition and system control. The force-displacement curve during indentation was analyzed and the portion with approximately constant indentation velocity was fit to a line with a slope corresponding to the indentation stiffness $k = F_i/d_i$.

6.2.3 Finite Element Models

(Contributed by R.J.Okomoto)

In order to interpret the indentation test results, 3-D finite element (FE) models are developed to simulate the indentation tests using commercial software (Abaqus 6.10.1, Simulia Corp.). The FE model of indentation has been described previously [100]. Briefly, an asymmetric rigid tip indenting a transversely isotropic, linear elastic material was analyzed. The FE model geometry consisted of a layer of elastic material 3.0 mm in thickness and 15.0 mm in diameter (the tissue sample) indented with a rectangular indenter of cross-sectional area 1.6 mm × 19.0 mm. The corners of the rectangular indenter were rounded, hence the initial contact width was 1.0 mm and the initial contact area between indenter and gel was 15.0 mm^2. To reduce the number of elements required, only one quarter of the sample was modeled and symmetry boundary conditions were applied to the straight edges of the model. The quarter model contained 103,925 eight node brick elements (C3D8) and the rigid rectangular indenter was discretized into 1686 rigid elements (R3D4). Contact between the indenter and the sample was initially approximated as frictionless sliding. The displacement u_z of all nodes on the lower surface of the sample was set to zero to approximate frictionless contact between the sample and rigid substrate. All other surfaces had traction-free boundary conditions. The non-linear geometry option was used to account for large

displacements. To explore the possible role of frictional forces on our results, we included friction in the indenter-sample and sample-substrate contact conditions. The contact friction was modeled as static Coulomb friction with a friction coefficient, c_f, equal to 0.1, 0.25, 0.5, 0.75, or 1 on both contacting surfaces.

The engineering constants (Young's moduli, shear moduli, and Poisson's ratios) required by the Abaqus FE software were calculated from specified values of κ, μ, ζ and ϕ. To generate the values for different combinations of the strain energy function parameters, the ratios ϕ/μ and ζ/μ were varied while the ratio κ/μ was fixed at 200. Indentation simulations were performed with the axis of transverse isotropy oriented perpendicular to the long axis of the indentation head ($\boldsymbol{e_1} = \boldsymbol{e_X}$). To model indentation with the fibers aligned with the long axis of the indentation head, the local co-ordinate system of the material section was rotated by 90° without changing the orientation of the indenter ($\boldsymbol{e_1} = \boldsymbol{e_Y}$).A quasi-static displacement boundary condition for u_z was prescribed for the indentation head in increments of −0.01 mm and equations were solved with the Abaqus/Standard implicit solver. The maximum prescribed displacement of the indenter was $u_z = -0.15$ mm, 5% of the simulated sample thickness, which corresponded to the displacement at the end of the first experimental indentation step.

Because the indentation causes primarily local deformation in the region of the indenter, we developed a simplified model geometry consisting of a square sample (15 mm × 15 mm × 3 mm) with the same symmetry boundary conditions as the round sample geometry and a somewhat coarser mesh away from the indenter. This square model had fewer elements but yielded force-displacement estimates within 2% of the round model with a 10-fold reduction in solution time and was used for parametric studies.

6.3 Results

A total of 12 white matter samples and 9 gray matter samples were tested. For 6 of 12 white matter samples $k_{\perp}$ was measured before $k_{\parallel}$, and for the remaining six, $k_{\parallel}$ was measured before $k_{\perp}$.Typical DST experiment results for both gray and white samples are shown in Figure 6.3(a-b). The horizontal displacement of the flexure, U_x, was 0.03 mm, corresponding to a nominal shear strain of ~1%. Typical indentation experiment results for both gray and white matter samples are shown in Figure 6.4(a-b). Typical tissue relaxation results are shown in Figure 6.4(c-d). Consistent mechanical anisotropy was observed in both DST and indentation tests in corpus callosum white matter tissue.

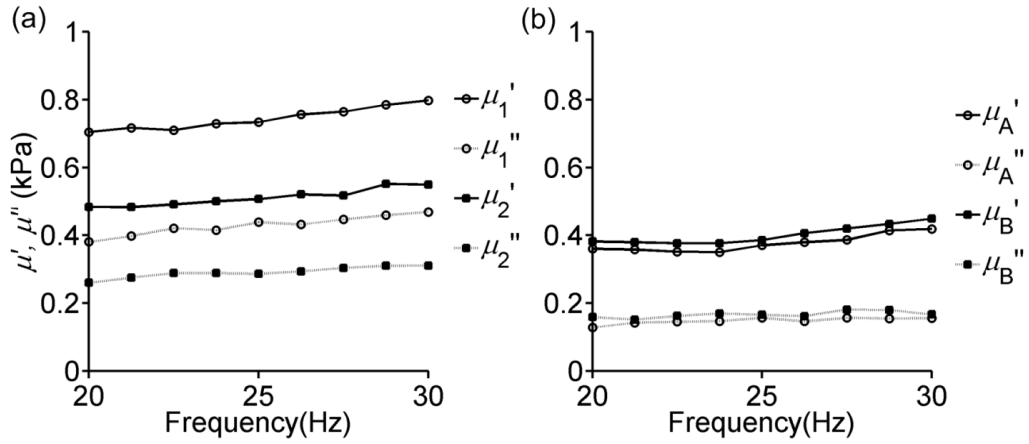

Figure 6.3. Storage and loss modulus components of the complex modulus $\boldsymbol{\mu^* = \mu' + i\mu''}$ measured using DST over frequency range 20-30Hz. (a) a representative gray matter sample tested in one orientation ($\boldsymbol{\mu_A}$) and rotated about the vertical axis by 90° ($\boldsymbol{\mu_B}$) (b) a representative white matter sample tested with shear loading applied in a plane parrallel to axonal fiber direction ($\boldsymbol{\mu_1}$), or in a plane perperdicular to the axonal fiber direction ($\boldsymbol{\mu_2}$).

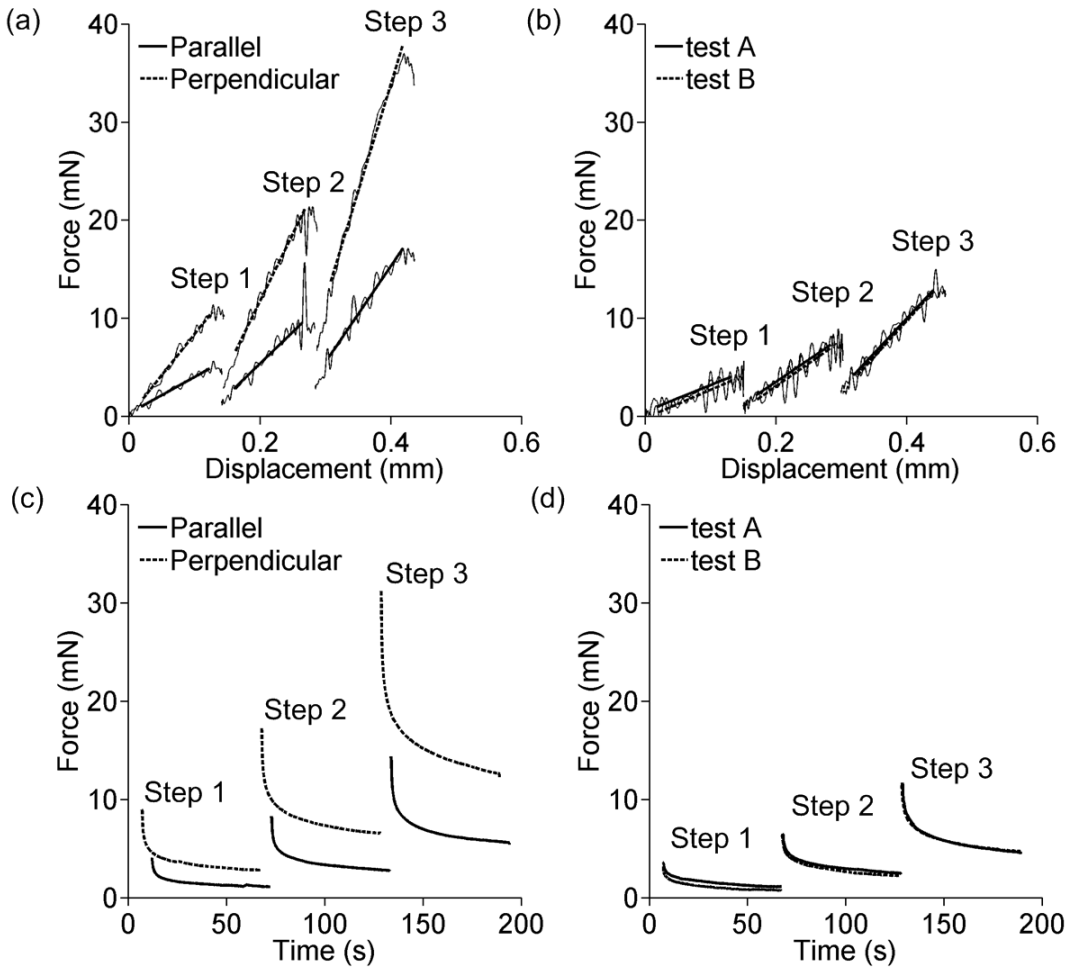

Figure 6.4. Force-displacement curve during 3-step indentation for (a) white matter sample and (b) gray matter sample. The solid and dashed lines are linear fittings when indentation head is at its constant velocity. Indentation relaxation curves during 3-step indentation for (c) white matter sample; (d) gray matter sample, the relaxation curves are filtered by a moving average filter (span over 0.5 sec) . For white matter sample test 1 is when indentation head long side is parallel to axonal fiber direction and test 2 is when indentation head long side is perpendicular to axonal fiber direction. For gray matter sample, test A is the first test and test B is the second test after rotating the sample 90 degrees along the vertical axis.

6.3.1 Results of Shear Tests

White matter samples were stiffer when tested with the fibers parallel to the direction of shear (Figure 6.2a), while no orientation dependence was detected for the shear moduli of gray matter samples. To compare shear moduli between samples, we averaged the storage and loss moduli of each sample at frequencies between 20 and 30 Hz. We calculated the estimated shear wavelengths based on the average shear moduli values

and found that the wavelengths were at least 6 times longer than the thickness of the sample, meaning that inertial effects could be neglected relative to elastic and viscoelastic effects. The average storage and loss moduli for white and gray matter samples from the DST tests are plotted in Figure 6.5a. The storage and loss moduli for white matter were significantly larger when the samples were tested with the primary axonal fiber direction parallel to the direction of shear regardless of the order in which the two orientations were tested. However, no significant difference was observed for gray matter between the two orientations tested (Figure 6.5b). The storage and loss modulus ratios (μ_1'/μ_2' and μ_1''/μ_2'') were 1.41 ± 0.26 and 1.43 ± 0.29 respectively; for gray matter samples, the storage and loss modulus ratio (μ_A'/μ_B' and μ_A''/μ_B'') were 0.96 ± 0.11 and 0.96 ± 0.15 respectively.

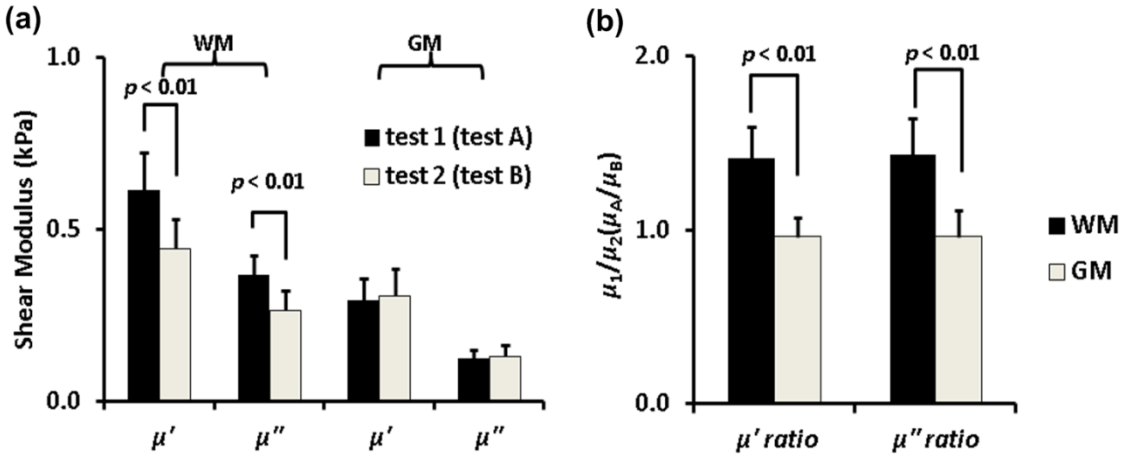

Figure 6.5. (a) Comparison of storage and loss components of the complex shear modulus of white matter (n=12 samples) and gray matter (n=9 samples). (b) Ratios of complex modulus components of white matter and gray matter, estimated by DST over frequency range of 20-30 Hz. Differences between storage moduli (μ_1' and μ_2') and between loss moduli (μ_1'' and μ_2'') for white matter samples were statistically significant (student's t-test, p<0.01). Differences between storage moduli ratios (μ_1'/μ_2' and μ_A'/μ_B') and between loss moduli ratios (μ_1''/μ_2'' and μ_A''/μ_B'') for white and gray matter samples were statistically significant (student's t-test, p<0.01).

6.3.2 Results of Indentation Tests

White matter samples appeared stiffer when indented with fibers perpendicular to the long side of the indenter head (Figure 6.2d) compared to when fibers were parallel to the long axis. In contrast, gray matter samples exhibited similar indentation stiffness in

both the first and second tests. The indentation stiffness values for all samples are summarized in Figure 6.6a, b; indentation stiffness ratios ($k_\perp/k_\parallel$ or k_A/k_B) are compared for gray and white matter in Figure 6.6c. For white matter samples, $k_\perp$ was significantly greater than $k_\parallel$, regardless of the order in which the two tests were performed. This was true for each indentation step, although the stiffness ratio $k_\perp/k_\parallel$ decreased for the second and third indentation step (2.3 $\pm$ 0.7 and 2.1 $\pm$ 0.6 respectively). For gray matter samples, there was no significant difference between k_A and k_B and the stiffness ratio k_A/k_B was not significantly different than one for any of the three steps. The relatively large standard deviations in the stiffness ratios was likely due to the uncertainty in establishing contact and local variations in thickness of individual samples. In addition, $k_\parallel$ of white matter samples for each indentation step was not significantly greater than k_A or k_B of gray matter samples for the corresponding step (Figure 6.6).

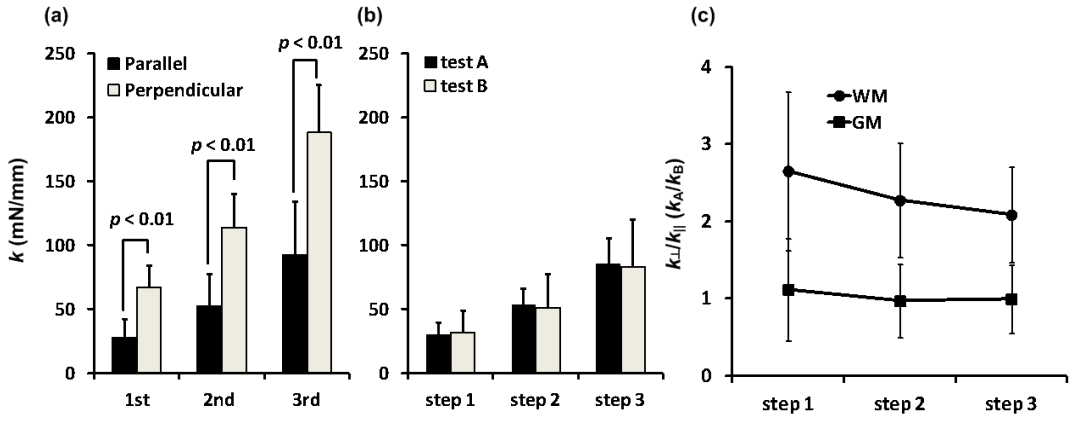

Figure 6.6. Comparison of indentation stiffness of (a) white matter (n=12 samples) and (b) gray matter (n=9 samples) for each indentation step. Indentation stiffness measured for white matter is marked as $k_\parallel$ (for axonal fiber direction parallel to the long axis of the rectangular indenter head) and $k_\perp$ (fiber axis perpendicular to the long axis of indenter). Indentation stiffness measured for gray matter is denoted as k_A and k_B, for two orientations of the sample 90° apart. The difference between indentation stiffnesses for white matter tissue ($k_\parallel$ and $k_\perp$) is significant, but the difference in indentation stiffnesses for gray matter tissue (k_A and k_B) is not significant. (c) Indentation stiffness ratio of gray and white matter. Differences of indentation ratio ($k_\perp/k_\parallel$ or k_A/k_B) for each indentation steps between white matter (WM) and gray matter (GM) samples were significantly different (student's t-test p<0.01).

6.3.3 Finite Element Model Results

(Contributed by R.J.Okamoto)

FE simulations of the indentation experiments are used to relate indentation stiffness to the three free parameters of the constitutive model. Predicted force-displacement curves were obtained in both material orientations from FE simulations by setting the ratios ϕ/μ equal to 0, 0.4 or 0.8 and ζ/μ equal to 0, 2.5, 12.5, or 25 while μ was fixed at 500 Pa and the coefficient of static Coulomb friction, c_f, between contacting surfaces was set to zero. The range for the ratio ϕ/μ was chosen to span the ranges observed in DST experiments and the range of ζ/μ was chosen to obtain maximum values of $k_\perp/k_\parallel$ $k_\perp/k_\parallel$similar to our indentation experiments. This resulted in 12 combinations of ϕ/μ and ζ/μ. Representative FE force-displacement curves are shown in Figure 6.7. The maximum magnitudes of shear strains (~ 0.2) and fiber strains (~ 0.1) occurred along the rounded edge of the indentation head; strains are typically much smaller (<0.05) in the rest of the domain.

When the sample was indented with the fiber direction perpendicular to the long side of the indentation head, the resistance of the sample to indentation increased with ζ/μ (Figure 6.7a), indicating a stronger reinforcing effect by the fibers. The resistance to indentation was relatively insensitive to the ratio ζ/μ when the sample was indented with the fiber direction parallel to the long side of the indentation head (Figure 6.7b). These trends were observed in additional studies with c_f = 0.5 (Figure 6.7c and Figure 6.7d) and with ϕ/μ = 0.1, 0.25, 0.5 or 1.0 (results not shown). Additional FE simulations with isotropic model parameters (μ = 500 Pa, $\zeta = \phi$ = 0 and c_f = 0.1, 0.25, 0.5, or 1.0) were used to estimate the effect of friction on gray matter indentation stiffness (results not shown).

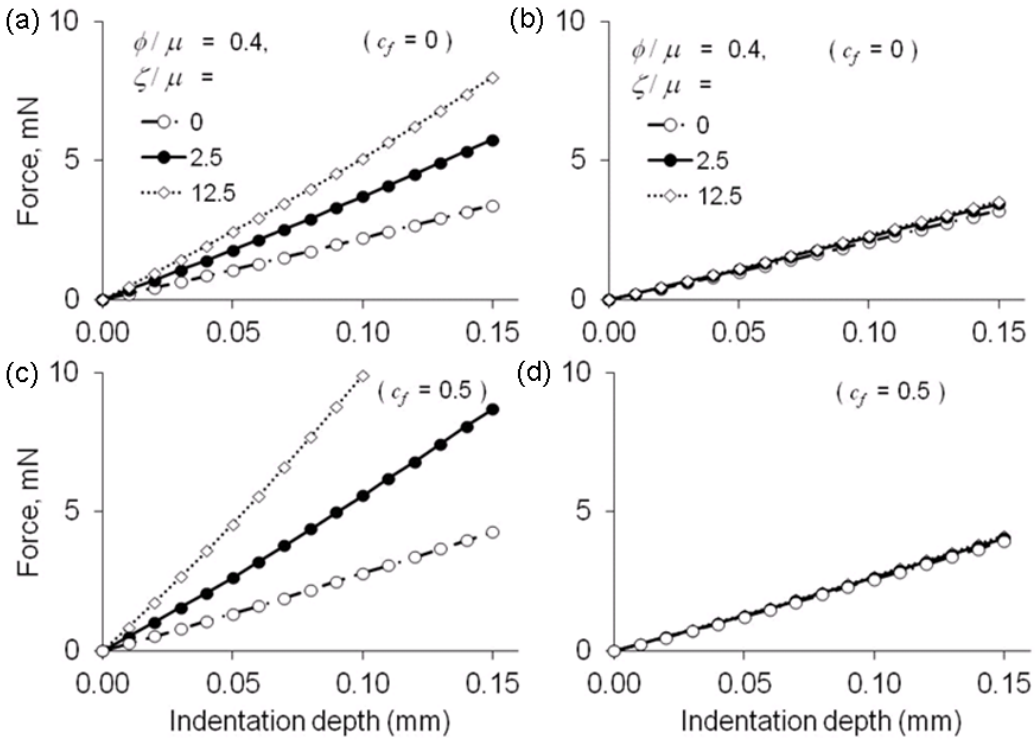

Figure 6.7 Predicted force-displacement curves from finite element simulations of samples indented with fiber direction (a) perpendicular or (b) parallel to the long side of the indenter head (frictionless). (c) and (d) Force-displacement curves as in (a) and (b) but with coefficient of friction, cf, of contacting surfaces equal to 0.5. In all panels, ϕ/μ = 0.4, κ/μ =200, and μ = 500 Pa. with ζ/μ = 0, 2.5, 12.5, or 25.

The model-predicted force-displacement curves for indentation depths of 0 to 0.15 mm were fit to a straight line and the slope was used to estimate the indentation stiffness. The stiffness values obtained with the long side of the indentation head perpendicular to and parallel to the fiber direction are denoted $k_\perp$ and $k_\parallel$ respectively. The predicted indentation stiffness ratio $k_\perp/k_\parallel$ increased with ζ/μ (Figure 6.8). The ratio $k_\perp/k_\parallel$ also increased with ϕ/μ, but the effect was minor over the range studied. Friction was important in determining $k_\perp/k_\parallel$, as shown in Figure 6.8. When the long side of the indenter head was parallel to the fiber direction, contact friction with c_f = 0.5 increased the predicted $k_\parallel$ by a factor of 1.2. However, when the long side of the indentation head was perpendicular to the fiber direction, this level of friction increased $k_\perp$ by up to a factor of 2.3. The net result was that friction increased $k_\perp/k_\parallel$.

Since we do not know precise values of c_f for either contact surface, we estimated a range of possible ζ/μ values for white matter by matching experimental values of μ_1'/μ_2' and $k_\perp/k_\parallel$ (Table 6.1) assuming that $c_f = 0.5$ or 0.1. First, we identified the value of ζ/μ that matched the experimental value of $k_\perp/k_\parallel$ for $\phi/\mu = 0.4$ and $c_f = 0.5$, resulting in a predicted value of $\zeta/\mu = 5.5$. We then estimated the value of μ by comparing the predicted value of $k_\parallel$ for the FE model (where $\mu = 500$ Pa) with the experimentally measured value for white matter, shown in Table 6.1 and scaling-which yielded an estimated $\mu = 0.51 \pm 0.27$ kPa, slightly larger than the value of μ_2 obtained from DST. For gray matter samples, we matched the experimental values of k_A to the predicted value from FE simulations with $\zeta = \phi = 0$ and $c_f = 0.5$ to obtain an estimate for $\mu = 0.58 \pm 0.17$ kPa, which is larger than the value of μ_A obtained from DST (0.29 $\pm$ 0.06 kPa). This process was repeated for $c_f = 0.1$, resulting in estimates of $\zeta/\mu = 13$, and $\mu = 0.58$ kPa for white matter, and $\mu = 0.70$ kPa for gray matter (Table 6.1).

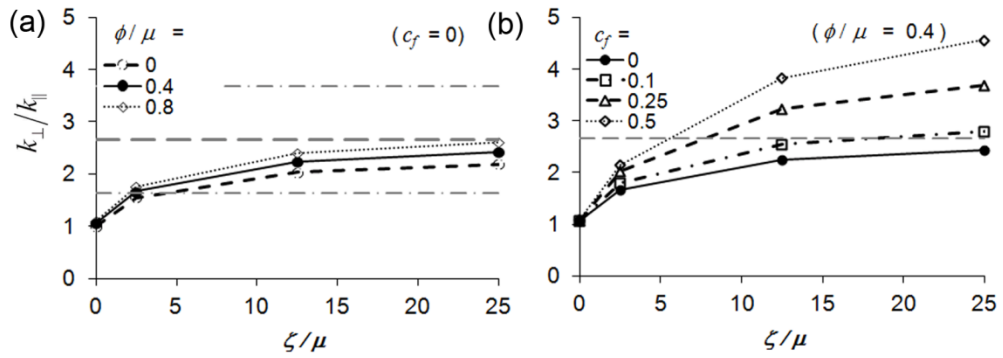

Figure 6.8 Predicted stiffness ratios ($k_\perp/k_\parallel$) from the parametric finite element model study of asymmetric indentation. (a) The increase in $k_\perp/k_\parallel$ with ζ/μ is shown for ϕ/μ =0, 0.4 or 0.8 with κ/μ = 200, μ = 500 Pa and frictionless contact (c_f = 0). The dashed horizontal lines indicate the mean experimental value of $k_\perp/k_\parallel$ for white matter samples, plus or minus one standard deviation. (b) The increase in $k_\perp/k_\parallel$ with ζ/μ is shown for c_f = 0, 0.1, 0.25 and 0.5 with ϕ/μ = 0.4 and μ = 500 Pa. The dashed horizontal line indicates the mean value of $k_\perp/k_\parallel$ for white matter samples.

Table 6.1 Summary of experimental DST and indentation test results and the associated material parameters estimated from finite element (FE) models of indentation

Gray matter	White matter			
Measured Elastic (Storage) Components of Shear Modulus				
μ'_A (kPa)	μ'_2 (kPa)	μ'_1/μ'_2		
0.29 ± 0.06	0.41 ± 0.42	1.41 ± 0.26		
Measured Indentation Stiffness				
k_A (mN/mm)	$k_\parallel$ (mN/mm)	$k_\perp/k_\parallel$		
31 ± 10	28 ± 15	2.7 ± 1.0		
Estimated Strain Engergy Function Parameters from FE Model of Indentation				
c_f	μ (kPa)	μ (kPa)	ϕ/μ	ζ/μ
0.1	0.71	0.58	0.4	13
0.5	0.58	0.51	0.4	5.5

6.4 Discussion

In this study, we investigated the requirements for general hyperelastic, transversely isotropic models of white matter in the brain. We observed that if the material exhibits anisotropy in deformations involving shear without fiber stretch , as well as during deformations involving fiber stretch, the strain energy function must depend on both of the two pseudo-invariants I_4 and I_5 . In the context of this observation, simple shear and asymmetric indentation tests were used to characterize the mechanical anisotropy of white matter. Strong mechanical anisotropy of white matter was observed in both shear and indentation tests, while gray matter tissue appeared consistently isotropic.

6.4.1 Comparison of Estimated Tissue Parameters to Values from Prior Studies

The storage moduli measured in our study ranged approximately from 420-620 Pa for white matter and were near 300 Pa for gray matter. These values are within the broad range of values reported in prior research on mammalian brain tissue [26] and consistent with previous tests of white matter tissue (corona radiata) under oscillatory shear tests at 23°C [171].

Our findings that corpus callosum white matter is mechanically anisotropic and gray matter is mechanically isotropic are consistent with most prior studies. Our observation that the sample is stiffer when shear is applied in the plane parallel to the fibers, compared to shear in the plane perpendicular to the fibers, is consistent with the observations of Prange and Margulies (2002) [39] for the corona radiata, but differs from their reported findings in the corpus callosum. Hrapko and co-authors [43] also found that white matter tissue from the corona radiata region was mechanically anisotropic, with a stiffness ratio between maximum and minimum directions of about 1.3. We note also some conflicting evidence; early studies [33] using human brain tissue appear to show that white matter tissue from the corona radiata is isotropic in shear. A recent study using rotational rheometry and DST, Nicolle [44] also concluded that porcine white matter tissue from the corona radiata does not exhibit significant anisotropy in shear.

Our measurements of shear modulus magnitude are generally consistent with those of other recent indentation studies. Indentation tests of porcine brain tissue [32] using a spherical indenter (indentation depth 0.1-0.3 mm, indenter diameter 2 mm, sample thickness ranging from 1 to 2 mm) showed that porcine gray matter has lower indentation stiffness and lower estimated average shear modulus (μ'=0.75 kPa) than white matter (μ'=1.0 kPa). Microindentation methods (indentation depth 40 μm) was used to investigate the regional mechanical properties of porcine brain tissue [152]. Those results suggest that the equilibrium (steady state) shear modulus is larger in the cortical gray matter than in white matter from the corpus callosum, but that at short

time scales, corpus callosum white matter is stiffer than cortical gray matter, consistent with our results. However, in rodents [31, 50], white matter was observed to be softer than gray matter tissue when indented. Prange and co-authors [172-173] investigated regional differences in porcine brain tissue, and concluded that the average equilibrium modulus of gray matter tissue was about 1.3 times stiffer than the modulus of white matter tissue from the corpus callosum. However, the shear strain amplitudes (2.5% - 50%) were much larger than in our tests (1%), and the equilibrium shear modulus was computed rather than the complex shear modulus.

6.4.2 Relationship of Model Parameters to Physical Measurements and Simulation

In the majority of hyperelastic, transversely isotropic models of fibrous tissue in the literature, the strain energy function is assumed to depend on the pseudo-invariant I_4 but not on I_5 [45, 86, 167]. Such material models will predict the same shear modulus for simple shear in planes parallel to the fiber axis as for shear in planes perpendicular to the fiber axis [167-168]. This is inconsistent with the anisotropy that we observed in our experimental shear tests: the shear modulus is larger when displacement is applied along the fiber axis. We showed that a simple hyperelastic model can explain the observed mechanical response of white matter, as long as it includes contributions from both I_4 and I_5 in the strain energy density function.

The example hyperelastic model we use to illustrate these points is based on a strain energy density function that depends in general on four parameters. The bulk modulus, κ, was taken to be infinite to represent the incompressibility of white matter. Estimates of the remaining three moduli could be extracted from the small strain data that we acquired. The three parameters were a shear modulus, μ, a modulus of shear anisotropy, ϕ, and a modulus of fiber stretch, ζ. Their appearance in the stress-strain relations (Eq. (2.78)) and the small strain limit of these (Eq. (2.79)) offer insight into their physical interpretations. Since a Neo-Hookean form was taken for the isotropic foundation of this model, the constants μ and κ could be fit to small strain data and

retain their usual meanings in the limit of small strain. The modulus of shear anisotropy ϕ appears in the small strain limit only as an additional shear resistance relative to the isotropic shear modulus μ. However, at larger strains, Eq. (2.78) reveals a coupling between this added shear resistance and the stress in the fiber direction. The modulus of fiber stretch, ζ, appears only in terms associated with axial stretching for both small and large strains. This effect was measureable in indentation experiments, but only for tests in which specimens were indented with the long axis of the indenter perpendicular to the fibers.

The form of the constitutive law examined in this study was a special case that could be fit to data from the small-strain regime, and thus might not be accurate for injury-level deformation of white matter. However the results should guide the development of more general, nonlinear hyperelastic models for larger deformations. Such hyperelastic models should be consistent with the linear elastic model in the limiting case of small strain. Specifically, the small strain limit of all such models must reduce to the form of Eq. (2.78) with $\mu_1 > \mu_2$, which requires that the model must depend on both I_4 and I_5.

For the combination of shear and asymmetric indentation, experimental estimates of the values of parameters that govern shear (μ and ϕ) could be determined with greater precision than the parameter ζ that describes anisotropy due to fiber stretch. This is largely due to the effects of friction on indentation force. FE model results demonstrate that the indentation stiffness ratio $k_\perp/k_\parallel$ depends on friction as well as on the ratio ζ/μ, with both affecting the amount of energy stored in material directly beneath the indentor. Prior FE simulation studies of indentation on soft biological tissues treat the contact between sample and indenter head as frictionless The current study shows that the effect of friction can be substantial in the indentation of anisotropic materials, because it affects the stiffness ratio for parallel and perpendicular indentations; indentation stiffness perpendicular to fibers increased with friction, while stiffness during parallel indentation was relatively insensitive to friction.

In asymmetric indentation experiments the ratio $k_{\perp}/k_{\parallel}$ may also be influenced by local variations in sample thickness and initial contact force, making the standard deviation of the measured stiffness ratio relatively large. When combined with the uncertainty due to frictional effects, we conclude that precise determination of ζ/μ $\frac{\zeta}{\mu}$is not possible; but the combination of the FE studies and our measurements show that white matter has a substantial fiber reinforcement effect. Using Eq. (2.82) and assuming c_f = 0.5, we can estimate the ratio E_1/E_2=6.5 for white matter from the lamb corpus callosum. This value is somewhat larger than corresponding estimates for white matter from porcine corona radiata found from uniaxial tests by Velardi et al. [45]; they obtained a fiber reinforcement parameter k = 1.7, corresponding to E_1/E_2=2.7.

6.4.3 Discussion of Viscoelastic Behavior

Although most of the discussion is focusing on the elastic response of the tissue, it is noticed that brain tissue has viscoelastic properties. To illustrate the viscoelastic properties of the brain tissue, a three element Maxwell fluid model is adopted for fitting the relaxation curve of white matter (Figure 6.9). The peak force at the end of the indentation is larger for elastic model than the viscoelastic model. But at the initial stage of indentation, elastic model fits the experimental data well.

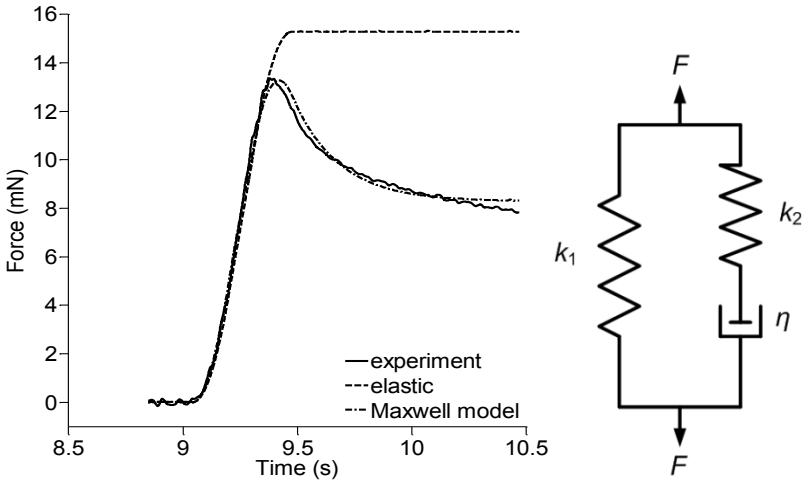

Figure 6.9 Tissue relaxation and 3-parameter Maxwell viscoelastic model.

6.4.4 Limitations and Future Work

Because this study was limited to small strains, future work should include further experimental and modeling studies focusing on large deformation in white matter. Nonlinear material properties may contribute to the increase of indentation stiffness with indentation depth (Figure 6.6). Also, although a purely elastic model was used to describe the mechanical response of brain tissue (focusing on the short-time response), brain tissue exhibits viscoelastic behavior. After rapid indentation the indentation force relaxed to about 38% of its peak value. However, the primary goal of this study was to describe the elastic component of the short-term response of white matter, which should guide the selection and parameterization of more general hyperelastic and viscoelastic models.

Experimental measurements were performed ex vivo in this study. Although all tests were conducted within 5 hours of death, material properties may differ from those in the living, intact brain. Magnetic resonance elastography (MRE) has been used to estimate the mechanical properties of soft tissues including brain, in vivo [60-61, 63-65, 128]. In MRE, shear waves are imaged by magnetic resonance techniques and the local wavelength is used to infer viscoelastic parameters. Recent studies of human brain tissue in vivo have suggested that white matter tissue is about 2.6 times stiffer in shear modulus [174] at 100 Hz. In a study involving MRE of the feline brain, white matter also appeared stiffer than gray matter at 85 Hz [131]. MRE studies of anisotropic wave propagation are possible in brain [146], but factors such as the relatively long wavelength of shear waves compared to the size of typical brain structures, and the dependence of wave speed on fiber direction, complicate the inversion problem. Direct comparison between estimates of anisotropic parameters of white matter obtained in vivo by MRE and in vitro by mechanical testing is a future goal. Using current methods, direct estimation of the shear modulus from DST is possible only up to about 30 Hz. Chapter 4 discussed the application of MRE to ferret brain in vivo. Future work could include an MRE study of lamb brain tissue in a comparable frequency range.

Chapter 7

Conclusions

This dissertation describes the dynamic response of the brain to repeated impacts, including the brain-skull interaction, and the mechanical properties of brain tissue both ex vivo and in vivo. This chapter summarizes the key results and highlights the significance of the previous chapters. The limitations of this dissertation with respect to MR imaging, modeling, and experimentation are addressed. Finally, future directions for research on TBI, brain-skull boundary conditions and tissue mechanics are presented.

7.1 Summary

7.1.1 Key Findings and Results

This section summarizes the key findings and results of each specific aim of this dissertation:

- A tagged MR imaging method was used to study the dynamic response of the brain during mild frontal impact of the human head. Rigid motions of the skull were calculated by using a rigid-body registration method. The peak linear acceleration of the skull is about 16.3 m/s^2, and the peak angular acceleration is about 143 rad/s^2 during the impact. A typical displacement of the brain relative to the skull during these impacts is about 2-3 mm. The maximum principal strain during the impact is near 5%.

- Viscoelastic properties of ferret brain tissue were measured in vivo by MRE. Harmonic excitations were applied to the skull at 400 Hz, 600 Hz, and 800 Hz. Three-dimensional (3D) displacement fields were acquired during wave propagation in the brain. Shear waves with wavelengths on the order of millimeters were clearly visible in the displacement field, in strain fields, and in the curl of displacement field (which contains no contributions from longitudinal waves). Viscoelastic parameters (storage and loss moduli) governing dynamic shear deformation were estimated in gray and white matter for these excitation frequencies. The estimated storage modulus (G') and loss modulus (G'') increased over the measured frequency ranges in both the gray matter and the white matter. In general, white matter in the ferret brain appears to be stiffer and more dissipative than gray matter, especially at lower frequencies.

- A mechanical testing procedure was developed to characterize transversely isotropic soft biological tissue. The experimental protocol was applied to test fibrin gel, in which fibrils could be aligned arbitrarily. Shear storage modulus measured by DST is 1.08 ± 0.42 kPa (mean $\pm$ std. dev.) for shear in a plane parallel to the dominant fiber direction, which was significantly larger than the shear modulus (0.58 ± 0.21 kPa) for shear in the plane of isotropy. Indentation tests also showed that the aligned fibrin gels were stiffer when indented with the long axis of the rectangular tip perpendicular to the dominant fiber direction.

- Mechanical anisotropy of white matter and mechanical isotropy of gray matter were studied by applying the DST and indentation procedures to lamb brain tissue. The storage and loss moduli ratios (ratios of shear moduli in planes parallel and perpendicular to fibers) of white matter are 1.41 ± 0.26 and 1.43 ± 0.29, respectively, indicating strong mechanical anisotropy. The storage and loss moduli ratios of gray matter are 0.96 ± 0.11 and 0.96 ± 0.15, respectively, indicating mechanical isotropy. The indentation results also showed strong mechanical anisotropy for white matter, and a mechanical isotropy for gray matter.

- The experimental results of the shear tests of both fibrin gel and lamb brain white matter indicate that the pseudo-invariant I_5, which contains the contributions to strain energy of the shear strain in planes parallel to the fiber axis, needs to be included in the strain energy function. A candidate strain energy function containing both contributions of I_4 and I_5 is presented. The parameter study by FE methods complies with experimental observations.

7.1.2 Significance

- The in vivo displacement and strain fields observed during mild frontal impact illuminate the interactions of the brain-skull interface. The data acquired provides boundary conditions between the brain and the skull, and can be used to validate computer simulations of TBI models.

- The measurements of shear wave propagation in the ferret brain can be used to both parameterize and validate FE models of brain biomechanics. The white and gray matter mechanical properties measured in vivo can also be used for a direct comparison of the ex vivo mechanical tests.

- The test protocol developed combining both DST and indentation can be used for parameter characterization of a large variety of transversely isotropic biological tissue, such as muscle, aorta, and myocardium tissue.

- The experimental results of the mechanical anisotropy of the white matter confirm the prior research findings of the white matter anisotropic properties, and can provide useful guidance for a more general hyeprelatic model construction.

- The proposed transversely isotropic hyperelastic model analyzed in the small strain regime can be a useful guide to the choice and initial parameterization of material models in the large deformation regime.

7.2 Limitations

Limitations of this dissertation can be categorized into limitations of modeling and of experimental methods. This section discusses the limitations of the spatial and temporal resolutions of the MR imaging methods used in chapter 3 and chapter 6. Differences between 2D and 3D imaging and analysis are discussed. Shortcomings of current mechanical testing methods and mechanical models are also presented.

7.2.1 MR Imaging

The spatial resolution of MRI is one of the most important limitations in both MR tagging studies and MR elastography studies. In the study of brain-skull interactions using the tagged MR method, the image resolution affects the rigid body registration results, thus also affecting the accuracy of the estimate of the rigid body motion of the skull. Although the current MR tagging pulse sequence and imaging parameters appear to give an appropriate resolution (voxel size $1.3\times1.3\times5$ mm^3, compared to human brain which is about 1.1-1.3 $\times10^3$ mm^3 [175]), the resolution still may be improved to give a more accurate estimate of the brain-skull relative motion. In the study of in vivo measurements of ferret brain properties by MRE, the image resolution will affect the displacement estimates during wave propagation, thus affecting the estimate of the shear modulus. The current resolution of the MRE imaging sequence used (voxel size $0.5\times0.5\times0.5$ mm^3) is sufficient to observe the shear wave propagating through the brain, but a finer resolution could provide more accurate elastograms for each specific region of the brain.

The temporal resolution (5.6 ms) used in the MR tagging study is also a limiting factor. In the mild frontal impact, a total of 30 image frames were acquired for analysis. Around the peak acceleration and displacement point, about 5 image frames were captured for depicting the brain-skull interaction. Better temporal resolution would help

acquire more images during the period of high deceleration after impact, thus giving a more detailed picture of brain-skull interaction.

In the MRE study, we were able to acquire 3D images for modulus analysis. However, in the tagged MR imaging study, only 2D images were acquired for studying planar motion. Although acquiring 3D tagged images using the current imaging protocol could be accomplished by multi-plane imaging sequences, it would take more impact repetition and longer time for scanning, which would not be suitable for human volunteers. If isochoric material properties are assumed, the strain component outside of the imaging plane would be less than 1% in this study. This supports the usefulness of the 2D tagged imaging method; however, although small, the out-of-plane motion should not be neglected.

7.2.2 Mechanical Test

The sample geometry is one of the most important limiting factors in the mechanical testing methods used. In both DST and indentation tests, cylindrical samples were acquired by using a circular punch. The flatness of the sample surface could affect the detection of the contact point between the DST shear plate (or indentation head) and the sample. Current preparation methods for fibrin gel provide a satisfactory flat surface of the sample, but it is a challenge to have perfectly flat samples of brain tissue because of the uneven geometry of the brain. For DST tests, the signal-to-noise ratio is related to the contact area between the sample and shear plate. Current DST samples used have a diameter of 11.6 mm for the fibrin gel, and a diameter of 15.6 mm for the brain tissue. The diameter of the fibrin gel sample is constrained by the magnetic bore size, which is used for housing the gel sample for fiber alignment. The diameter of the brain tissue sample is constrained by the brain size and the region where cylindrical samples are harvested.

In the indentation test, the contact position is determined by the attainment of a 1 mN contact force. Due to the limitations of the sample size, the uneven surface, and the

indentation contact area, the signal-to-noise ratio is limited. In the FE simulation of the indentation process, the friction between the sample and the indentation head can affect the indentation stiffness ratio.

7.2.3 Modeling

This dissertation is presented within the framework of continuum mechanics, which gives the flexibility of application to both the small and the large strain regime. In the tagged MR study, the maximum principal strain is about 5%. In the MRE study, the maximum strain is about 3%. In the DST and indentation tests of both fibrin gel and lamb brain tissue, strain results within 5% were analyzed. The material characterization studies (MRE, DST, and indentation) were all interpreted in the context of linear elasticity under the assumption of small strains. Although the current in vivo and ex vivo studies provide data for this limiting case, the results acquired should be consistent with appropriate large strain linear models in the infinitesimal limit.

In the anisotropic characterization of fibrin gel and white matter, a pure elastic model is adopted to describe the mechanical response, focusing on the short-time response. Although brain tissue exhibits viscoelastic behavior, the elastic component of the short-time response can be used to guide the selection of more general hyperelastic and viscoelastic models.

In the MRE study, dynamic shear modulus is estimated using an isotropic viscoelastic model. This model is likely to be valid for gray matter, which is structurally isotropic, but it neglects the anisotropic properties of white matter, as presented in chapter 5. Ideally, a transversely isotropic model for the modulus inversion of MRE data would give a more accurate estimate of the dynamic properties of the white matter.

7.3 Future Directions and Outlook

7.3.1 Brain-Skull Dynamic Response

To acquire brain-skull interaction data in the large strain regime, in vivo animal models could be used. An improved device inducing higher acceleration of the head could be used in a tagged MR study. This could provide a picture of brain-skull interaction during large deformation, or even during injury-level experiments. An animal model could also make longer scanning time possible, thus providing more 3D tagged images for studying the dynamics of impact.

A higher-resolution imaging sequence may be used for improving the tagged MR image resolution. A faster imaging sequence will reduce the scanning time, thus making the 3D image acquisition possible for human study.

The accuracy of the tagged image data could be improved by using a physical marker visible in the MR images. This will improve the rigid body registration step because a physical marker does not introduce the calculation error during the image processing step. The improved marker device could be applied to both animal and human tagged MR studies.

7.3.2 Brain Tissue Properties

In this dissertation, ex vivo mechanical tests of brain tissue and in vivo MRE tests of brain tissue were not in the same frequency range, which makes the direct comparison of the results difficult. Future studies could carry out the mechanical testing and MRE at comparable frequency ranges for the same species. Large mammalian brains such as lamb brain could be used. Due to the brain size of large mammals, in vivo MRE study may be difficult; however, in situ MRE could be a choice.

The mechanical testing in this dissertation focuses on the elastic characterization of the brain tissue. Future studies may address the viscoelastic properties. Proper viscoelastic models should be considered to enhance the current strain energy function used. A viscoelastic characterization would also have a better comparison to the MRE test.

7.3.3 Large Strain Model

The current strain energy function proves useful for explaining the shear anisotropy in the small strain regime. Future work should extend the small strain formulation into the large strain regime, which is more applicable in the study of TBI. Correspondingly, the DST and indentation experiments could be modified to test the tissue in large strain deformation and to verify the strain energy form in the large strain regime. Although it may be challenging, the FE simulation of large strain mechanical tests, and parameter analysis of the model will help understand the model physical implications.

7.3.4 Anisotropic MRE

Current shear moduli estimates from MRE are based on an isotropic linear elastic model. However, as pointed out in the chapter 6, brain tissue, like most biological tissue, is anisotropic. Developing an effective anisotropic model for MRE study is a promising direction to explore. Recently, Sinkus [70] and Romano [146] applied transversely isotropic models to the MRE study of breast and white matter. Although reasonable results were calculated from the 3D displacement field, the actuated wave propagation is still in one direction. Applying and measuring waves in multiple directions will provide more information about the tissue structure for an anisotropic moduli inversion. This will help us study a variety of anisotropic biological tissues such as white matter, muscle, and aorta.

7.3.5 Outlook

In summary, the knowledge of dynamic deformation and properties of brain issue is valuable to understand the mechanisms of TBI, to help improve neurosurgical procedures, to understand the brain development process, and to give useful information to the larger biomechanical research community.

Appendix

Transversely Isotropic Linearly Elastic Material Compliance Matrix

In Chapter 2, stiffness matrix $[\mathbb{C}]$ at reference configuration is given by Eq. (2.64). The corresponding compliance matrix is:

$$[\mathbb{S}] = \begin{bmatrix} s_{11} & s_{12}' & s_{12}' & & & \\ s_{12}' & s_{22} & s_{23}' & & & \\ s_{12}' & s_{23}' & s_{22} & & & \\ & & & \left(\frac{\partial\psi}{\partial I_1}-\frac{\partial\psi}{\partial I_3}\right)^{-1} & & \\ & & & & \left(\frac{\partial\psi}{\partial I_1}-\frac{\partial\psi}{\partial I_3}+2\frac{\partial\psi}{\partial I_5}\right)^{-1} & \\ & & & & & \left(\frac{\partial\psi}{\partial I_1}-\frac{\partial\psi}{\partial I_3}+2\frac{\partial\psi}{\partial I_5}\right)^{-1} \end{bmatrix},$$

where

$$s_{11} = \frac{\left(\frac{\partial^2\psi}{\partial I_1^2}-\frac{1}{4}\frac{\partial\psi}{\partial I_1}+4\frac{\partial^2\psi}{\partial I_1\partial I_2}+2\frac{\partial^2\psi}{\partial I_1\partial I_3}+4\frac{\partial^2\psi}{\partial I_2^2}+4\frac{\partial^2\psi}{\partial I_2\partial I_3}+\frac{1}{4}\frac{\partial\psi}{\partial I_3}+\frac{\partial^2\psi}{\partial I_3^2}\right)}{\frac{1}{8}\left(8\frac{\partial^2\psi}{\partial I_1^2}-2\frac{\partial\psi}{\partial I_1}+32\frac{\partial^2\psi}{\partial I_1\partial I_2}+16\frac{\partial^2\psi}{\partial I_1\partial I_3}+32\frac{\partial^2\psi}{\partial I_2^2}+32\frac{\partial^2\psi}{\partial I_2\partial I_3}+2\frac{\partial\psi}{\partial I_3}+8\frac{\partial^2\psi}{\partial I_3^2}\right)-\frac{\mathcal{D}}{4}},$$

$$s'_{12} = -\left(\frac{1}{2}\frac{\partial^2\psi}{\partial I_1^2} - \frac{1}{4}\frac{\partial\psi}{\partial I_1} + 2\frac{\partial^2\psi}{\partial I_1\partial I_2} + \frac{\partial^2\psi}{\partial I_1\partial I_3} + \frac{1}{2}\frac{\partial^2\psi}{\partial I_1\partial I_4} + \frac{\partial^2\psi}{\partial I_1\partial I_5} + 2\frac{\partial^2\psi}{\partial I_2^2}\right.$$
$$+ 2\frac{\partial^2\psi}{\partial I_2\partial I_3} + \frac{\partial^2\psi}{\partial I_2\partial I_4} + 2\frac{\partial^2\psi}{\partial I_2\partial I_5} + \frac{1}{4}\frac{\partial\psi}{\partial I_3} + \frac{1}{2}\frac{\partial^2\psi}{\partial I_3^2} + \frac{1}{2}\frac{\partial^2\psi}{\partial I_3\partial I_4}$$
$$\left.+ \frac{\partial^2\psi}{\partial I_3\partial I_5}\right)\left(\frac{1}{8}\left(8\frac{\partial^2\psi}{\partial I_1^2} - 2\frac{\partial\psi}{\partial I_1} + 32\frac{\partial^2\psi}{\partial I_1\partial I_2} + 16\frac{\partial^2\psi}{\partial I_1\partial I_3} + 32\frac{\partial^2\psi}{\partial I_2^2}\right.\right.$$
$$\left.\left.+ 32\frac{\partial^2\psi}{\partial I_2\partial I_3} + 2\frac{\partial\psi}{\partial I_3} + 8\frac{\partial^2\psi}{\partial I_3^2}\right)\mathcal{C} - \frac{\mathcal{D}}{4}\right)^{-1},$$

$$s_{22} = \frac{1}{4\left(\frac{\partial\psi}{\partial I_1} - \frac{\partial\psi}{\partial I_3}\right)} + \mathcal{B},$$

$$s'_{23} = -\frac{1}{4\left(\frac{\partial\psi}{\partial I_1} - \frac{\partial\psi}{\partial I_3}\right)} + \mathcal{B},$$

$$\mathcal{B} = \left(2\frac{\partial^2\psi}{\partial I_1^2} + 8\frac{\partial^2\psi}{\partial I_1\partial I_2} + 4\frac{\partial^2\psi}{\partial I_1\partial I_3} + 4\frac{\partial^2\psi}{\partial I_1\partial I_4} + 8\frac{\partial^2\psi}{\partial I_1\partial I_5} + 8\frac{\partial^2\psi}{\partial I_2^2} + 8\frac{\partial^2\psi}{\partial I_2\partial I_3}\right.$$
$$+ 8\frac{\partial^2\psi}{\partial I_2\partial I_4} + 16\frac{\partial^2\psi}{\partial I_2\partial I_5} + 2\frac{\partial^2\psi}{\partial I_3^2} + 4\frac{\partial^2\psi}{\partial I_3\partial I_4} + 8\frac{\partial^2\psi}{\partial I_3\partial I_5} + 2\frac{\partial^2\psi}{\partial I_4^2}$$
$$+ 8\frac{\partial^2\psi}{\partial I_4\partial I_5} + 4\frac{\partial\psi}{\partial I_5}$$
$$\left.+ 8\frac{\partial^2\psi}{\partial I_5^2}\right)\left(\left(4\frac{\partial^2\psi}{\partial I_1^2} - 2\frac{\partial\psi}{\partial I_1} + 16\frac{\partial^2\psi}{\partial I_1\partial I_2} + 8\frac{\partial^2\psi}{\partial I_1\partial I_3} + 16\frac{\partial^2\psi}{\partial I_2^2}\right.\right.$$
$$\left.+ 16\frac{\partial^2\psi}{\partial I_2\partial I_3} + 2\frac{\partial\psi}{\partial I_3} + 4\frac{\partial^2\psi}{\partial I_3^2}\right)\mathcal{C} - 2\mathcal{D}$$
$$+ \left(4\frac{\partial^2\psi}{\partial I_1^2} + 16\frac{\partial^2\psi}{\partial I_1\partial I_2} + 8\frac{\partial^2\psi}{\partial I_1\partial I_3} + 16\frac{\partial^2\psi}{\partial I_2^2} + 16\frac{\partial^2\psi}{\partial I_2\partial I_3}\right.$$
$$\left.\left.+ 4\frac{\partial^2\psi}{\partial I_3^2}\right)\mathcal{C}\right)^{-1},$$

$$\mathcal{C} = 4\frac{\partial^2\psi}{\partial I_1^2} + 16\frac{\partial^2\psi}{\partial I_1 \partial I_2} + 8\frac{\partial^2\psi}{\partial I_1 \partial I_3} + 8\frac{\partial^2\psi}{\partial I_1 \partial I_4} + 16\frac{\partial^2\psi}{\partial I_1 \partial I_5} + 16\frac{\partial^2\psi}{\partial I_2^2} + 16\frac{\partial^2\psi}{\partial I_2 \partial I_3}$$
$$+ 16\frac{\partial^2\psi}{\partial I_2 \partial I_4} + 32\frac{\partial^2\psi}{\partial I_2 \partial I_5} + 4\frac{\partial^2\psi}{\partial I_3^2} + 8\frac{\partial^2\psi}{\partial I_3 \partial I_4} + 16\frac{\partial^2\psi}{\partial I_3 \partial I_5} + 4\frac{\partial^2\psi}{\partial I_4^2}$$
$$+ 16\frac{\partial^2\psi}{\partial I_4 \partial I_5} + 8\frac{\partial\psi}{\partial I_5} + 16\frac{\partial^2\psi}{\partial I_5^2},$$
$$\mathcal{D} = \left(4\frac{\partial^2\psi}{\partial I_1^2} - 2\frac{\partial\psi}{\partial I_1} + 16\frac{\partial^2\psi}{\partial I_1 \partial I_2} + 8\frac{\partial^2\psi}{\partial I_1 \partial I_3} + 4\frac{\partial^2\psi}{\partial I_1 \partial I_4} + 8\frac{\partial^2\psi}{\partial I_1 \partial I_5} + 16\frac{\partial^2\psi}{\partial I_2^2}\right.$$
$$+ 16\frac{\partial^2\psi}{\partial I_2 \partial I_3} + 8\frac{\partial^2\psi}{\partial I_2 \partial I_4} + 16\frac{\partial^2\psi}{\partial I_2 \partial I_5} + 2\frac{\partial\psi}{\partial I_3} + 4\frac{\partial^2\psi}{\partial I_3^2} + 4\frac{\partial^2\psi}{\partial I_3 \partial I_4}$$
$$\left. + 8\frac{\partial^2\psi}{\partial I_3 \partial I_5}\right)^2.$$

References

[1] Menon, D.K., et al., Position Statement: Definition of Traumatic Brain Injury. *Arch Phys Med Rehab*, 91(11):1637-1640, 2010.

[2] Coronado, V.G., et al., Surveillance for traumatic brain injury-related deaths--United States, 1997-2007. *MMWR Surveill Summ*, 60(5):1-32, 2011.

[3] Risdall, J.E. and D.K. Menon, Traumatic brain injury. *Philos Trans R Soc Lond B Biol Sci*, 366(1562):241-50, 2011.

[4] Goldstein, M., Traumatic brain injury: A silent epidemic. *Annals of Neurology*, 27(3):327-327, 1990.

[5] Coup and Contrecoup. *The Lancet*, 242(6267):449-450, 1943.

[6] Swischuk, L.E., Obvious head injury: analyzing the mechanism. *Pediatr Emerg Care*, 22(3):195-6, 2006.

[7] Shaw, N.A., The neurophysiology of concussion. *Prog Neurobiol*, 67(4):281-344, 2002.

[8] Smith, D.H. and D.F. Meaney, Axonal Damage in Traumatic Brain Injury. *Neuroscientist*, 6(6):483-495, 2000.

[9] Meythaler, J.M., et al., Current concepts: diffuse axonal injury-associated traumatic brain injury. *Arch Phys Med Rehabil*, 82(10):1461-71, 2001.

[10] Sharp, D.J. and T.E. Ham, Investigating white matter injury after mild traumatic brain injury. *Curr Opin Neurol*, 24(6):558-63, 2011.

[11] Ueno, K., et al., Development of tissue level brain injury criteria by finite element analysis. *J Neurotrauma*, 12(4):695-706, 1995.

[12] Cloots, R.J., J.A. van Dommelen, and M.G. Geers, A tissue-level anisotropic criterion for brain injury based on microstructural axonal deformation. *J Mech Behav Biomed Mater*, 5(1):41-52, 2012.

[13] Zhang, L., K.H. Yang, and A.I. King, A proposed injury threshold for mild traumatic brain injury. *J Biomech Eng*, 126(226-236, 2004.

[14] Zou, H. and J.P. Schmiedeler, Predicting brain injury under impact with a strain measure from analytical models. *Int J Crashworthines*, 13(3):337-348, 2008.

[15] Ibrahim, N.G., et al., Influence of age and fall type on head injuries in infants and toddlers. *International Journal of Developmental Neuroscience*, 0):

[16] El Sayed, T., et al., Biomechanics of traumatic brain injury. *Computer Methods in Applied Mechanics and Engineering*, 197(4692-4701, 2008.

[17] Mao, H.J., et al., Strain-Based Regional Traumatic Brain Injury Intensity in Controlled Cortical Impact: A Systematic Numerical Analysis. *Journal of neurotrauma*, 28(11):2263-2276, 2011.

[18] Ivancevic, V.G., New mechanics of traumatic brain injury. *Cogn Neurodyn*, 3(3):281-93, 2009.

[19] Wright, R.M. and K.T. Ramesh, An axonal strain injury criterion for traumatic brain injury. *Biomech Model Mechanobiol*, 2011.

[20] McAllister, T.W., et al., Maximum principal strain and strain rate associated with concussion diagnosis correlates with changes in corpus callosum white matter indices. *Ann Biomed Eng*, 40(127-40, 2012.

[21] Morrison, B., 3rd, et al., A tissue level tolerance criterion for living brain developed with an in vitro model of traumatic mechanical loading. *Stapp Car Crash J*, 47(93-105, 2003.

[22] LaPlaca, M.C., et al., High rate shear strain of three-dimensional neural cell cultures: a new in vitro traumatic brain injury model. *J Biomech*, 38(5):1093-105, 2005.

[23] Kimpara, H., et al., Investigation of anteroposterior head-neck responses during severe frontal impacts using a brain-spinal cord complex FE model. *Stapp Car Crash J*, 50(509-44, 2006.

[24] Raul, J.S., et al., Finite-element models of the human head and their applications in forensic practice. *Int J Legal Med*, 122(5):359-66, 2008.

[25] Sayed, T.M.E., *Constitutive models for polymers and soft biological tissues*. 2008, California Institute of Technology: Pasadena. p. 127.

[26] Chatelin, S., A. Constantinesco, and R. Willinger, Fifty years of brain tissue mechanical testing: From in vitro to in vivo investigations. *Biorheology*, 47(255-276, 2010.

[27] Cheng, S., E.C. Clarke, and L.E. Bilston, Rheological properties of the tissues of the central nervous system: a review. *Med Eng Phys*, 30(10):1318-37, 2008.

[28] Miller, K., et al., Mechanical properties of brain tissue in-vivo: experiment and computer simulation. *J Biomech*, 33(11):1369-76, 2000.

[29] Miller, K., Constitutive model of brain tissue suitable for finite element analysis of surgical procedures. *Journal of Biomechanics*, 32(5):531-537, 1999.

[30] Gefen, A. and S.S. Margulies, Are in vivo and in situ brain tissues mechanically similar? *J Biomech*, 37(1339-1352, 2004.

[31] Elkin, B.S., A. Ilankovan, and B. Morrison Iii, A detailed viscoelastic characterization of the rat brain. *J Neurotrauma*, 2011.

[32] van Dommelen, J.A., et al., Mechanical properties of brain tissue by indentation: interregional variation. *J Mech Behav Biomed Mater*, 3(2):158-66, 2010.

[33] Shuck, L.Z. and S.H. Advani, Rheological Response of Human Brain-Tissue in Shear. *Journal of Basic Engineering*, 94(905-911, 1972.

[34] Peters, G.W.M., J.H. Meulman, and A.A.H.J. Sauren, The applicability of the time/temperature superposition principle to brain tissue. *Biorheology*, 34(2):127-138, 1997.

[35] Bilston, L.E., Z. Liu, and N. Phan-Thien, Linear viscoelastic properties of bovine brain tissue in shear. *Biorheology*, 34(6):377-85, 1997.

[36] Arbogast, K.B. and S.S. Margulies, Material characterization of the brainstem from oscillatory shear tests. *J Biomech*, 31(9):801-7, 1998.

[37] Thibault, K.L. and S.S. Margulies, Age-dependent material properties of the porcine cerebrum: effect on pediatric inertial head injury criteria. *Journal of Biomechanics*, 31(12):1119-1126, 1998.

[38] Bilston, L.E., Z.Z. Liu, and N. Phan-Thien, Large strain behaviour of brain tissue in shear: Some experimental data and differential constitutive model. *Biorheology*, 38(4):335-345, 2001.

[39] Prange, M.T. and S.S. Margulies, Regional, directional, and age-dependent properties of the brain undergoing large deformation. *J Biomech Eng*, 124(244-252, 2002.

[40] Hrapko, M., et al., The mechanical behaviour of brain tissue: large strain response and constitutive modelling. *Biorheology*, 43(5):623-36, 2006.

[41] Vappou, J., et al., Magnetic resonance elastography compared with rotational rheometry for in vitro brain tissue viscoelasticity measurement. *Magma*, 20(5-6):273-8, 2007.

[42] Garo, A., et al., Towards a reliable characterisation of the mechanical behaviour of brain tissue: The effects of post-mortem time and sample preparation. *Biorheology*, 44(1):51-8, 2007.

[43] Hrapko, M., et al., The influence of test conditions on characterization of the mechanical properties of brain tissue. *J Biomech Eng*, 130(3):031003, 2008.

[44] Nicolle, S., et al., Shear linear behavior of brain tissue over a large frequency range. *Biorheology*, 42(209-223, 2005.

[45] Velardi, F., F. Fraternali, and M. Angelillo, Anisotropic constitutive equations and experimental tensile behavior of brain tissue. *Biomech Model Mechanobiol*, 5(1):53-61, 2006.

[46] Miller, K. and K. Chinzei, Mechanical properties of brain tissue in tension. *Journal of Biomechanics*, 35(4):483-490, 2002.

[47] Franceschini, G., *THE MECHANICS OF HUMAN BRAIN TISSUE*, in *Department of mechanical and structural engineering*. 2006, UNIVERSITY OF TRENTO: TRENTO. p. 130.

[48] Cheng, S. and L.E. Bilston, Unconfined compression of white matter. *J Biomech*, 40(1):117-24, 2007.

[49] Hrapko, M., et al., Characterisation of the mechanical behaviour of brain tissue in compression and shear. *Biorheology*, 45(6):663-76, 2008.

[50] Christ, A.F., et al., Mechanical difference between white and gray matter in the rat cerebellum measured by scanning force microscopy. *J Biomech*, 43(15):2986-92, 2010.

[51] Elkin, B.S., A. Ilankova, and B. Morrison, Dynamic, Regional Mechanical Properties of the Porcine Brain: Indentation in the Coronal Plane. *J Biomech Eng-T Asme*, 133(7):2011.

[52] Axel, L. and L. Dougherty, MR imaging of motion with spatial modulation of magnetization. *Radiology*, 171(3):841-5, 1989.

[53] Axel, L. and L. Dougherty, Heart wall motion: improved method of spatial modulation of magnetization for MR imaging. *Radiology*, 172(2):349-50, 1989.

[54] Bayly, P.V., et al., Deformation of the human brain induced by mild acceleration. *J Neurotrauma*, 22(845-856, 2005.

[55] Feng, Y., et al., Relative brain displacement and deformation during constrained mild frontal head impact. *J R Soc Interface*, 7(53):1677-88, 2010.

[56] Ehman, R.L., et al., Magnetoelastography - Mr-Imaging of Acoustic Strain Waves. *Radiology*, 197(355-355, 1995.

[57] Muthupillai, R., et al., Magnetic resonance elastography by direct visualization of propagating acoustic strain waves. *Science*, 269(5232):1854-7, 1995.

[58] Hamhaber, U., et al., Three-dimensional analysis of shear wave propagation observed by in vivo magnetic resonance elastography of the brain. *Acta Biomater*, 3(1):127-37, 2007.

[59] Klatt, D., et al., Noninvasive assessment of the rheological behavior of human organs using multifrequency MR elastography: a study of brain and liver viscoelasticity. *Phys Med Biol*, 52(24):7281-94, 2007.

[60] Sack, I., et al., Non-invasive measurement of brain viscoelasticity using magnetic resonance elastography. *NMR Biomed*, 21(265-271, 2008.

[61] Green, M.A., L.E. Bilston, and R. Sinkus, In vivo brain viscoelastic properties measured by magnetic resonance elastography. *NMR Biomed*, 21(755-764, 2008.

[62] Mac Donald, C.L., et al., Detection of blast-related traumatic brain injury in U.S. military personnel. *N Engl J Med*, 364(22):2091-100, 2011.

[63] Riek, K., et al., Wide-range dynamic magnetic resonance elastography. *J Biomech*, 44(7):1380-6, 2011.

[64] Atay, S.M., et al., Measurement of the dynamic shear modulus of mouse brain tissue in vivo by magnetic resonance elastography. *J Biomech Eng*, 130(21013, 2008.

[65] Clayton, E.H. and et al., Frequency-dependent viscoelastic parameters of mouse brain tissue estimated by MR elastography. *Phys Med Biol*, 56(8):2391, 2011.

[66] Murphy, M.C., et al., Magnetic resonance elastography of the brain in a mouse model of Alzheimer's disease: initial results. *Magn Reson Imaging*, 30(4):535-9, 2012.

[67] Boulet, T., M.L. Kelso, and S.F. Othman, Microscopic magnetic resonance elastography of traumatic brain injury model. *J Neurosci Methods*, 201(2):296-306, 2011.

[68] Klatt, D., et al., Viscoelastic properties of liver measured by oscillatory rheometry and multifrequency magnetic resonance elastography. *Biorheology*, 47(2):133-41, 2010.

[69] Asbach, P., et al., Viscoelasticity-based staging of hepatic fibrosis with multifrequency MR elastography. *Radiology*, 257(1):80-6, 2010.

[70] Sinkus, R., et al., Imaging anisotropic and viscous properties of breast tissue by magnetic resonance-elastography. *Magn Reson Med*, 53(2):372-87, 2005.

[71] Sinkus, R., et al., Viscoelastic shear properties of in vivo breast lesions measured by MR elastography. *Magn Reson Imaging*, 23(2):159-65, 2005.

[72] Xydeas, T., et al., Magnetic resonance elastography of the breast: correlation of signal intensity data with viscoelastic properties. *Invest Radiol*, 40(7):412-20, 2005.

[73] Elgeti, T., et al., Cardiac magnetic resonance elastography: toward the diagnosis of abnormal myocardial relaxation. *Invest Radiol*, 45(12):782-7, 2010.

[74] Li, S.Y., et al., A feasibility study of MR elastography in the diagnosis of prostate cancer at 3.0T. *Acta Radiol.*, 52(3):354-358, 2011.

[75] Chopra, R., et al., In Vivo MR Elastography of the Prostate Gland Using a Transurethral Actuator. *Magnet Reson Med*, 62(3):665-671, 2009.

[76] Bensamoun, S.F., et al., Determination of thigh muscle stiffness using magnetic resonance elastography. *J Magn Reson Imaging*, 23(2):242-7, 2006.

[77] Shafieian, M., K.K. Darvish, and J.R. Stone, Changes to the viscoelastic properties of brain tissue after traumatic axonal injury. *J Biomech*, 42(13):2136-42, 2009.

[78] Kyriacou, S.K., et al., Brain mechanics For neurosurgery: modeling issues. *Biomech Model Mechanobiol*, 1(2):151-64, 2002.

[79] Xu, G., et al., Axons pull on the brain, but tension does not drive cortical folding. *J Biomech Eng*, 132(7):071013, 2010.

[80] Richman, D.P., et al., Mechanical Model of Brain Convolutional Development. *Science*, 189(4196):18-21, 1975.

[81] Van Essen, D.C., A tension-based theory of morphogenesis and compact wiring in the central nervous system. *Nature*, 385(6614):313-8, 1997.

[82] Gasser, T.C., R.W. Ogden, and G.A. Holzapfel, Hyperelastic modelling of arterial layers with distributed collagen fibre orientations. *J R Soc Interface*, 3(6):15-35, 2006.

[83] Humphrey, J.D., R.K. Strumpf, and F.C.P. Yin, Determination of a Constitutive Relation for Passive Myocardium .1. A New Functional Form. *Journal of Biomechanical Engineering-Transactions of the Asme*, 112(3):333-339, 1990.

[84] Humphrey, J.D., R.K. Strumpf, and F.C.P. Yin, Determination of a Constitutive Relation for Passive Myocardium .2. Parameter-Estimation. *Journal of Biomechanical Engineering-Transactions of the Asme*, 112(3):340-346, 1990.

[85] Holzapfel, G.A. and R.W. Ogden, Constitutive modelling of passive myocardium: a structurally based framework for material characterization. *Philos T R Soc A*, 367(1902):3445-3475, 2009.

[86] Ning, X., et al., A transversely isotropic viscoelastic constitutive equation for brainstem undergoing finite deformation. *J Biomech Eng*, 128(925-933, 2006.

[87] Meaney, D.F., Relationship between structural modeling and hyperelastic material behavior: application to CNS white matter. *Biomech Model Mechanobiol*, 1(4):279-93, 2003.

[88] Spencer, A.J.M., *Continuum theory of the mechanics of fibre-reinforced composites*, Springer-Verlag, New York, 1984.

[89] Arbogast, K.B. and S.S. Margulies, A fiber-reinforced composite model of the viscoelastic behavior of the brainstem in shear. *Journal of Biomechanics*, 32(8):865-870, 1999.

[90] Galford, J.E. and J.H. McElhaney, A viscoelastic study of scalp, brain, and dura. *J Biomech*, 3(211-221, 1970.

[91] Fallenstein, G.T., V.D. Hulce, and J.W. Melvin, Dynamic mechanical properties of human brain tissue. *J Biomech*, 2(217-226, 1969.

[92] Mendis, K.K., R.L. Stalnaker, and S.H. Advani, A Constitutive Relationship for Large-Deformation Finite-Element Modeling of Brain-Tissue. *Journal of Biomechanical Engineering-Transactions of the Asme*, 117(3):279-285, 1995.

[93] Kohandel, M., et al., Frequency dependence of complex moduli of brain tissue using a fractional Zener model. *Phys Med Biol*, 50(12):2799-805, 2005.

[94] Streitberger, K.J., et al., In vivo viscoelastic properties of the brain in normal pressure hydrocephalus. *NMR Biomed*, 2010.

[95] Holzapfel, G., *Nonlinear Solid Mechanics: A Continuum Approach for Engineering*, John Wiley & Sons, Inc. 455, 2000.

[96] Spencer, A.J.M., Theory of Invariants. *Continuum Physics*, 1(III):239-255, 1972.

[97] Love, A.E.H., *A treatise on the mathematical theory of elasticity*. 4th ed, Dover Publications. xviii, 643 p., New York, 1944.

[98] Merodio, J. and R.W. Ogden, Instabilities and loss of ellipticity in fiber-reinforced compressible non-linearly elastic solids under plane deformation. *International Journal of Solids and Structures*, 40(4707-4727, 2003.

[99] Bower, A.F., *Applied Mechanics of Solids*. 1st ed, CRC Press. 820, Boca Raton, FL, 2010.

[100] Namani, R., et al., Elastic characterization of transversely isotropic soft materials by dynamic shear and asymmetric indentation. *J Biomech Eng*, 134(6):061004, 2012.

[101] Flügge, W., *Viscoelasticity*. A Blaisdell book in solid mechanics, Blaisdell Pub. Co. viii, 127 p., Waltham, Mass.,, 1967.

[102] Auld, B.A., *Acoustic fields and waves in solids*. 2nd ed, R.E. Krieger, Malabar, FL, 1990.

[103] Kolsky, H., *Stress waves in solids*. 1963, Dover Publications: New York,.

[104] Pudenz, R.H. and C.H. Shelden, The Lucite Calvarium—A Method for Direct Observation of the Brain. *Journal of Neurosurgery*, 3(6):487-505, 1946.

[105] Shelden, C.H., et al., The Lucite Calvarium—A Method for Direct Observation of the Brain. *Journal of Neurosurgery*, 1(1):67-75, 1944.

[106] Ommaya, A.K., J.W. Boretos, and E.E. Beile, The Lexan calvarium: an improved method for direct observation of the brain. *J Neurosurg*, 30(1):25-9, 1969.

[107] Gosch, H.H., E. Gooding, and R.C. Schneider, Distortion and displacement of the brain in experimental head injuries. *Surg Forum*, 20(425-6, 1969.

[108] Hodgson, V.R., E.S. Gurdjian, and L.M. Thomas, Experimental Skull Deformation and Brain Displacement Demonstrated by Flash X-Ray Technique*. *Journal of Neurosurgery*, 25(5):549-552, 1966.

[109] Shatsky, S.A., et al., Traumatic Distortions of the Primate Head and Chest: Correlation of Biomechanical, Radiological and Pathological Data. *Proceedings of the 18st Stapp Car Crash Conference*, 351-381, 1974.

[110] Stalnaker, R.L., et al., Head Impact Response. *Proceedings of the 21st Stapp Car Crash Conference*, 305-335, 1977.

[111] Hardy, W.N., et al., Investigation of Head Injury Mechanisms Using Neutral Density Technology and High-Speed Biplanar X-ray. *Stapp Car Crash J*, 45(337-68, 2001.

[112] Zou, H., J.P. Schmiedeler, and W.N. Hardy, Separating brain motion into rigid body displacement and deformation under low-severity impacts. *Journal of Biomechanics*, 40(6):1183-1191, 2007.

[113] Sabet, A.A., et al., Deformation of the human brain induced by mild angular head acceleration. *J Biomech*, 41(2):307-15, 2008.

[114] Ji, S. and S.S. Margulies, In vivo pons motion within the skull. *J Biomech*, 40(1):92-9, 2007.

[115] Zhang, L., et al., Recent advances in brain injury research: a new human head model development and validation. *Stapp Car Crash J*, 45(369-94, 2001.

[116] Kleiven, S. and W. Hardy, Correlation of an FE model of the human head with local brain motion—consequences for injury prediction. *Proceedings 46th Stapp Car Crash Conference, SAE paper*, 2002-22-0007(123–144, 2002.

[117] Cloots, R.J., et al., Biomechanics of traumatic brain injury: influences of the morphologic heterogeneities of the cerebral cortex. *Ann Biomed Eng*, 36(7):1203-15, 2008.

[118] Masood, S., et al., Investigating intrinsic myocardial mechanics: the role of MR tagging, velocity phase mapping, and diffusion imaging. *J Magn Reson Imaging*, 12(6):873-83, 2000.

[119] Axel, L., A. Montillo, and D. Kim, Tagged magnetic resonance imaging of the heart: a survey. *Medical Image Analysis*, 9(4):376-393, 2005.

[120] Osman, N.F., E.R. McVeigh, and J.L. Prince, Imaging heart motion using harmonic phase MRI. *IEEE Trans Med Imaging*, 19(3):186-202, 2000.

[121] Kaster, T., I. Sack, and A. Samani, Measurement of the hyperelastic properties of ex vivo brain tissue slices. *J Biomech*, 44(6):1158-63, 2011.

[122] Muthupillai, R. and R.L. Ehman, Magnetic resonance elastography. *Nat Med*, 2(5):601-3, 1996.

[123] Asbach, P., et al., Assessment of liver viscoelasticity using multifrequency MR elastography. *Magn Reson Med*, 60(2):373-9, 2008.

[124] McCracken, P.J., et al., Mechanical transient-based magnetic resonance elastography. *Magn Reson Med*, 53(3):628-39, 2005.

[125] Di Ieva, A., et al., Magnetic resonance elastography: a general overview of its current and future applications in brain imaging. *Neurosurgical Review*, 33(137-145, 2010.

[126] Hamhaber, U., et al., In vivo magnetic resonance elastography of human brain at 7 T and 1.5 T. *J Magn Reson Imaging*, 32(3):577-83, 2010.

[127] Clayton, E.H., G.M. Genin, and P.V. Bayly, Transmission, attenuation and reflection of shear waves in the human brain. *J R Soc Interface*, 2012.

[128] Zhang, J., et al., Viscoelastic properties of human cerebellum using magnetic resonance elastography. *J Biomech*, 44(10):1909-13, 2011.

[129] Clayton, E.H., J.R. Garbow, and P.V. Bayly, Frequency-dependent viscoelastic parameters of mouse brain tissue estimated by MR elastography. *Phys Med Biol*, 56(8):2391-406, 2011.

[130] Schregel, K., et al., Demyelination reduces brain parenchymal stiffness quantified in vivo by magnetic resonance elastography. *Proc Natl Acad Sci U S A*, 109(17):6650-5, 2012.

[131] Pattison, A.J., et al., Time-harmonic magnetic resonance elastography of the normal feline brain. *J Biomech*, 43(14):2747-52, 2010.

[132] Barnette, A.R., et al., Characterization of brain development in the ferret via MRI. *Pediatr Res*, 66(1):80-4, 2009.

[133] Knutsen, A.K., et al., A new method to measure cortical growth in the developing brain. *J Biomech Eng*, 132(10):101004, 2010.

[134] Neal, J., et al., Insights into the gyrification of developing ferret brain by magnetic resonance imaging. *J Anat*, 210(1):66-77, 2007.

[135] Chang, Y.V., et al., *Measurement of ferret brain tissue stiffness in vivo using MR elastography*, in *Proceedings of the 19th Annual ISMRM Scientific Meeting and Exhibition*. 2011: Montreal, Quebec. p. 3474.

[136] Spottiswoode, B.S., et al., Tracking myocardial motion from cine DENSE images using spatiotemporal phase unwrapping and temporal fitting. *IEEE Trans Med Imaging*, 26(1):15-30, 2007.

[137] Soutas-Little, R.W., *Elasticity*, Dover. xvi, 431 p., Mineola, NY, 1973.

[138] Romano, A.J., et al., Determination and analysis of guided wave propagation using magnetic resonance elastography. *Magn Reson Med*, 54(4):893-900, 2005.

[139] Tong, Y.Y., et al., Discrete multiscale vector field decomposition. *ACM Transactions on Graphics*, 22(3):445-452, 2003.

[140] McGarry, M.D., et al., An octahedral shear strain-based measure of SNR for 3D MR elastography. *Phys Med Biol*, 56(13):N153-64, 2011.

[141] Kruse, S.A., et al., Magnetic resonance elastography of the brain. *Neuroimage*, 39(1):231-7, 2008.

[142] Kruse, S.A. and R.L. Ehman, *2D Approximation of 3D Wave Propagation in MR Elastography of the Brain*, in *Proceedings of the 11th ISMRM Scientific Meeting and Exhibition*. 2003: Toronto. p. 1084.

[143] Feng, Y., et al., *Anisotropic mechanical properties of brain tissue characterized by indentation and shear tests.*, in *SEM Annual Conference and Exposition on Experimental and Applied Mechanics,*. 2012: Costa Mesa, CA.

[144] Feng, Y., et al., *Identification of a transversely isotropic material model for white matter in the brain.* , in *ASME International Mechanical Engineering Congress and Exposition.* . 2012: Houston, TX. p. IMECE2012-88374.

[145] Margulies, S., et al., Shaken baby syndrome: a flawed biomechanical analysis. *Forensic Sci Int*, 164(2-3):278-9; author reply 282-3, 2006.

[146] Romano, A., et al., In vivo waveguide elastography of white matter tracts in the human brain. *Magn Reson Med*, 2012.

[147] Manduca, A., et al., Magnetic resonance elastography: non-invasive mapping of tissue elasticity. *Med Image Anal*, 5(4):237-54, 2001.

[148] Billiar, K.L. and M.S. Sacks, Biaxial mechanical properties of the natural and glutaraldehyde treated aortic valve cusp--Part I: Experimental results. *Journal of biomechanical engineering*, 122(23-30, 2000.

[149] Holzapfel, G.A., Ogden, Ray W, On planar biaxial tests for anisotropic nonlinearly elastic solids . *Mathematics and Mechanics of Solids*, 14(474-489, 2009.

[150] Karduna, a.R., H.R. Halperin, and F.C. Yin, Experimental and numerical analyses of indentation in finite-sized isotropic and anisotropic rubber-like materials. *Annals of biomedical engineering*, 25(1009-16, 1997.

[151] Bischoff, J.E., Static indentation of anisotropic biomaterials using axially asymmetric indenters--a computational study. *J Biomech Eng*, 126(4):498-505, 2004.

[152] Elkin, B.S., A. Ilankova, and B. Morrison, 3rd, Dynamic, regional mechanical properties of the porcine brain: indentation in the coronal plane. *J Biomech Eng*, 133(7):071009, 2011.

[153] Cox, M.A., et al., Mechanical characterization of anisotropic planar biological soft tissues using large indentation: a computational feasibility study. *J Biomech Eng*, 128(3):428-36, 2006.

[154] Torbet, J., J.M. Freyssinet, and G. Hudry-Clergeon, Oriented fibrin gels formed by polymerization in strong magnetic fields. *Nature*, 289(5793):91-93, 1981.

[155] Namani, R., et al., Anisotropic mechanical properties of magnetically aligned fibrin gels measured by magnetic resonance elastography. *J Biomech*, 42(13):2047-53, 2009.

[156] Okamoto, R.J., E.H. Clayton, and P.V. Bayly, Viscoelastic properties of soft gels: comparison of magnetic resonance elastography and dynamic shear testing in the shear wave regime. *Phys Med Biol*, 56(19):6379-400, 2011.

[157] Margulies, S.S. and l.e. Thibault, A proposed tolerance criterion for diffuse axonal injury in man. *J Biomech*, 25(917-923, 1992.

[158] Gennarelli, T.A., et al., Diffuse axonal injury and traumatic coma in the primate. *Ann Neurol*, 12(6):564-74, 1982.

[159] Wright, R.M. and K.T. Ramesh, An axonal strain injury criterion for traumatic brain injury. *Biomech Model Mechanobiol*, 11(1-2):245-60, 2012.

[160] Abney, T.M., et al., Principal component analysis of dynamic relative displacement fields estimated from MR images. *PLoS One*, 6(7):e22063, 2011.

[161] Brody, D.L., et al., Electromagnetic controlled cortical impact device for precise, graded experimental traumatic brain injury. *J Neurotrauma*, 24(4):657-73, 2007.

[162] Ji, S., et al., In vivo measurements of human brain displacement. *Stapp Car Crash J*, 48(227-37, 2004.

[163] Coats, B., S.S. Margulies, and S. Ji, Parametric study of head impact in the infant. *Stapp Car Crash J*, 51(1-15, 2007.

[164] Bayly, P.V., E.H. Clayton, and G.M. Genin, Quantitative imaging methods for the development and validation of brain biomechanics models. *Annu Rev Biomed Eng*, 14(369-96, 2012.

[165] Kaster, T., I. Sack, and A. Samani, Measurement of the hyperelastic properties of ex vivo brain tissue slices. *J Biomech*, 2011.

[166] Spencer, A., *Continuum theory of the mechanics of fibre-reinforced composites*, Springer-Verlag, Wien ;;New York, 1984.

[167] Qiu, G.Y. and T.J. Pence, Remarks on the behavior of simple directionally reinforced incompressible nonlinearly elastic solids. *Journal of Elasticity*, 49(1):1-30, 1997.

[168] Merodio, J. and R.W. Ogden, Mechanical response of fiber-reinforced incompressible non-linearly elastic solids. *International Journal of Nonlinear Mechanics*, 40(213-227, 2005.

[169] Alexander, G.M. and D.W. Godwin, Presynaptic inhibition of corticothalamic feedback by metabotropic glutamate receptors. *J Neurophysiol*, 94(163-175, 2005.

[170] Prevost, T.P., et al., Dynamic mechanical response of brain tissue in indentation in vivo, in situ and in vitro. *Acta Biomater*, 7(12):4090-101, 2011.

[171] Hrapko, M., et al., Characterisation of the mechanical behaviour of brain tissue in compression and shear. *Biorheology*, 45(663-676, 2008.

[172] Prange, M.T. and S.S. Margulies, Regional, directional, and age-dependent properties of the brain undergoing large deformation. *J Biomech Eng*, 124(2):244-52, 2002.

[173] Prange, M.T., D.F. Meaney, and S.S. Margulies, Defining brain mechanical properties: effects of region, direction, and species. *Stapp Car Crash J*, 44(205-213, 2000.

[174] Kruse, S.A., et al., Magnetic resonance elastography of the brain. *NeuroImage*, 39(231-7, 2008.

[175] Cosgrove, K.P., C.M. Mazure, and J.K. Staley, Evolving knowledge of sex differences in brain structure, function, and chemistry. *Biol Psychiatry*, 62(8):847-55, 2007.

Vita

Yuan Feng

Degrees

Ph.D. Mechanical Engineering, December 2012
M.S. Mechanical Engineering, December 2011
M.S. Mechatronics Engineering, July 2008
B.S. Thermo Energy and Power Engineering, July 2006

Professional Societies

American Society of Mechanical Engineers (ASME)
National Society of Professional Engineers (NSPE)

Journal Publications

Feng, Y., Clayton, E. H., Chang, Y. V., Okamoto, R. J., Bayly, P. V., "Viscoelastic Properties of the Ferret Brain Measured In Vivo at Multiple Frequencies by Magnetic Resonance Elastography" (submitted).

Feng, Y., Namani, R., Okamoto, Genin, G. M., Bayly, P. V., "Elastic Characterization of Brain Tissue and Implications for Transversely Isotropic Models of White Matter" (submitted).

Namani R., Feng Y., Okamoto R. J., Jesuraj N., Genin G. M., and Bayly P. V., 2012, "Elastic Characterization of Transversely Isotropic Soft Materials by Dynamic Shear and Asymmetric Indentation," J Biomech Eng, 1-37.

Abney, T. M., Feng, Y., Pless, R., Okamoto, R. J., Genin, G. M. & Bayly, P. V. 2011. "Principal Component Analysis of Dynamic Relative Displacement Fields Estimated from MR Images". PLoS One, 6, e22063.

Feng, Y., Abney, T. M., Okamoto, R. J., Pless, R. B., Genin, G. M. & Bayly, P. V. 2010. "Relative brain displacement and deformation during constrained mild frontal head impact". J R Soc Interface, 7, 1677-88.

Hu, H., Li M., Wang P., Feng, Y., Sun, L., 2009. "Development of a Continuum Robot for Colonoscopy", High Technology Letter, 2, 115-119.

Conference Abstract and Proceedings

Feng Y., Okamoto R. J., Namani R., Genin G. M., and Bayly P. V., 2012, "Identification of A Transversely Isotropic Material Model for White Matter In The Brain", Proceedings of the ASME 2012 International Mechanical Engineering Congress & Exposition, Houston, Texas, USA, November 9-15, 2012.

Feng Y., Chang Y., Clayton E. H., Okamoto R. J., and Bayly P. V., 2012, "Shear wave propagation of the ferret brain at multiple frequencies in vivo", Proceedings of the ASME 2012 International Mechanical Engineering Congress & Exposition, Houston, Texas, USA, November 9-15, 2012.

Feng, Y, Namani, R., Okamoto, R. J., Genin, G. M., Bayly, P. V., "Anisotropic mechanical properties of brain tissue characterized by shear and indentation tests", SEM XII International Congress & Exposition on Experimental and Applied Mechanics. Costa Mesa, CA, USA, June 11-14, 2012. (presentation for SEM International Student Paper Competition)

Chang, Y., Feng, Y., Clayton, E. H., Bayly, P. V., "Measurement of Ferret Brain Tissue Stiffness in vivo Using MR Elastography", Proceedings of the International Society for Magnetic Resonance in Medicine, Montreal, Canada, May 7-13, 2011.

Feng, Y., Abney, T. M., Okamoto, R. J., Pless, R. B., Genin, G. M. & Bayly, P. V., "Relative Motion Of The Brain And Skull During Mild Head impact", US National Congress of Theoretical and Applied Mechanics, State College, Pennsylvania, June 27-July 2, 2010. Award: Student Travel Stipend.

Bayly, P. V., Clayton, E. H., Feng, Y., Abney, T. M., Namani, R., Okamoto, R. J., Genin, G. M., "Measurement of Brain Biomechanics in Vivo by Magnetic Resonance Imaging", SEM Annual Conference and Exposition on Experimental and Applied Mechanics, Indianapolis, Indiana, June 7-10, 2010.

Feng, Y., Abney, T. M., Okamoto, R. J., Pless, R. B., Genin, G. M. & Bayly, P. V., "Measurement of Brain Deformation During Mild Frontal Head Impact", ASME International Mechanical Engineering Congress & Exposition. Lake Buena Vista, Florida, November 13-19, 2009.

Abney, T. M., Feng, Y., Okamoto, R. J., Pless, R. B., Genin, G. M. & Bayly, P. V., "Materials and Structures in the Mechanical Interaction of the Skull and Brain", ASME International Mechanical Engineering Congress & Exposition. Lake Buena Vista, Florida, November 13-19, 2009.

Feng, Y., Li, W., Li, M. & Sun, L., "Structure Optimization of The Endoscopic Robot Ciliary Leg Based on Dimensional Analysis", IEEE International Conference on Robotics and Biomimetics, 15-18 Dec. 2007. 109-114.

December 2012